

**DEFORMATION MECHANISMS IN MAGNESIUM ALLOYS  
AT ELEVATED TEMPERATURE**

**BY**

**DAVID E. CIPOLETTI**

**B.S., LAFAYETTE COLLEGE, 2006**

**A DISSERTATION SUBMITTED IN PARTIAL FULFILLMENT  
OF THE REQUIREMENTS FOR  
THE DEGREE OF DOCTOR OF PHLOSOPHY  
IN THE SCHOOL OF ENGINEERING AT BROWN UNIVERSITY**

**PROVIDENCE, RI**

**MAY 2011**

© Copyright 2011 by David E. Cipoletti

This dissertation by David E. Cipoletti is accepted in its present form  
by the School of Engineering as satisfying the  
dissertation requirement for the degree of Doctor of Philosophy

Date \_\_\_\_\_

\_\_\_\_\_

Allan F. Bower, Advisor

Recommended to the Graduate Council

Date \_\_\_\_\_

\_\_\_\_\_

William A. Curtin, Reader

Date \_\_\_\_\_

\_\_\_\_\_

K. Sharvan Kumar, Reader

Approved by the Graduate Council

Date \_\_\_\_\_

\_\_\_\_\_

Peter Weber, Dean of the Graduate School

## **Curriculum Vitae**

David E. Cipoletti was born on October 6, 1983 in Providence, Rhode Island to proud parents, Steven and Jane Cipoletti. He grew up in Barrington, RI with his sister, Susan, and brother, Scott, where he attended the Barrington public school system and graduated from Barrington High School in June 2002. Upon graduation from high school, David enrolled at Lafayette College in Easton, Pennsylvania where he received his Bachelors of Science degree in Mechanical Engineering in May 2006. After completing his undergraduate education, David began his graduate work at Brown University in Providence, RI under the tutelage of his advisor, Dr. Allan F. Bower. He defended his Ph.D. dissertation on Wednesday, May 11<sup>th</sup>, 2011.

## Acknowledgements

First, I would like to thank my advisor Dr. Allan Bower. Without your patient support and steady guidance throughout my development as a graduate student, researcher, and teacher, I would not be where I am today. I would also like to thank my advisor at General Motors, Dr. Paul Krajewski. Your tutelage has been instrumental in my development, thank you for your continuous advice and support. I owe you both a large debt of gratitude.

I would like to thank all the professors at Brown University for their guidance and assistance during my years as a graduate student. I would specifically like to thank my readers, Dr. William Curtin and Dr. Sharvan Kumar, for their support during my graduate studies and for their helpful critique of my dissertation. I would also especially like to thank Dr. Janet Blume, Dr. Eric Chason, Dr. Clyde Briant, Dr. Ben Freund, and Dr. Chris Bull for many helpful and engaging conversations. I would like to thank all the professors at Lafayette College for their assistance and guidance in developing the foundation of my engineering education, especially Dr. Jenn Rossmann, Dr. Scott Hummel, Dr. James Schaffer, Dr. Leonard Van Gulick, and Dr. Karl Seeler.

I would like to extend a warm thank you to my family, Mom, Dad, Susan, and Scott. You have been there for me and continue to be there for me in good times and bad. My unending thanks go to you for your love and support.

I would like to thank my friends for your unyielding support and encouragement. You have kept me sane throughout this process and brightened my days. For that I owe you my gratitude. To Jeff, Kellis, Evan, Sarah, Annie, Jim, Sinan, Yang, Dave, Isa,

Rassin, Vissu, Eric, Ningning, Indrek, Greg, Jennet, Sean, Vince, Padam, LeAnne, Yorgos, Maria, Sam, Mallery, Suzanne, Judy, George, Matt, Col, Roger, Nick, Maria, Liz, Megan, Dana, Emily, Adam, Erica, Alex, John, Kate, Erik, Megan, Patrick, Carey, Andrew, Katie, Amanda, Victoria, Paul, and lastly to Gwen. From the bottom of my heart, I thank you.

I would like to thank the support staff at Brown, Stephanie, Pat, Brian, Paul, and Tony, as well as the support staff at General Motors, Josh, Willie, Yan, Shruti, and Todd.

I would like to thank my collaborators at General Motors for your assistance and fruitful discussion on various aspects of this dissertation, Dr. Lou Hector, Dr. Yue Qi, Dr. Jon Carter, and Dr. Ravi Verma. Finally, I would like to thank the General Motors Company for funding my research through the Brown University / General Motors Collaborative Research Laboratory for Computational Materials Research.

*David Cipoletti*

# Table of Contents

<b>List of Tables</b>	<b>xi</b>
<b>List of Figures</b>	<b>xii</b>
<b>Chapter 1: Introduction</b>	<b>1</b>
1.1 General Properties of Superplasticity	10
1.2 Elevated Temperature Deformation Mechanism	14
1.3 Summary of Dissertation	17
<b>Chapter 2: Experimental Procedures and Results</b>	<b>31</b>
2.1 Experimental Procedures	34
2.1.1 Heat Treatment	34
2.1.2 Tensile Tests	34
2.1.3 Sample Preparation and Observation	37
2.2 Experimental Results	38
2.2.1 Material Specifications	38
2.2.2 Heat Treatment Effects	39
2.2.3 Elevated Temperature Tensile Tests	41

2.2.3.1 Pure Magnesium	41
2.2.3.2 Magnesium Alloy AZ31	43
2.3 Experimental Conclusions	46
<b>Chapter 3: The Finite Element Model</b>	<b>69</b>
3.1 Formulation of the Finite Element Model	70
3.1.1 Intragranular Dislocation Creep	71
3.1.2 Grain Boundary Diffusion	74
3.1.3 Grain Boundary Sliding	75
3.1.4 Grain Boundary Triple Junctions	76
3.1.5 Mechanical Equilibrium	77
3.1.6 Strain Rate Computations	79
<b>Chapter 4: Validation and Application of the Model to Magnesium Alloy AZ31</b>	<b>83</b>
4.1 Determination and Calibration of Model Parameters	85
4.2 Distribution of Strain Rate by Deformation Mechanism	89
4.3 Comparison of Magnesium and Aluminum	90
4.4 Conclusions from Model Calibration and Validation	92



## **Chapter 5: Application of the Model to Study Plastic Anisotropy in Magnesium Alloy AZ31 Extruded Sheet**

**100**

5.1 Application of the Model to Extruded Magnesium AZ31 Sheet Deformed at 450°C	102
5.1.1 Setup of Initial Conditions	103
5.1.2 Comparison of Computational and Experimental Results	104
5.1.3 Distribution of Strain Rate by Deformation Mechanism	105
5.1.4 Comparison of Grain Size and Orientation	107
5.1.5 Conclusions from Deformation at 450°C	109
5.2 Application of the Model to a Change in Temperature in Magnesium AZ31 Extruded Sheet	110
5.2.1 Comparison of the Model with Experiment	110
5.2.2 Distribution of Strain Rate by Deformation Mechanism	112
5.2.3 Conclusions from Application of the Model to Temperature	113
5.3 Discussion	114
5.4 Conclusions of the Anisotropy Study	117

## **Chapter 6: A Finer Examination of Grain Boundary Sliding**

**135**

6.1 Introduction and Motivation	135
6.2 Material Parameters and Deformation in Homogenous Material	137
6.3 The Effect of Grain Boundary Sliding Heterogeneity on Deformation	140
6.3.1 The Effect of $f$ on the Overall Constitutive Behavior	140
6.3.2 The Effect of $f$ on Flow Stress	141
6.3.3 The Effect of $f$ on the Transition in Deformation Mechanisms	142
6.4 The Influence of the Spatial Distribution of the Free Sliding Grain Boundaries	143
6.5 Discussion	143
6.6 Conclusions	145
<b>Chapter 7: Conclusions and Future Work</b>	<b>160</b>
7.1 Conclusions	160
7.2 Recommendations for Future Work	166
<b>References</b>	<b>168</b>

## List of Tables

Table 3.1: Elastic constants for magnesium (Freund and Suresh, 2003).

Table 4.1: Values for the material parameters used in the finite element simulations for magnesium alloy AZ31 (Barnett, 2003; Freund & Suresh, 2003; Frost & Ashby, 1982; Obara, Yoshinga, & Morozumi, 1973; Reed-Hill & Robertson, 1957; Ward Flynn, Mote, & Dorn, 1961; Yoo, Agnew, Morris, & Ho, 2001; Yoshinaga & Horiuchi, 1963).

Table 6.1: Values for material parameters used in the finite element simulations for aluminum alloy 5083.

# List of Figures

- Figure 1.1: Primary energy flow by source and sector in the United States in 2009 (U.S. Energy Information Administration, Annual Energy Review, Tables 1.3, 2.1b-2.1f, 10.3, and 10.4, August 19, 2010).
- Figure 1.2: The materials used in construction of a typical automobile over the past century (Taub, Krajewski, Luo, & Owens, 2007).
- Figure 1.3: The manufacturing process and material evolution of the front cradle structure of an automotive chassis over time. Number of parts necessary for final assembly of the chassis and overall weight listed in parenthesis (Taub et al., 2007).
- Figure 1.4: Complex parts formed from an aluminum alloy using superplastic forming processes (Chandra, 2002).
- Figure 1.5: An example of superplasticity in commercial bronze (a Cu-Al alloy). 8000% elongation is achieved without significant necking of the material (Chandra, 2002).
- Figure 1.6: Stress vs. strain curves from tensile tests at a constant strain rate of  $5.5 \times 10^{-4} s^{-1}$  performed at various temperatures (Yi, Zaefferer, & Brokmeier, 2006).
- Figure 1.7: Schematic of the bulge test apparatus: (b) is the full testing assembly, (a) details the sample positioning and its location in the assembly (Verma, Hector, Krajewski, & Taleff, 2009).
- Figure 1.8: Commercial magnesium AZ31B decklid inner panels formed using the QPF process. The panel in (a) used a material with a greater than 55mm dome height during bulge testing. The panel in (b) used a material with a less than 55mm dome height (Carter, Krajewski, & Verma, 2008).
- Figure 1.9: A decklid assembly for the Cadillac *STS*. (a) The decklid inner panel formed from magnesium AZ31B. (b) The decklid assembly from the inside. The inner panel is painted black. (c) The decklid assembly from the outside. The outer panel is made of hot blow formed aluminum alloy 5083. The spoiler is a polymeric material (Carter et al., 2008).
- Figure 1.10: A schematic of microstructure and texture evolution during plastic deformation (Chandra, 2002).
- Figure 1.11: A schematic of microstructure and texture evolution during superplastic deformation (Chandra, 2002).

Figure 1.12: Mode of failure (a) and microstructure evolution (b) in a sample deformed in the dislocation creep regime (top sample in (a), right sample in (b)) and the grain boundary sliding regime (bottom sample in (a), left sample in (b)) (Agarwal, Briant, Krajewski, Bower, & Taleff, 2007).

Figure 1.13: Creep behavior of fine grained materials (Nieh, 1997).

Figure 1.14: Schematic of the microstructure used in the finite element simulations.

Figure 2.1: Schematic of an elevated temperature test specimen.

Figure 2.2: The true stress vs. true strain curve for two cycles of a step strain rate test. The flow stress at a given strain for a specific strain rate is interpolated from the linear fits to the steady state stress at each strain rate.

Figure 2.3: Micrograph of as received 99.999% pure magnesium warm sheet rolled to a final thickness of 1.6mm.

Figure 2.4: Schematic of the extruded sheet, detailing the orientation of tensile specimens and the face observed during microscopy measurements.

Figure 2.5: Optical micrographs of the specimen orientated  $0^\circ$  to the ED (a) and  $90^\circ$  to the ED (b).

Figure 2.6: Pole figures (a) and texture map (b) for the specimen orientated with the tensile axis parallel to the extruded direction.

Figure 2.7: Pole figures (a) and texture map (b) for the specimen orientated with the tensile axis perpendicular to the extruded direction.

Figure 2.8: Micrographs of pure magnesium sheet annealed for 30 minutes at (a)  $350^\circ\text{C}$ , (b)  $400^\circ\text{C}$ , (c)  $450^\circ\text{C}$ . The average grain size is  $33\mu\text{m}$  at  $350^\circ\text{C}$ ,  $90\mu\text{m}$  at  $400^\circ\text{C}$ , and  $150\mu\text{m}$  at  $450^\circ\text{C}$ . The surface twins are due to polishing of the soft metal.

Figure 2.9: Micrographs of pure magnesium sheet annealed at  $450^\circ\text{C}$  for (a) 6 minutes, (b) 15 minutes, (c) 30 minutes, and (d) 60 minutes. The average grain size is  $141\mu\text{m}$  at 6 minutes,  $117\mu\text{m}$  at 15 minutes,  $150\mu\text{m}$  at 30 minutes, and  $127\mu\text{m}$  at 60 minutes. The surface twins are due to polishing of the soft metal.

Figure 2.10: Stress vs. strain curves for pure magnesium specimens tested at  $350^\circ\text{C}$  and  $450^\circ\text{C}$  at a constant strain rate to failure of  $0.1\text{s}^{-1}$  and  $0.001\text{s}^{-1}$ .

Figure 2.11: Micrographs from various points along a tensile specimen of pure magnesium pulled at a constant strain rate to failure of  $0.001\text{s}^{-1}$  at a constant

temperature of 450°C. Each micrograph exhibits the result of increasing amounts of strain from the top left counter clockwise to the bottom right.

Figure 2.12: Micrographs from various points along a tensile specimen of pure magnesium pulled at a constant strain rate to failure of  $0.001\text{s}^{-1}$ , at a constant temperature of 350°C. Each micrograph exhibits the result of increasing amounts of strain from the top left counter clockwise to the bottom right.

Figure 2.13: Average grain size shown as a function of the true strain measured in the thickness direction for pure magnesium tensile samples pulled at a constant strain rate of  $0.0001\text{ s}^{-1}$  to failure at 350°C and 450°C.

Figure 2.14: Strain rate as function of flow stress for pure magnesium tensile samples tested at 350°C, 400°C and 450°C. This plot was compiled from the results of the step strain rate tests.

Figure 2.15: A fourth set of data points have been added to the plot from figure 2.13 to show the effect of annealing temperature, and thus the effect of initial grain size, on the strain rate as a function of flow stress in pure magnesium.

Figure 2.16: Stress vs. strain curves for magnesium AZ31 specimens oriented with the tensile axis  $0^\circ$  and  $90^\circ$  to the extruded direction tested at 450°C at a constant strain rate to failure of  $0.1\text{s}^{-1}$  and  $0.001\text{s}^{-1}$ .

Figure 2.17: Fractured tensile specimens pulled at a constant strain rate of  $0.1\text{s}^{-1}$  to failure at 450°C. The tensile axis of (a) is orientated  $0^\circ$  to the ED and (b) is orientated  $90^\circ$  to the ED.

Figure 2.18: Strain rate as function of flow stress for the magnesium AZ31 specimens oriented so that the tensile axis is  $0^\circ$  and  $90^\circ$  to the extruded direction. This plot was compiled from the results of the step strain rate tests at 450°C.

Figure 2.19: Strain rate sensitivity,  $m$ , plotted as a function of strain rate for both orientations, compiled from the results of the step strain rate tests at 450°C.

Figure 2.20: Strain rate plotted as a function of stress for tensile test where the loading was  $0^\circ$  and  $90^\circ$  to the ED at 350°C and 450°C.

Figure 2.21: Activation energy for creep during elevated temperature tensile tests for both orientations of the tensile axis with respect to the ED plotted as function of stress.

Figure 3.1: Schematic of a grain boundary in the finite element model.

- Figure 4.1: Comparison of the simulation microstructure (a) and the experimentally obtained microstructure using EBSD (b) for the specimen orientated  $0^\circ$  to the ED. The tensile direction is horizontally to the right.
- Figure 4.2: Optical micrographs of the three magnesium AZ31 sheet specimens with average grain size (a)  $8\mu\text{m}$ , (b)  $16\mu\text{m}$ , and (c)  $50\mu\text{m}$ .
- Figure 4.3: Experimentally produced strain rate vs. stress curves compiled from step strain rate tests at  $450^\circ\text{C}$  for the  $8\mu\text{m}$ ,  $16\mu\text{m}$ , and  $50\mu\text{m}$  material.
- Figure 4.4: Computational and experimental strain rate vs. stress curves for the  $8\mu\text{m}$ ,  $16\mu\text{m}$ , and  $50\mu\text{m}$  material at  $450^\circ\text{C}$ . The simulation shows good fit to experiment.
- Figure 4.5: The predicted percent contribution to total strain rate from each deformation mechanism, DC, GBD, and GBS as a function of strain rate and average grain size at  $450^\circ\text{C}$ .
- Figure 4.6: The predicted percent contribution to the total strain rate due to dislocation creep from slip on the basal, prismatic and pyramidal slip system in magnesium as a function of strain rate and average grain size at  $450^\circ\text{C}$ .
- Figure 5.1: Comparison of the simulation microstructure (a) and the experimentally obtained microstructure using EBSD (b) for the specimen orientated  $90^\circ$  to the ED. The tensile direction is horizontally to the right.
- Figure 5.2: Computational and experimental flow stress curves for the AZ31 extruded sheet material tested at  $450^\circ\text{C}$  for the tensile axis rotated  $0^\circ$  or  $90^\circ$  from the extrusion direction. The simulation shows good fit to experiment.
- Figure 5.3: The predicted percent contribution to total strain rate from each deformation mechanism, DC, GBD, and GBS as a function of strain rate and orientation of the tensile axis at  $450^\circ\text{C}$ .
- Figure 5.4: The predicted percent contribution to the total strain rate due to dislocation creep from slip on the basal, prismatic and pyramidal slip system in magnesium as a function of strain rate and orientation of the tensile axis at  $450^\circ\text{C}$ .
- Figure 5.5: Computational flow curves for the simulations based on the actual micrographs of the differently oriented extruded magnesium AZ31 sheet and the fabricated simulations with alternate grain size and orientation at  $450^\circ\text{C}$ .
- Figure 5.6: The predicted percent contribution to the total strain rate due to dislocation creep from slip on the basal, prismatic and pyramidal slip system as a function of strain rate for the simulations based on the actual material and the

simulations based on a fabricated material with alternate grain size and orientation at 450°C.

Figure 5.7: The predicted percent contribution to total strain rate from each deformation mechanism, DC, GBD, and GBS as a function of strain rate and orientation of the tensile axis at 450°C with constant grain size of 9 $\mu$ m.

Figure 5.8: The predicted percent contribution to total strain rate from each deformation mechanism, DC, GBD, and GBS as a function of strain rate and orientation of the tensile axis at 450°C with constant grain size of 18 $\mu$ m.

Figure 5.9: Computational and experimental strain rate vs. stress curves for the AZ31 extruded sheet material oriented with the tensile axis 0° to the extruded direction tested at 350°C and 450°C. The simulation shows good fit to experiment.

Figure 5.10: Computational and experimental strain rate vs. stress curves for the AZ31 extruded sheet material oriented with the tensile axis 90° to the extruded direction tested at 350°C and 450°C. The simulation shows good fit to experiment.

Figure 5.11: The predicted percent contribution to total strain rate from each deformation mechanism, DC, GBD, and GBS as a function of strain rate and temperature for loading 0° to the ED.

Figure 5.12: The predicted percent contribution to total strain rate from each deformation mechanism, DC, GBD, and GBS as a function of strain rate and temperature for loading 90° to the ED.

Figure 5.13: The predicted percent contribution to the total strain rate due to dislocation creep from slip on the basal, prismatic and pyramidal slip system in magnesium AZ31 as a function of strain rate and temperature for loading 0° to the ED.

Figure 5.14: The predicted percent contribution to the total strain rate due to dislocation creep from slip on the basal, prismatic and pyramidal slip system in magnesium AZ31 as a function of strain rate and temperature for loading 90° to the ED.

Figure 6.1: Schematic of the microstructure used in the finite element simulations for aluminum alloy 5083.

Figure 6.2: Strain rate as a function of stress for multiple values of constant grain boundary fluidity  $\eta$ .



Figure 6.3: The predicted percentage contribution of total strain rate from dislocation creep, grain boundary diffusion and grain boundary sliding for simulations where  $\eta = 4.74 \times 10^{-8} \text{ m}^3 / \text{MN} \cdot \text{s}$  and  $\eta = 4.74 \times 10^{-12} \text{ m}^3 / \text{MN} \cdot \text{s}$ .

Figure 6.4: Plot of strain rate vs. stress for simulated results of varying percent of grain boundaries with allowable grain boundary sliding.

Figure 6.5: Plots for percent contribution to total strain rate for each deformation mechanism ((a) dislocation creep; (b) grain boundary diffusion; (c) grain boundary sliding) plotted for various values of  $f$ .

Figure 6.6: Plot of flow stress as a function of  $f$  for several values on constant strain rate.

Figure 6.7: Plots of the percent contribution to total strain rate attributed to each mechanism of plastic flow as a function of  $f$ , plotted at several constant strain rates:  $\dot{\epsilon} = 1.0 \times 10^{-3} \text{ s}^{-1}$ ,  $\dot{\epsilon} = 2.9 \times 10^{-4} \text{ s}^{-1}$ , and  $\dot{\epsilon} = 1.0 \times 10^{-4} \text{ s}^{-1}$ .

Figure 6.8: The strain rate where the transition in the dominant deformation mechanism between dislocation creep and grain boundary sliding plotted as a function of  $f$ .

Figure 6.9: Strain rate plotted as a function of stress for  $f = 54$  percent with different distributions of the grain boundaries that are allowed and restricted to slide.  $f = 100$  percent and  $f = 0$  percent are plotted for reference.

Figure 6.10: Distribution of the grain boundaries with allowed or restricted sliding aligned diagonally across the microstructure.

## **CHAPTER 1: INTRODUCTION**

It can be argued that the United States is dependent on fossil fuels to supply our energy demand. To report current energy statistics and historical trends, the U.S. Energy Information Administration produces the Annual Energy Review (U.S. Energy and Information Administration, 2009). Included in this report are data on energy production, consumption and trade as well as a breakdown of specific sources of energy. Figure 1.1 shows a visual distribution of the supply sources and demand sectors for the 94.6 quadrillion Btu of energy consumed in the United States in 2009. Although research into renewable energy sources has increased, the United States remains strongly reliant on non-renewable forms of energy, specifically carbon based sources. Petroleum sources account for the majority of our energy needs, 37 percent of our energy supply at approximately 21 million barrels per day, and the majority of that petroleum, 72 percent, is spent as fuel to power transportation of people and goods across the country. Within the scope of the transportation sector, about 9 million barrels per day is refined into motor gasoline for use in cars and trucks (U.S. Energy and Information Administration, 2009). Thus, if the United States is interested in decreasing its dependence on oil, decreasing vehicle fuel consumption would have a significant impact.

With an eye towards decreasing the United States' dependence on oil the government has enacted stricter regulations to push companies to develop more fuel efficient vehicles. In May 2010, the U.S. Environmental Protection Agency (EPA) and the National Highway Traffic Safety Administration (NHTSA) published the Light-Duty Vehicle Greenhouse Gas Emissions Standards and Corporate Average Fuel Economy Standards that they estimate will cut greenhouse gas emissions by 960 million metric tons and decrease fuel consumption by approximately 1.8 billion barrels of oil during the lifetime of vehicles encompassed by the program (U.S Environmental Protection Agency, 2011). This set of standards requires passenger cars, light-duty trucks, and medium duty passenger vehicles produced from 2012 to 2016 to have an estimated combined average emissions level of 250 grams of carbon per mile or less. If car companies were to meet this requirement by improving fuel economy (this could also be accomplished by removing more carbon from the engine exhaust), the standards are equivalent to requiring that vehicles get 35.5 miles per gallon (MPG). The EPA and NHTSA published standards for medium and heavy duty vehicles in November 2010 that are estimated to cut greenhouse gas emissions by 250 million metric tons and decrease oil consumption by 500 million barrels (U.S Environmental Protection Agency, 2011).

There are multiple avenues that the automobile industry can take to decrease fuel consumption by increasing the average MPG of its fleet to comply with the stricter regulations. These options include: development of more efficient gasoline and diesel engines, development of more efficient transmissions, increased use of hybrid and electric engines, reduction of vehicle weight, and reduction of vehicle drag. In 2008, The Laboratory for Energy and the Environment at the Massachusetts Institute of Technology

forecast that a 30-50% reduction in fuel consumption is possible within thirty years due to a combination of these solutions in their report, *On the Road in 2035* (Bandivadekar et al., 2008). If a focus is placed on reducing vehicle weight, which can have a significant effect on decreasing fuel consumption, especially in stop and go traffic, there are generally three paths that the automobile industry can take to develop lighter vehicles. One option would be to make smaller cars which would be inherently lighter than their larger counterparts. A second option would be to improve component design so that components require less material to serve the same function without compromising structure integrity or safety. Lastly, the automobile industry can design vehicles that utilize lightweight materials to serve the same function as components made from heavier materials (Bandivadekar et al., 2008). This dissertation intends to present results that will make the third option more viable.

Over the past forty years the automobile industry has steadily increased the amount of lightweight materials used in the average vehicle. The graph in figure 1.2 shows the percent composition of various materials in a typical automobile over the past century. In 1906, before the introduction of Ford's Model T in 1908, the typical automobile was made mostly from wood, but as the automobile became more commonplace low-carbon steel quickly became the material of choice. Due to its low cost, ease of use during manufacture, and high strength it has remained that way for the better part of the last century (Taub, Paul E. Krajewski, Luo, & Owens, 2007g). The major drawback of steel is its relatively high density which increases vehicle weight. When gasoline was inexpensive this was of little concern to the automobile companies or consumers. However, due to the oil crisis of 1973 gasoline quickly rose in price and

gasoline rations prevented large consumption of gasoline causing consumers to quickly become aware of the gas guzzling nature of their cars and trucks. Further incentives for more fuel efficient cars were initiated by the Clean Air Act of the 1963 and its substantial expansion in 1970, which placed restrictions on automobile emissions in response to environmental movements. In reaction to the increased demand for lighter more gas efficient vehicles the average curb weight of automobiles in the United States dropped from 3,620 pounds to 2,870 pounds from 1975 to 1980, and the high percentages of low-carbon steel in automobiles started to decline (Buckingham, 2006).

To increase fuel efficiency by reducing vehicle curb weight a broader range of materials have been adopted by the automobile industry. Figure 1.2 shows how over the past century the amount of low-carbon steel in an average vehicle has decreased as the use of other materials has increased. Specifically, the use of aluminum in automobiles has steadily increased over the past 40 years as a light weight alternative to steel. The average aluminum content per vehicle in the United States increased from 82.2 pounds in 1970 to 289 pounds in 2004 and continues to rise (Buckingham, 2006). Aluminum is approximately one third as dense as steel ( $\rho_{Al} = 2.66 \text{ g/cm}^3$ ,  $\rho_{Steel} = 7.86 \text{ g/cm}^3$ ), which provides substantial weight savings. Besides their lightweight advantage aluminum alloys have relatively high strength (for aluminum alloy 5083:  $E = 70.3 \text{ GPa}$ ,  $G = 26.4 \text{ GPa}$ ,  $\sigma_Y = 250 \text{ MPa}$ ,  $\sigma_{UTS} = 320 \text{ MPa}$ ), good energy absorption characteristics during impact, good resistance to corrosion, and high thermal and electric conductivity. They are also extremely recyclable; approximately 60 percent of the aluminum in new cars has been recycled and 90 percent of the aluminum in scraped vehicles is recovered and recycled (Buckingham, 2006).

In addition to aluminum, magnesium alloys are also being developed as a lightweight alternative to steel. Magnesium ( $\rho_{\text{Mg}} = 1.77 \text{ g/cm}^3$ ) is approximately 25 percent as dense as steel and two thirds as dense as aluminum, allowing for more substantial weight savings. It has relatively high strength (for magnesium alloy AZ31:  $E = 45 \text{ GPa}$ ,  $G = 17 \text{ GPa}$ ,  $\sigma_Y = 221 \text{ MPa}$ ,  $\sigma_{\text{UTS}} = 290 \text{ MPa}$ ) and has the characteristics to become a highly recyclable material if production increased. Magnesium alloys also show excellent damping characteristics, ideal to help build a smoother running vehicle. At present there is limited use of magnesium in the automobile industry but recent developments including the work presented here aim to change that.

One automotive application of aluminum and magnesium alloys has been in the design of lightweight chassis (Alan I. Taub et al., 2007g). Traditionally, chassis are made of steel by welding together multiple extruded and stamped components. Aluminum and magnesium alloys offer two distinct advantages over their steel counterpart. In addition to the substantial weight savings due to their lower density, they exhibit good material flow at molten temperatures, and thus are excellent for use in die casting. This has allowed for chassis to be designed using fewer components which led to improved cycle times during production (Alan I. Taub et al., 2007g). Figure 1.3 exhibits several examples of chassis designs over the past decades, showcasing the gradual transition from steel to magnesium chassis design.

Aluminum and magnesium alloys are also being utilized in the automotive industry for body applications. In the past vehicle body components have been made almost exclusively from cold-rolled low-carbon steel sheet because of its high strength and excellent formability. These characteristics allow steel sheet components to be

stamped at room temperature with quick cycle times, which in addition to its low cost, make it an ideal choice financially. Aluminum and magnesium alloy sheet material is significantly more expensive and significantly less formable than steel. This generates two challenges that must be overcome if the substantial weight savings that the automobile industry could incur through increased use of aluminum and magnesium alloys in construction of body panels can be achieved. Due to the rising cost of oil which has led to higher savings for more fuel efficient vehicles, the roadblock due to cost differences in the materials has converged to an extent. Advantages in marketing novel materials has also helped to close the cost gap between steel and aluminum or magnesium alloys by making them more attractive to consumers. The second issue is more innate to the properties of each material; however, many advances have been made to address the decreased formability of aluminum and magnesium alloys. A multitude of alternative forming processes have been attempted to increase formability, including: superplastic forming, quick plastic forming, hydroforming, thermohydroforming, warm forming, roller hemming, retrogression heat treatment, electromagnetic forming, and preform annealing (Alan I. Taub et al., 2007g).

Superplastic forming (SPF) is a hot blow forming process that utilizes the unique characteristics of superplasticity to make geometrically complex parts (Barnes, 1994, 2007). Examples of the complex shapes that can be formed by SPF are shown in figure 1.4. Superplasticity is defined as the ability of polycrystalline materials to exhibit very high tensile elongations prior to failure in a generally isotropic manner (Chandra, 2002). An extreme example of superplasticity is shown in figure 1.5, in which Highashi obtained 8000 percent elongation in commercial bronze. Most materials will only undergo

superplastic deformation under specific conditions and otherwise will deform plastically. In general for superplastic deformation to occur the material must be deformed at a temperature greater than 50 percent of the melting temperature ( $T/T_M > 0.5$ , where  $T_M$  is the melting point) and low strain rates, generally on the order of  $1.0 \times 10^{-4} s^{-1}$ .

The superplastic forming process is capable of producing body panels out of lightweight materials that meet strength and safety regulations, but to be viable in the automobile industry, the process must be able form parts on the order of 100,000 panels per year. That equates to about 2-3 minutes per panel and strain rates for forming on the order of  $0.001 s^{-1}$  to  $0.01 s^{-1}$  (Alan I. Taub et al., 2007g). These requirements led the General Motors Company (GM) to develop the quick plastic forming (QPF) process (Paul E. Krajewski & Morales, 2004c; Paul E. Krajewski & Schroth, 2007d; Schroth, 2004). QPF is a hot blow forming process that achieves similar formability to SPF at lower temperatures ( $450^\circ C$ ) and faster strain rates ( $>0.001 s^{-1}$ ) for specific materials therefore enabling increased production volume (Paul E. Krajewski, 2004). Extensive research has been done to fine tune the process for commercial grade aluminum alloy 5083 (Agarwal, Paul E. Krajewski, & Briant, 2004a; Kulas, Green, Pettengill, Paul E. Krajewski, & Taleff, 2004e). AA5083 is a relatively inexpensive aluminum sheet material which lowered material costs, making QPF aluminum parts economically feasible. To further decrease vehicle weight, research is currently being done to develop the QPF process for magnesium alloys.

As previously mentioned, similar to aluminum alloys, magnesium alloys do not exhibit acceptable formability at room temperature. However, studies have shown that magnesium alloy AZ31 shows promise for elevated temperature forming applications of



sheet material. As temperature is increased there is a substantial increase in the ductility of magnesium alloy AZ31 as can be seen in figure 1.6 (Yi, Zaefferer, & Brokmeier, 2006). Furthermore, Kim et al. documented in their work that a superplastic response of rolled magnesium AZ31 sheet is possible at elevated temperatures (Kim, S. W. Chung, C. S. Chung, & Kum, 2001) This is due to activation of additional deformation mechanisms at elevated temperature including grain boundary sliding and grain boundary diffusion, and decreased critical resolved shear stress on the available slip systems. At room temperature slip is limited to the basal slip system, whereas at elevated temperature the prismatic and pyramidal slip systems are activated at significantly lower stresses, allowing for greater movement of dislocations by cross slip due to intersecting slip planes and thus greater ductility (Wu & Liu, 2002). The increase in the GBS mechanism at elevated temperature is paramount to increasing ductility, however, an accommodation mechanism is necessary for GBS to occur (Langdon, 2006; Valle, Pérez-Prado, & Ruano, 2005). Thus, increased dislocation creep and grain boundary diffusion are also needed for increased GBS. By observing microstructure evolution in tensile specimens of magnesium AZ31 tested at elevated temperatures, Panicker et al. concluded that superplastic deformation was attainable due to grain boundary sliding, while dislocation creep coupled with some grain boundary sliding was largely responsible for non-superplastic deformation (Panicker, Chokshi, Mishra, R. Verma, & P.E. Krajewski, 2009f).

Elevated temperature biaxial bulge forming tests have been instrumental in evaluating the superplastic response of various materials, especially in terms of their potential for sheet metal forming. This test is described in detail by Bradley, but in

summary it consists of applying a constant gas pressure to a secured sheet so that a dome forms and eventually ruptures at its peak (Bradley, 2004). The dome height can be measured along with the final thickness of the sheet at various positions. A schematic of the bulge testing apparatus is shown in figure 1.7. General Motors has used this test extensively to test the suitability of a material for its QPF process. Specifically, for an aluminum alloy to be considered for sheet forming GM requires a dome height of 55 mm. Magnesium alloy AZ31 sheet, processed using various techniques to adjust the starting microstructure, were tested under the same specifications of the existing QPF infrastructure for aluminum in an effort to jumpstart the magnesium QPF process. It was determined that multiple samples achieved the 55mm dome height and that one in particular, commercial grade direct cast (DC) AZ31B with an H24 temper with an 8-10 $\mu$ m grain size, compared well to AA5083, the alloy used extensively for aluminum QPF processes (Carter, Paul E. Krajewski, & Ravi Verma, 2008b). Due to the promising results these samples were used to form decklid inner panels using the QPF process, the results of which can be seen in figure 1.8. The panel in figure 1.8a is formed using the material described above; whereas the panel in figure 1.8b is characteristic of sheet material that did not pass the 55mm dome height specification (Jon T. Carter et al., 2008b). Failure occurs due to extensive thinning because of the sharp entry radius to the pocket of the die and friction between the sheet and die. As the material attempts to flow over the die entry radius a compressive force develops due to friction at the radius while the sheet is in tension, causing thinning and eventually fracture in less ductile materials. Finite element simulations of the QPF process for biaxial bulge forming tests, and forming into a die were used to formulate these conclusions and improve understanding

of the process (Ravi Verma, Hector, Paul E. Krajewski, & Taleff, 2009). Overall, this work showed that if a conservative strain rate is used with the right processing, magnesium AZ31 can be used to form body panels. Furthermore, it has allowed GM to achieve production capabilities for magnesium body panels. Magnesium AZ31 is presently being used in the Cadillac STS decklid inner panel, shown in figure 1.9 (Jon T. Carter et al., 2008b). In spite of this success, questions remain and improvements are necessary. Although the process is mechanically possible, the strain rate needs to be increased (to decrease cycle time) and temperature of formation needs to be decreased to make use of magnesium panels more economically viable. To do this the deformation mechanisms of magnesium at elevated temperature and the microstructural characteristics that affect them need to be understood.

It is useful to begin with a more detailed description of superplasticity and the mechanisms involved to provide a solid technical background to this work.

## **1.1 General Properties of Superplasticity**

A common way to characterize tensile deformation in a material is to determine its strain rate sensitivity, which is commonly defined by the following equation:

$$\sigma = C \dot{\epsilon}^m \quad (1.1)$$

where  $m$  is the strain rate sensitivity,  $\sigma$  is the flow stress,  $C$  is a constant, and  $\dot{\epsilon}$  is the strain rate. For reference, a material that exhibits ideal Newtonian viscous behavior has  $m = 1$ . For most metals, generally if the strain rate sensitivity is less than 0.2 the material exhibits plastic deformation, and for  $m > 0.3$  the deformation is generally superplastic,

but this is not always the case (Nieh, 1997). Within the realm of superplasticity in polycrystalline materials, there are two classes: Fine-structure superplasticity (FSS) and internal-stress superplasticity (ISS). Some consider high-strain-rate superplasticity (HSRS) to be a third class, however, it can be considered as an extension of fine-structure superplasticity applied to high strain rates on the order of  $10^{-1}$  to  $10^1 \text{s}^{-1}$  (Nieh, 1997). Due to the high strain rates of HSRS there is potential for fast forming applications but it is not applicable for the materials discussed in this work. ISS achieves the high strain rate sensitivity values necessary for superplasticity by thermal cycling or pressure cycling of specific materials that generate internal stresses which drive deformation by a slip controlled process. However, FSS is the most common and most studied of the two classes of superplasticity, and the work presented in this dissertation falls under this general class of materials. FSS has the following characteristics which will be introduced here to serve as a backbone to this work.

For a material to deform by fine-structure superplasticity the strain rate sensitivity is on the order of 0.5 and the dominant deformation mechanism is grain boundary sliding (GBS). Grain boundary sliding will be discussed in more detail in the next section, but in general, it is more prevalent for smaller grain sizes. Thus, the strain rate below which superplasticity will occur increases as grain size decreases. Specifically for most materials the strain rate at which superplastic deformation will occur as a function of grain size is described by the following relation,

$$\dot{\epsilon} \propto d^{-p} \tag{1.2}$$

where  $d$  is grain size and  $p$  is a constant (Nieh, 1997). For magnesium alloys  $p = 3$ .

A corollary to the need for small grain sizes for superplastic behavior is that the

material contains a second phase. When a single phase material is placed under tension and especially at elevated temperature the increase in energy causes rapid grain growth. The enlarged grains decrease the prevalence of grain boundary sliding, thus decreasing the likelihood of a superplastic response. When the material contains a second phase, which in many cases is made up of hard particles that gather at grain boundaries, grain growth is limited, decreased grain size is preserved, and superplastic behavior is not suppressed.

The grain boundaries in a material usually have specific characteristics that make grain boundary sliding and thus superplasticity more likely to occur. GBS is more prevalent along high energy grain boundaries rather than low energy grain boundaries. An equiaxed grain structure supports extensive GBS by increasing the likelihood that grain boundaries can be subjected to shear stress which initiates sliding. Grain boundary mobility is also important for grain boundary sliding, so that if adjacent grains are prevented from sliding against one another due to an obstruction, the grain boundary can migrate and continue sliding. This ability of the GBS mechanism to bypass an obstacle is extremely important, so much so that models to describe GBS are usually defined by their accommodation mechanism, which will be explained momentarily. Each of these characteristics has been observed in superplastic materials and will be demonstrated in the following work for magnesium alloys.

The effect of grain boundary sliding leads to different microstructure evolution between superplastically and plastically deformed materials. During GBS, the sliding between adjacent grains allows individual grains to change neighbors during deformation. This process helps the grains to remain equiaxed or to become equiaxed if

the microstructure was strongly textured to begin with (Chandra, 2002). This process is illustrated in figure 1.10. Grains move amongst each other by GBS and an additional accommodation mechanism to accommodate the induced strain in the microstructure while the texture remains weak. This is in stark opposition to plastic deformation, illustrated in figure 1.11. In this case grain boundary sliding is not prevalent, and thus neighboring grains remain adjacent to each other. The induced strain in the microstructure must be accommodated by stretching of the individual grains through dislocation motion which elongates the grains. This also causes the grains to rotate so that they align themselves along the principal direction, causing a strong texture to develop. As can be seen by observing the final microstructure in figure 1.10 and figure 1.11 the microstructure evolution of a plastically deformed solid and a superplastically deformed solid differs substantially (Chandra, 2002).

The failure mechanisms for plastically and superplastically deformed solids show stark differences as well. Plastically deforming materials commonly fail due to a necking process. Geometric or material weak points in the material cause a strain to increase in the localized area which leads to a reduced cross section. This in turn leads to an increase in stress which leads to a subsequent increase in strain, further localized thinning of the material, and eventual failure due to repeated occurrence of this process. Superplastic materials generally fail due to vacancy coalescence. Vacancies form from separation of adjacent grains due to inadequate accommodation of GBS. These vacancies usually form at triple junctions, grain boundary ledges, or particles on the grain boundary, and eventually coalesce to sufficient size and quantity to cause failure. Necking is not observed in superplastically deformed materials because GBS allows for greater

distribution of the localized increase in stress, which discourages the start of the necking process (Chandra, 2002).

An example of these differences is observed in the microstructure evolution and failure criteria for aluminum alloy 5083 deformed under conditions for superplastic and plastic deformation, as shown in figure 1.12. All tests were performed at 450°C but one sample was deformed at a strain rate of  $0.03\text{s}^{-1}$  which is within the dislocation creep regime of the stress vs. strain rate curve and the second sample was deformed at a strain rate of  $0.0005\text{ s}^{-1}$  which is within the grain boundary sliding regime (Agarwal, Briant, Paul E. Krajewski, Bower, & Taleff, 2007). For deformation at the high strain rate the sample shows necking prior to failure and a strong texture develops in the microstructure, whereas for the low strain rate there is little necking prior to failure and the microstructure remains equiaxed.

At this point, after an explanation of the general characteristics of superplastic deformation, it is advisable to take a closer look at the deformation mechanisms involved. For it is these mechanisms that are at the core of how superplastic deformation functions and how formability can be improved for magnesium.

## **1.2 Elevated Temperature Deformation Mechanisms**

Creep is the process of plastic deformation that occurs when a material is subjected to stress for an extended period of time at elevated temperature without initially forming cracks or voids. At the microstructural level creep is associated with the following three deformation mechanisms: dislocation movement on individual slip

systems, sliding of adjacent grains along their common grain boundary, and diffusion of material due to stress gradients (Nieh, 1997). If a material is subjected to an imposed strain rate at elevated temperature so that the specimen deforms due to creep, the relationship between the strain rate and the subsequent flow stress can be modeled using the following equation,

$$\dot{\epsilon} = A\sigma^n \quad (1.3)$$

where  $A$  is a constant and  $n$  is the stress exponent. The stress exponent is equivalent to  $1/m$ , where  $m$  is the strain rate sensitivity defined in eq. 1.1. The dominant deformation mechanism associated with creep in the material is characterized by the value of the stress exponent for a specified range of strain rates. Diffusional creep is associated with a stress exponent,  $n = 1$ . Deformation by diffusional creep occurs by the diffusion of atoms from areas of the material under compression to those under tension. When the diffusion occurs through the grain lattice it is referred to as Nabarro-Herring creep, and when it occurs along grain boundaries it is referred to as Coble creep (Coble, 1963; Nieh, 1997).

When the stress exponent rises to between three and five, deformation is associated with dislocation creep, which is defined by the movement of dislocations to accommodate the strain induced in the material. A stress exponent,  $n = 3$ , is typical of dislocation creep limited by glide of dislocations along the slip plane, whereas a stress exponent,  $n = 4$  to  $5$  is associated with dislocation creep limited by climb of dislocations. When  $n = 2$  ( $m = 0.5$ ), creep is contributed to grain boundary sliding and deformation is considered to be superplastic.

Grain boundary sliding describes deformation by which adjacent grains slide against one another along their common grain boundary due to a resolved shear stress on



the boundary. This action is known to play an important part in superplastic deformation, and thus extensive research has been done to investigate the nature of GBS.

Geometrically it is not possible for GBS to act as the sole method of deformation, for if this was the case, adjacent grains would be forced to separate most likely at triple junctions (where three grain boundaries meet) to permit sliding, causing the material to fail prematurely. Thus, an accommodation mechanism is usually associated with GBS that allows sliding to take place without void creation. To describe deformation by GBS a number of models have been proposed, each of which consider a specific accommodation mechanism (Langdon, 2006). In general the various models can be grouped by their accommodation mechanism: grain boundary sliding accommodated by diffusion commonly referred to as Lifshitz sliding (Lifshitz, 1963), grain boundary sliding accommodated by dislocation creep commonly referred to as Ratchinger sliding (Ratchinger, 1952), and grain boundary sliding accommodated by itself, grain boundary migration or recrystallization. There are many models that describe diffusion controlled GBS including the work of Raj and Ashby, Ashby and Verral, Ashby et al., and more recently, Yang and Wang (Ashby, Edward, Davenport, & Verrall, 1978; Ashby & Verrall, 1973; Raj & Ashby, 1971; Yang & Wang, 2004). Models that describe dislocation creep controlled GBS are greater in number and include the work of Ball and Hutchinson, Mukherjee, Langdon, Hayden, Gifkins, Gittus, Kaibyshev, and Ghosh (Ball & Hutchinson, 1969; Ghosh, 1994; Gifkins, 1976; Gittus, 1977; Hayden, Floreen, & Goodell, 1972; Kaibyshev, Valiev, & Emaletdinov, 1985; Langdon, 1970; Mukherjee, 1971).

Creep behavior can be explained by a log plot of strain rate vs. flow stress, as

shown in figure 1.13, which captures how the combination of multiple mechanisms affects deformation. The plot shown here explicitly shows the independent relationship between grain boundary sliding, depicted as the dotted line, and power-law creep, depicted as the thin black line; the faster mechanism dominates deformation which is depicted as the thick black line. At high strain rates creep dominates deformation in the area referred to as region III. As the strain rate is decreased, the dominant deformation mechanism transitions to grain boundary sliding, region II on the plot. In this plot a threshold stress is shown for grain boundary sliding. When the stress drops below this threshold, grain boundary sliding is suppressed and the strain rate decreases drastically over a small decrease in stress as shown in region I (Nieh, 1997).

### **1.3 Summary of Dissertation**

There has been extensive experimental work with magnesium alloys to analyze elevated temperature deformation mechanisms and their effect on superplastic behavior. Experiments show that the elevated temperature deformation mechanisms in magnesium are strongly sensitive to microstructure. For example Vespa et al. (Vespa et al., 2008) showed how different starting microstructures influenced the tensile response to an imposed strain rate at elevated temperature. Verma analyzed the difference between direct-chill and continually-strip cast sheet, and attributed the difference in the deformation behavior of these materials to microstructural changes imposed by the two casting techniques (Ravi Verma, Carter, & Paul E. Krajewski, 2009). This sensitivity suggests that the microstructure of magnesium alloys can be designed to optimize their

formability.

The development and implementation of a computational model can be used as an aid in understanding the deformation mechanisms (Bower & Wininger, 2004; Pan & Cocks, 1993). A constitutive model was developed for deformation of hcp materials that accounts for dislocation creep and twinning, and was applied to study room temperature deformation of magnesium AZ31 (Staroselsky & Anand, 2003). Prakash et al. developed a crystal plasticity code to model the evolution of texture and grain shape in a microstructure representative of magnesium alloy AZ31 during plane strain compression with and without pyramidal slip active, which in essence corresponds to high and low temperature deformation (Prakash et al., 2009). Beausir et al. use similar constitutive laws to those used in the aforementioned publications along with those used in this work to make conclusions on the stress state in a crystal due to an imposed strain rate (Beausir, Toth, & Neale, 2007). Recently, Raeisinia developed a crystal plasticity model that correctly models slip system constitutive data in parity with single crystal data that also accounts for grain size dependence (Raeisinia & Agnew, 2010).

Keeping in mind the promise for improved forming of magnesium alloys due to microstructure design and prospect of computational models for development, a microstructure based model, originally developed for face centered cubic (fcc) materials, has been modified to model elevated temperature deformation mechanisms in magnesium, which has a hexagonal close packed (hcp) atomic stacking structure. The model extends a two-dimensional finite element method for modeling high temperature deformation in polycrystals described in reference (Bower & Wininger, 2004). The microstructure of magnesium is idealized as a two-dimensional assembly of grains,

separated by sharp grain boundaries, as shown in Fig. 1.14. The model accounts for three deformation mechanisms: dislocation creep within grains, as well as grain boundary sliding and grain boundary diffusion along the grain boundaries. As described previously, it is common to describe grain boundary sliding in association with its accommodation mechanism, however in the model framework presented here, this coupling occurs naturally by enforcing equilibrium and compatibility during deformation through the finite element method. This methodology should allow for a better understanding of the deformation mechanism and their relationship during elevated temperature forming. The model is used to predict the detailed distribution of stress and strain within the microstructure, as well as the macroscopic flow stress as a function of strain rate and grain size.

The remainder of this dissertation will be organized as follows. First there will be a detailed description of the experimental work that was completed to obtain a base characterization of magnesium and to provide experimental results to validate the model. Second, the finite element model will be described in detail, including the constitutive laws used in modeling the various elevated temperature deformation mechanisms. Next the results of the model will be presented in relation to the experimental data. This will include a discussion of the modeling results applied to experimental tensile test data for 8 $\mu$ m, 16 $\mu$ m, and 50 $\mu$ m magnesium AZ31 sheet material which was used to calibrate and validate the model. Results are presented from a study of the model applied to extruded magnesium AZ31 sheet with a strong texture in an attempt to determine the effects of texture and grain size. The model has also been applied in a grain boundary sliding study to further research this important mechanism. Finally, conclusions will be presented and

future directions for research will be discussed.

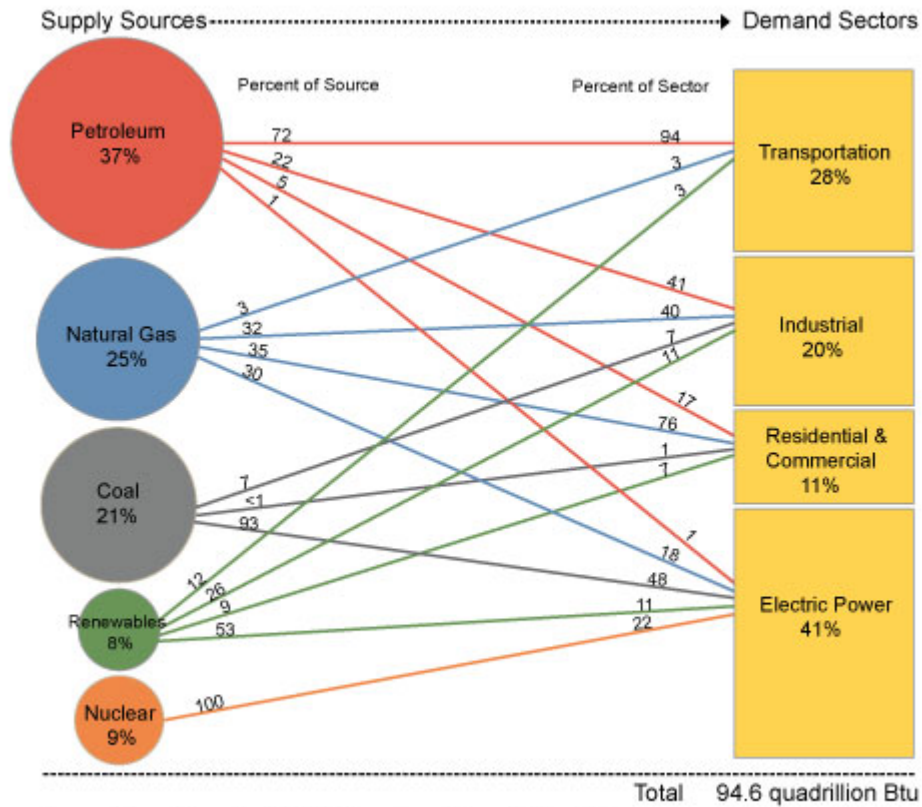


Figure 1.1: Primary energy flow by source and sector in the United States in 2009 (U.S. Energy Information Administration, [Annual Energy Review 2009](#), Tables 1.3, 2.1b-2.1f, 10.3, and 10.4, August 19, 2010).

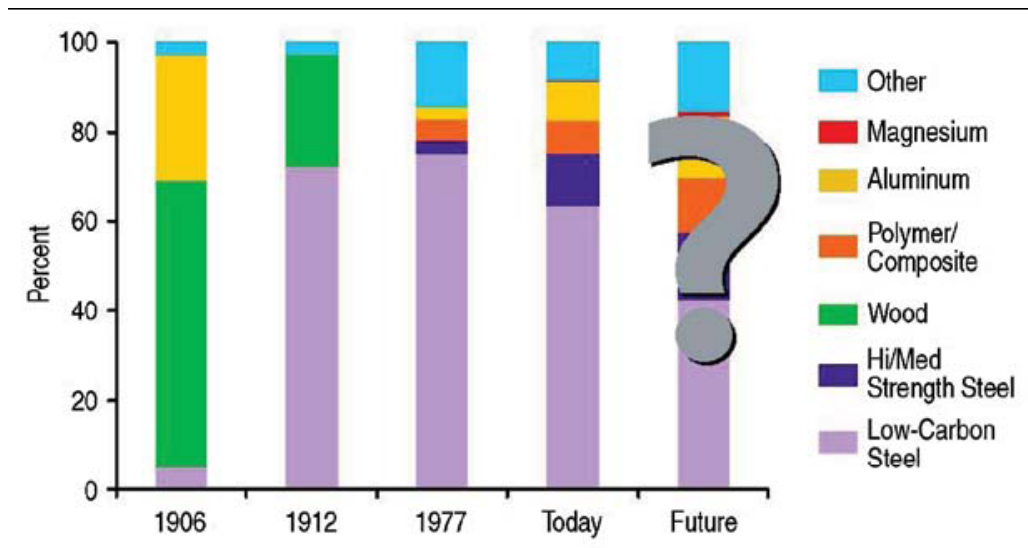
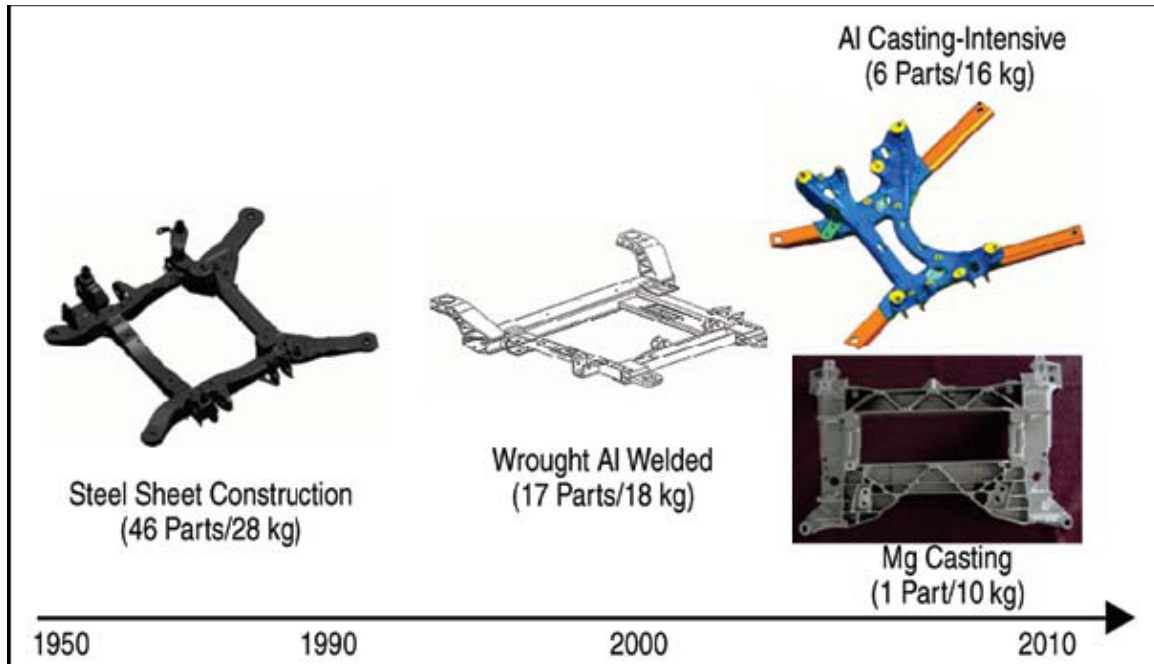


Figure 1.2: The materials used in construction of a typical automobile over the past century (Taub, Krajewski, Luo, & Owens, 2007).



The manufacturing process and material evolution of the front cradle structure of an automotive chassis over time. Number of parts necessary for final assembly of the chassis and overall weight listed in parenthesis (Taub et al., 2007).



Figure 1.4: Complex parts formed from an aluminum alloy using superplastic forming processes (Chandra, 2002).

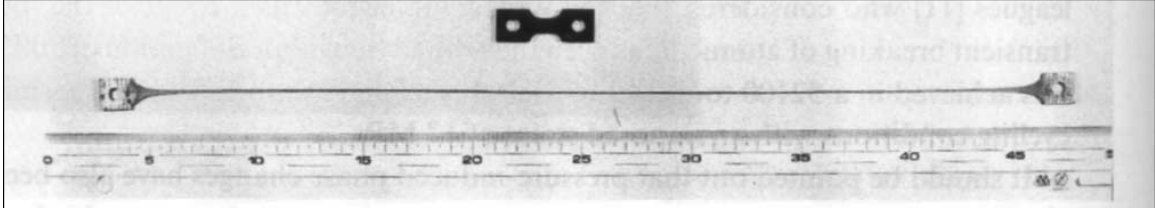


Figure 1.5: An example of superplasticity in commercial bronze (a Cu-Al alloy). 8000% elongation is achieved without significant necking of the material (Chandra, 2002).

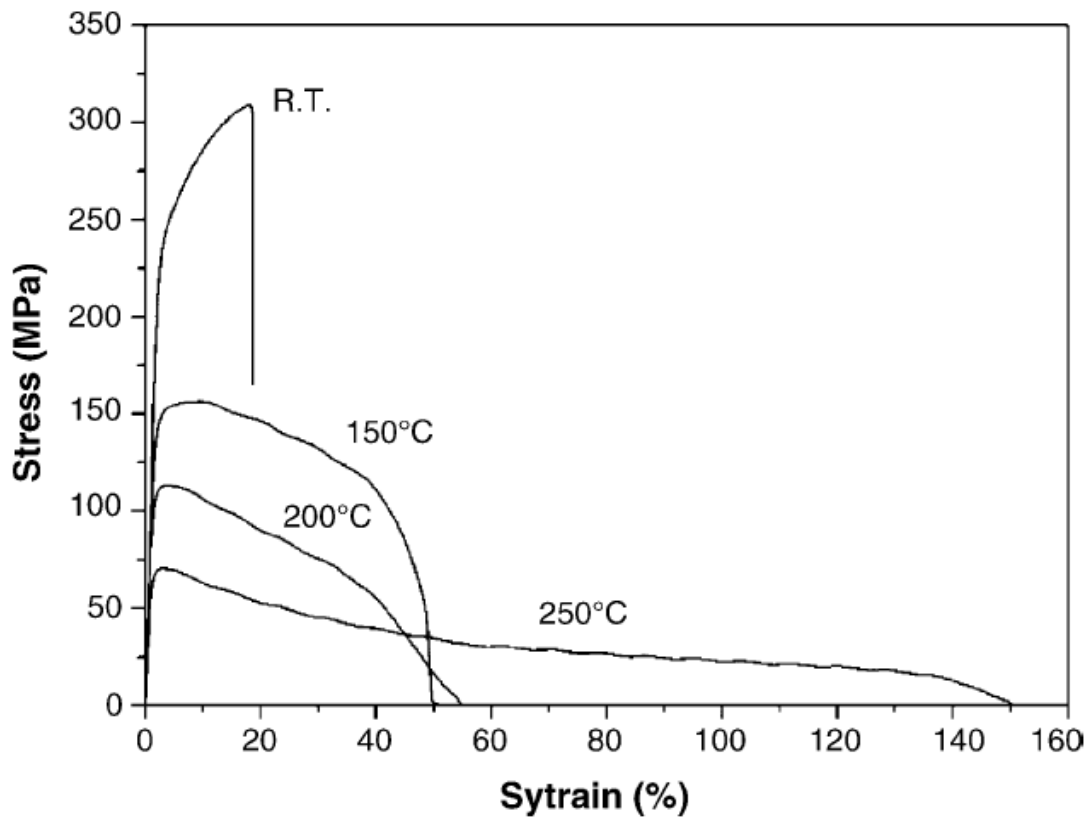


Figure 1.6: Stress vs. strain curves from tensile tests at a constant strain rate of  $5.5 \times 10^{-4} s^{-1}$  performed at various temperatures (Yi, Zaefferer, & Brokmeier, 2006).



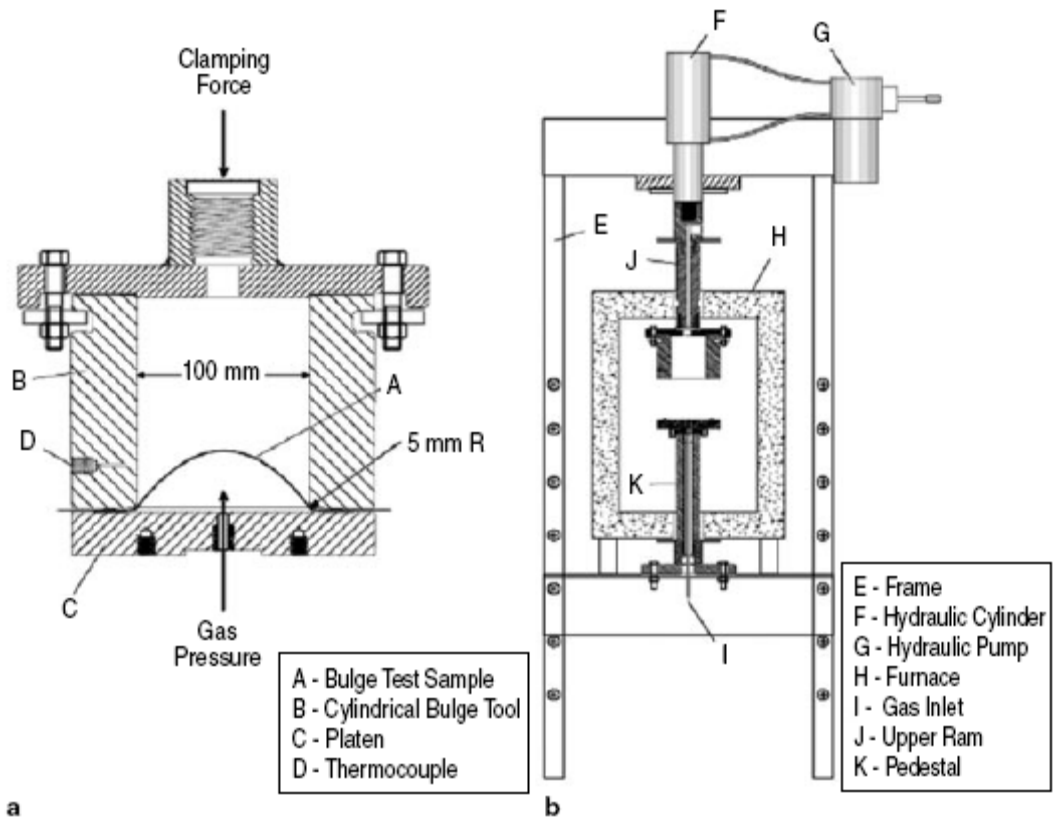


Figure 1.7: Schematic of the bulge test apparatus: (b) is the full testing assembly, (a) details the sample positioning and its location in the assembly (Verma, Hector, Krajewski, & Taleff, 2009).

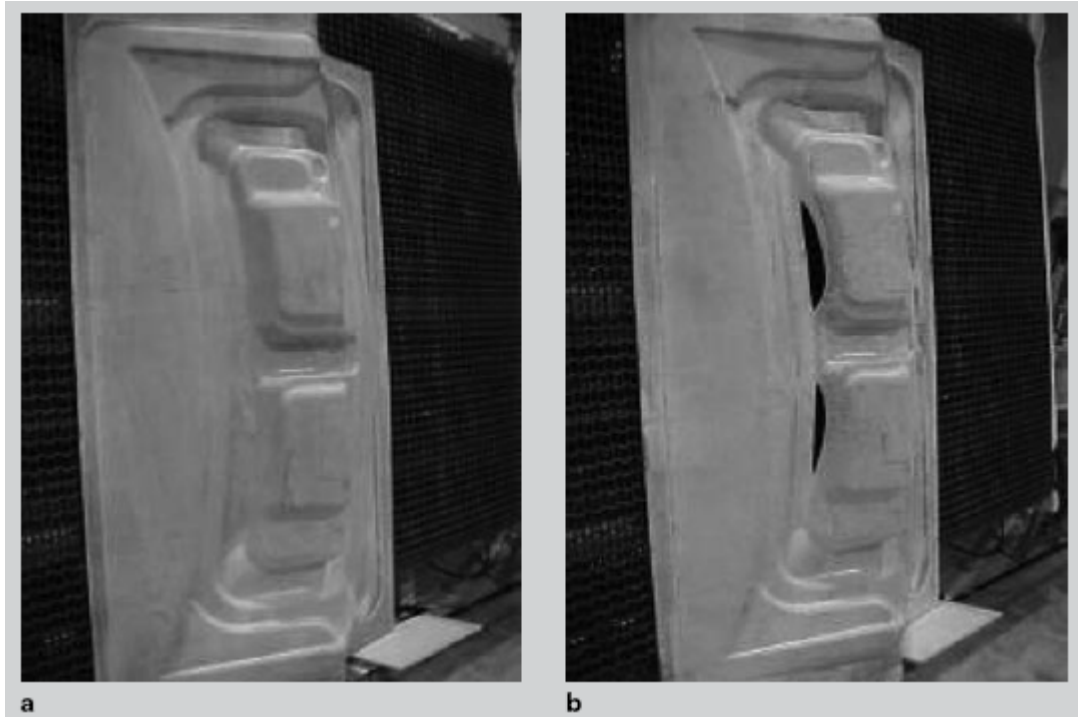


Figure 1.8: Commercial magnesium AZ31B decklid inner panels formed using the QPF process. The panel in (a) used a material with a greater than 55mm dome height during bulge testing. The panel in (b) used a material with a less than 55mm dome height (Carter, Krajewski, & Verma, 2008).

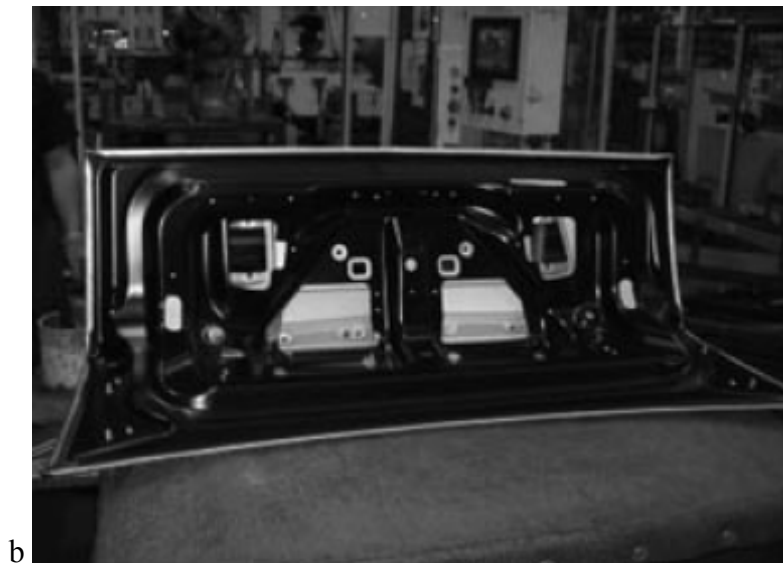


Figure 1.9: A decklid assembly for the Cadillac *STS*. (a) The decklid inner panel formed from magnesium AZ31B. (b) The decklid assembly from the inside. The inner panel is painted black. (c) The decklid assembly from the outside. The outer panel is made of hot blow formed aluminum alloy 5083. The spoiler is a polymeric material. (Carter, Krajewski, et al., 2008).

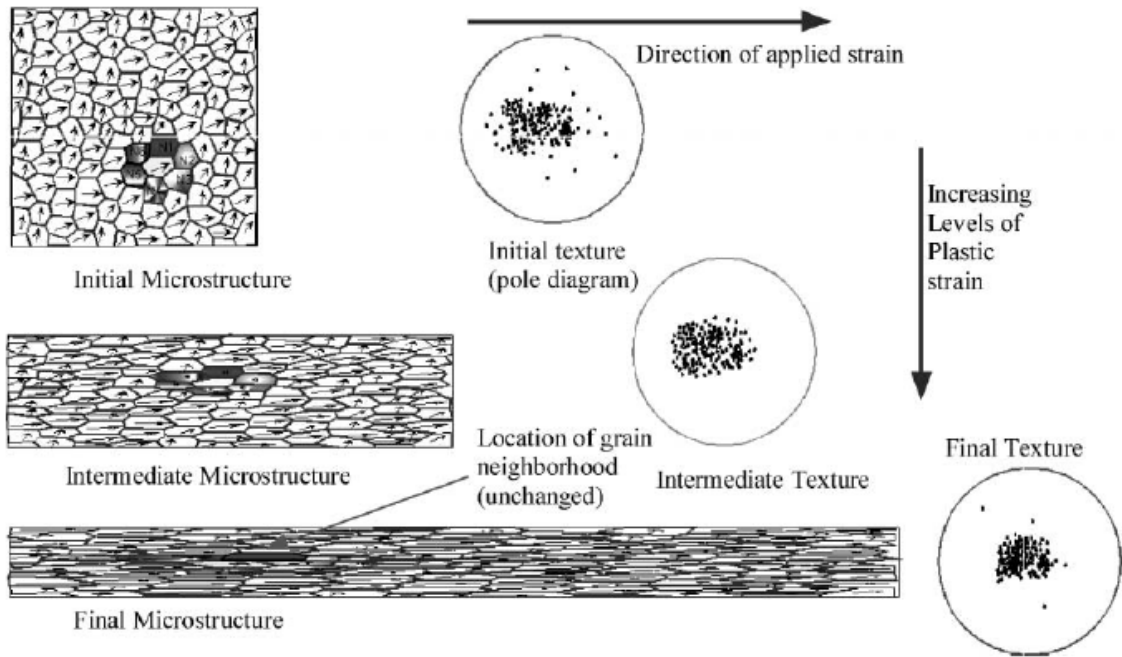


Figure 1.10: A schematic of microstructure and texture evolution during plastic deformation (Chandra, 2002).

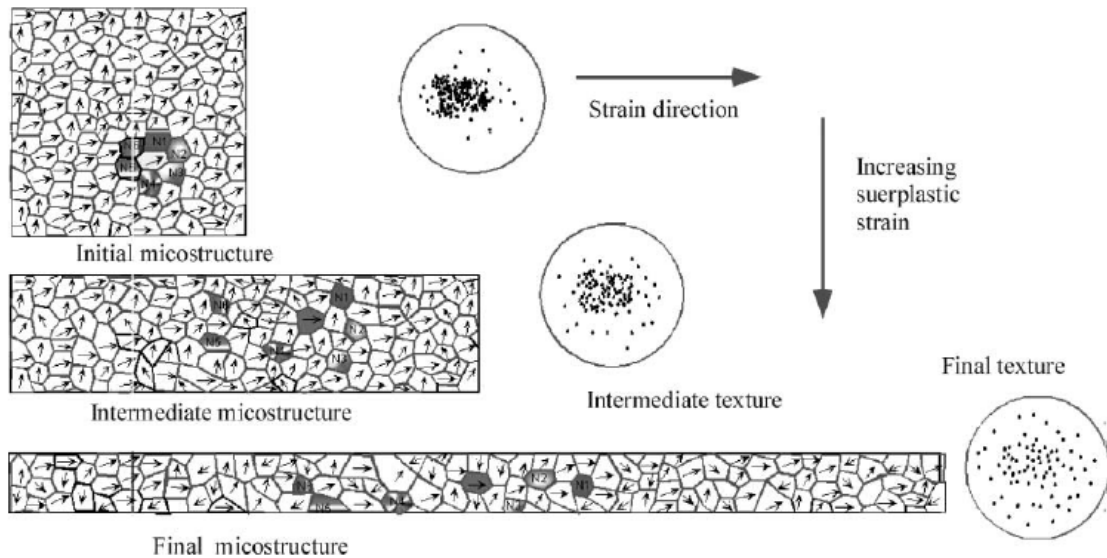


Figure 1.11: A schematic of microstructure and texture evolution during superplastic deformation (Chandra, 2002).

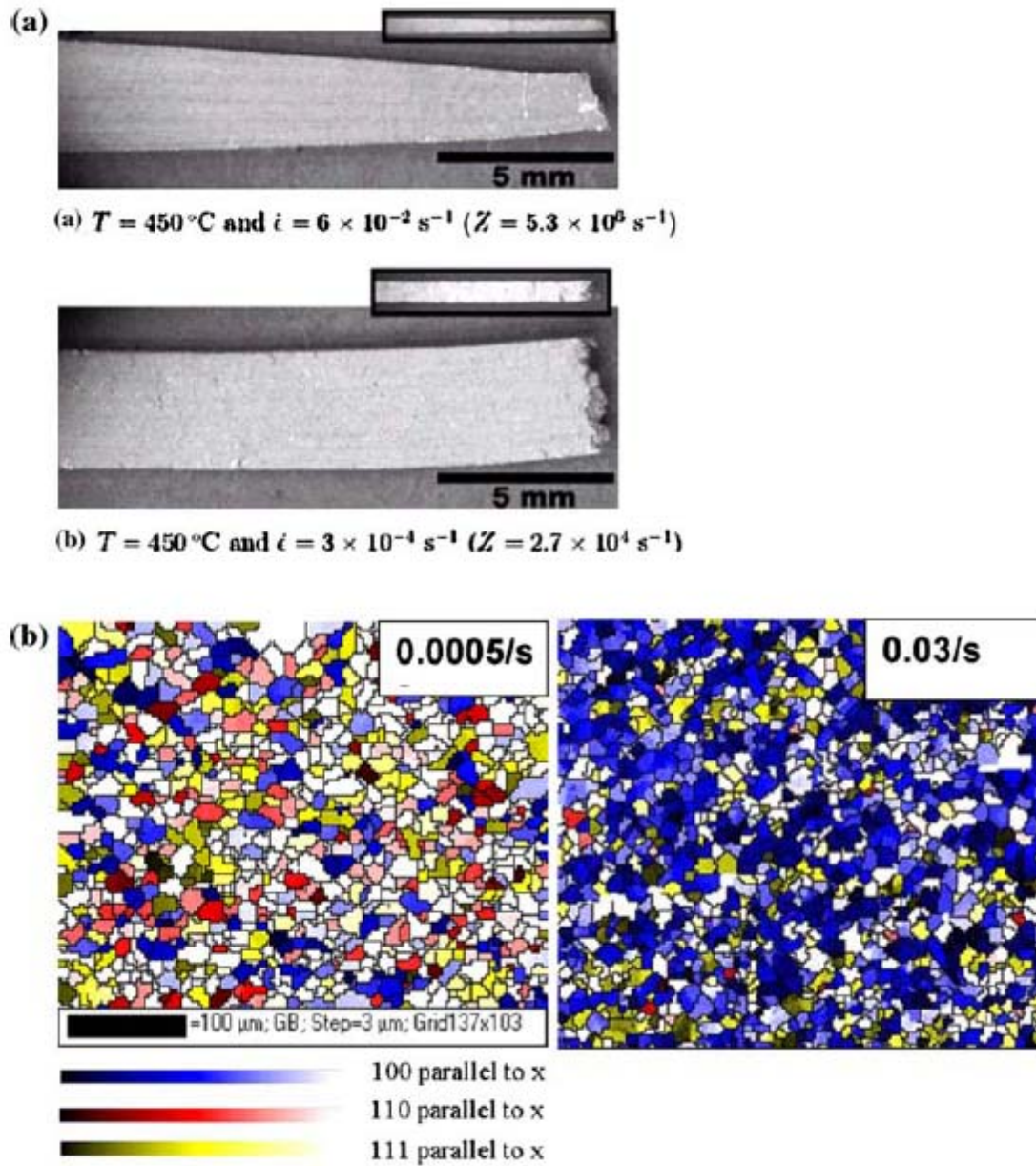


Figure 1.12: Mode of failure (a) and microstructure evolution (b) in a sample deformed in the dislocation creep regime (top sample in (a), right sample in (b)) and the grain boundary sliding regime (bottom sample in (a), left sample in (b)) (Agarwal, Briant, Krajewski, Bower, & Taleff, 2007).

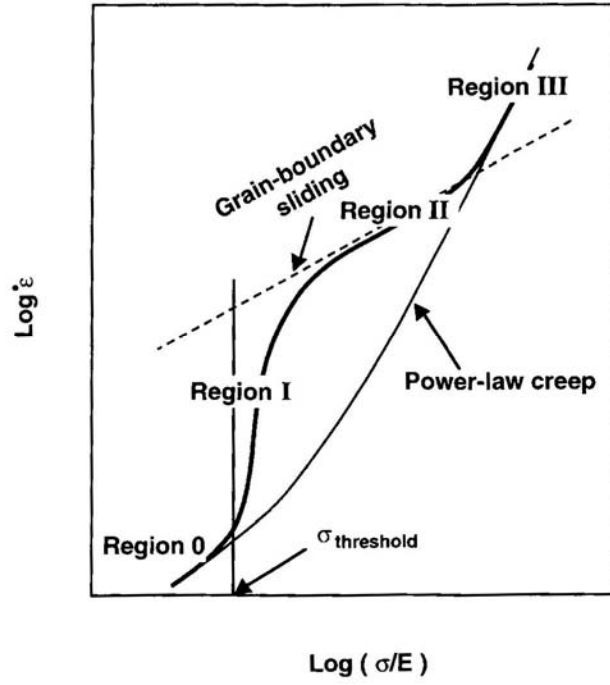


Figure 1.13: Creep behavior of fine grained materials (Nieh, 1997).

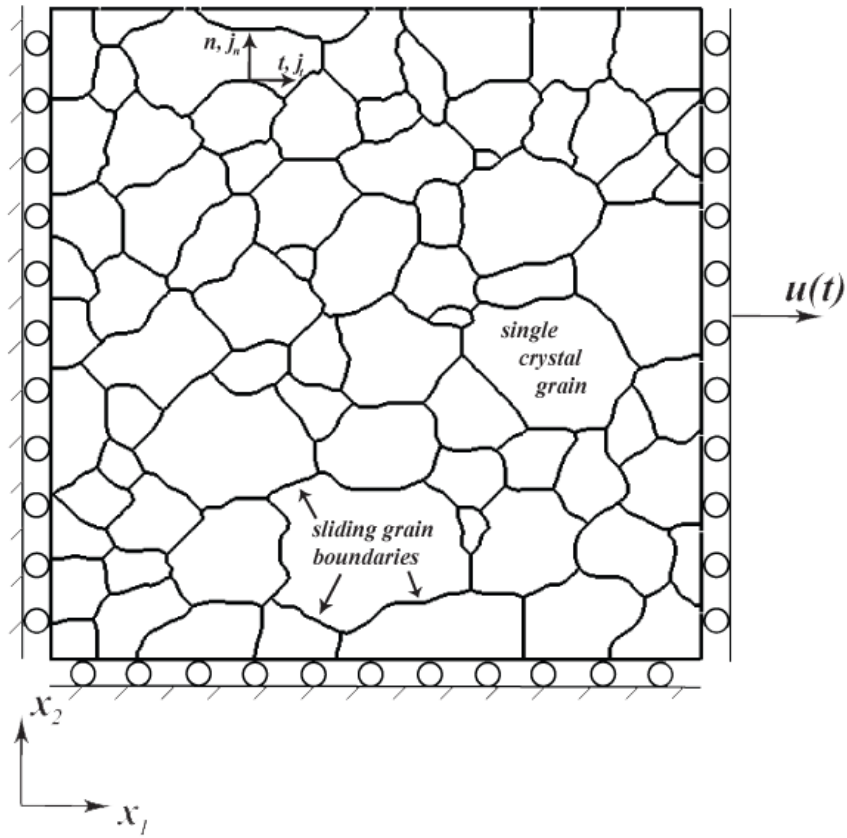


Figure 1.14: Schematic of the microstructure used in the finite element simulations.

## **CHAPTER 2: EXPERIMENTAL PROCEDURES AND RESULTS**

As a precursor to development of the finite element model, substantial experimental work was completed to form a base characterization of pure magnesium metal and magnesium alloy AZ31. Although pure magnesium will not likely be used for construction of automobile body panels, experimental tests were done to determine the characteristics of magnesium without solute strengthening or other effects due to alloy composition. It is useful to make comparisons between the experimental characterization of pure magnesium and magnesium alloys to understand elevated temperature behavior. Magnesium alloy AZ31 was chosen as the magnesium alloy for investigation in this work. It is commonly identified as a possible choice for adaption of the QPF process to magnesium, as evident by its use in the decklid of the Cadillac *STS* (Carter, Krajewski, & Verma, 2008). It is a good structural alloy with high specific strength, and there have been multiple reports of superplastic behavior in the sheet material (Hutchinson, Barnett, Ghaderi, Cizek, & Sabirov, 2009; Kim, S. W. Chung, C. S. Chung, & Kum, 2001; Lapovok, Estrin, Popov, Rundell, & Williams, 2008; Panicker, Chokshi, Mishra, Verma,



& Krajewski, 2009; del Valle, Pérez-Prado, & Ruano, 2005; Yi et al., 2006). It is also the most commonly available commercial magnesium alloy. In this case extruded AZ31 sheet has been investigated experimentally to improve understanding of elevated temperature deformation mechanisms. As will be explained, the extruded sheet exhibits different tensile behavior if it is strained so that the tensile axis is parallel or perpendicular to the extruded direction. From a microstructural viewpoint the most important differences affected by a change in the orientation of the tensile specimen are the apparent grain size and texture of the material. Experiments were performed to highlight these differences and to form a basis for further examination using the finite element model.

The choice of extruded magnesium AZ31 sheet as the second material for investigation was made due to its known anisotropic behavior in room temperature tensile tests, which has recently been studied at length. Krajewski et al. tested four different magnesium alloys in tension at room temperature and noted significant differences in the strength and ductility of extruded magnesium AZ31 and ZM21 sheet depending on if the tensile direction was rotated  $0^\circ$ ,  $45^\circ$ , or  $90^\circ$  to the extruded direction (Krajewski, Ben-Artzy, & Mishra, 2010). AZ61 and AM50 sheet material were also tested, however the results were not as drastic suggesting that composition plays a role in limiting or enhancing this effect. Specifically for the AZ31 samples, the yield stress was greatest when the tensile axis was parallel to the extruded direction and decreased for the other two orientations. When the tensile axis was rotated  $45^\circ$  from the extrusion axis the ductility was greatest, and less so for the samples cut so that the tensile axis was  $0^\circ$  and  $90^\circ$  to the extrusion axis. The rate of work hardening was also affected by the orientation of the tensile axis (Krajewski et al., 2010). Xiong and Davies show similar results in their

work with extruded AZ31 sheet tested in tension at room temperature (Xiong & C. H. J. Davies, 2003). However, more research is needed to determine if the anisotropic effects of extruded sheet at room temperature extend to elevated temperature deformation, where grain boundary sliding plays a larger role in deformation and the CRSS of the non-basal slip systems are decreased. Barnett et al. show that anisotropy is affected by an increase in temperature. Their work suggests that an increase in the fraction of strain due to GBS is responsible for the decrease in the Lankford r-value that occurs when temperature is increased for tensile tests of magnesium AZ31 sheet (Barnett, Ghaderi, Sabirov, & Hutchinson, 2009). In this dissertation, extruded magnesium AZ31 sheet was chosen to be investigated at temperature and strain rates typical of QPF with the intent of furthering the understanding of the deformation mechanisms in magnesium.

Multiple experimental procedures were performed on the pure magnesium sheet and magnesium alloy AZ31 extruded sheet including both static and dynamic tests. First, heat treatment experiments were performed to determine the microstructure evolution at elevated temperature. Next tensile tests were completed to determine the response of each material to an imposed strain rate at elevated temperature. These experiments were evaluated by performing microscopy on the strained specimens and by analyzing the stress generated in the samples. This chapter will discuss each procedure and the results that were obtained. First the procedures will be described; in general they are the same for each material. Next material specifics will be explained along with the results from each experiment.

## **2.1 Experimental Procedures**

### **2.1.1 Heat Treatment**

Heat treatment experiments were performed to determine the effect of temperature on the microstructure of the material by annealing material samples for various lengths of time at multiple temperatures. A Linberg/Blue furnace was utilized with Fluke 52 external thermocouples. Total time was measured from the time the sample entered the furnace to when it was removed. The furnace was preheated prior to beginning the test so that testing temperature was reached within one minute of inserting the sample into the furnace. Upon removal from the furnace, the samples were allowed to air cool at room temperature. The effect of annealing on microstructure was determined from grain size measurements taken before and after testing. Grain size was measured using the linear intercept method in accordance with ASTM standard E112-96

### **2.1.2 Tensile Tests**

Elevated temperature tensile tests were performed to determine the response of the material to an applied strain rate at temperature. A standard dog bone style elevated temperature tensile specimen was used for all tests. The specimen dimensions are shown in figure 2.1. Each experiment was performed on an Instron 5568. The tensile specimens were loaded into a pre-heated furnace, and testing was begun 2.5 minutes after the specimen reached testing temperature to ensure even temperature distribution in the

specimen. At the completion of the test, which was determined by fracture in all cases, the specimen was immediately removed and quenched in water to preserve the microstructure. Two different types of tensile tests were performed on the specimens, a constant strain rate test and a step strain rate test. During the constant strain rate test the specimen was strained at a constant rate until failure while load and extension were recorded to determine true stress and true strain during the test.

Step strain rate tests were performed to obtain the steady state flow stress as a function of strain, strain rate, and temperature. In these tests, the specimen was first subjected to an initial strain rate of  $3.0 \times 10^{-3} s^{-1}$  to guarantee that the specimen was firmly positioned in the testing apparatus and to stabilize the microstructure. Then the specimen was subjected to multiple strain rates sequentially in decreasing order from  $3.0 \times 10^{-2} s^{-1}$  to  $1.0 \times 10^{-4} s^{-1}$ ; each strain rate was held constant for a minimum of 2 percent engineering strain. When the stress had ceased to decay after each change in strain rate, reaching essentially a steady state value, the stress was recorded in the specimen. Each specimen was subjected to multiple cycles so that the flow stress at multiple strains could be interpolated. An example stress vs. strain curve that shows two complete cycles of a step strain rate test is shown in figure 2.2. The horizontal lines show how the stress was interpolated to give the steady state flow stress at various strain rates. It is assumed that the microstructure remains relatively constant during testing at each strain rate and that minimal hardening or softening occurs in the sample during the test. This assumption is reinforced by observing that the horizontal lines used to interpolate the flow stress in each test had close to no slope; the stress recorded at low and high levels of strain was approximately equal. However, as can be seen in figure 2.2, there is a

change in the stress during the period at each strain rate, thus the range of error possible from the tests was recorded and error bars were placed on the plots compiled from the step strain rate test results.

The data from these tests were used to determine plots of strain rate as a function of stress, which could then be fit to the following equation

$$\dot{\epsilon} = A\sigma^n \quad (2.1)$$

where  $A$  is a constant and  $n$  is the stress exponent. Thus, the stress exponent could be extrapolated from the results. The data can also be plotted in terms of the strain rate sensitivity  $m$ , which is defined as

$$m = \frac{d(\log(\sigma))}{d(\log(\dot{\epsilon}))} \quad (2.2)$$

and is equal to the inverse of the stress exponent,  $n$ . A change in the stress exponent (and in the strain rate sensitivity) is often used to gain insight on the prominent deformation mechanisms in the microstructure.

Calculating the activation energy can also be useful to determine the prevalent deformation mechanisms in the material. If the strain rate is defined in the following manner

$$\dot{\epsilon} = A_1 \exp\left(\frac{-Q}{RT}\right) \quad (2.3)$$

where  $Q$  is the activation energy for diffusion,  $R$  is the universal gas constant,  $T$  is temperature, and  $A_1$  is a constant. Equation 2.3 can then be modified to read

$$\ln(\dot{\epsilon}) = \frac{-Q}{R} \cdot \frac{1}{T} + A_2 \quad (2.4)$$

where  $A_2$  is a constant. If the logarithm of strain rate is plotted against the inverse of

temperature, the activation energy can be extrapolated from the slope of each curve for a constant flow stress.

### **2.1.3 Sample Preparation and Observation**

As received material, annealed samples, and deformed samples were each prepared for microstructure analysis using optical microscopy to determine grain size and general topography, and the method of electron backscatter diffraction (EBSD) on the scanning electron microscope (SEM) to determine texture and grain orientation. The samples were prepared in careful adherence to the following procedure for observing the microstructure characteristics. Each specimen was first cut to a more optimal size or to expose a specific face using a low speed diamond saw to eliminate any chance of twinning during the cutting process. The specimens were then mounted in cold mounts (epoxy) so that there was no possibility of a change in the microstructure due to the heat and pressure associated with a hot mount. Conductive filler was used at the specified ratio for each mount that housed specimens destined to be analyzed using EBSD to ensure electrical conductivity. The samples were mechanically polished with fine grain SiC paper, followed by finer polishing using suspended alumina solution with particle size  $1\mu\text{m}$ ,  $0.3\mu\text{m}$ , and  $0.05\mu\text{m}$  in order of decreasing particle size. Specimens to be observed optically were etched using a Picric acid solution with the following formulation:

Acetic-Picric Etchant  
4.2 g Picric Acid  
10 mL Acetic Acid  
70 mL Ethanol

10 mL Distilled Water

Grain size was measured on the optically observed samples using the linear intercept method in accordance with ASTM standard E112-96. Samples to be observed using EBSD were electro-polished in a solution of 10 percent nitric acid in methanol at 2 volts for one second with an aluminum cathode and a copper anode. All EBSD imaging was done on a JEOL 845 scanning electron microscope, and all EBSD patterns were obtained using an Oxford Instruments HKL Nordlys detector and the Oxford Instruments INCA software package.

## **2.2 Experimental Results**

### **2.2.1 Material Specifications**

All experiments were completed primarily with one of two materials to be described here. The first was 99.999% pure magnesium ingot. For sheet testing the ingot was cut into 0.5 inch slabs and then warm rolled to a final thickness of 1.6mm at an entry temperature of 400°C with an average reduction per pass of 10%. A micrograph of the as received material is shown in figure 2.3. There is substantial work in the material due to the rolling process, which also produced pockets of large and small grains. Thus, there is a significant amount of stored energy in the as received material that could serve to promote recrystallization and grain growth during an annealing process.

The second material used in experiments was magnesium alloy AZ31 with

composition Mg – Al 3.5 – Zn 1.5 – Mn 0.2 – Cu 0.05 – Ca 0.04 – Fe 0.01 – Ni 0.01 (in weight percent) extruded into sheet material. Elevated temperature tensile test specimens were cut from the extruded sheet so that the tensile axis was rotated  $0^\circ$  or  $90^\circ$  from the extruded direction (ED). The specimens cut  $0^\circ$  to the extruded direction (ED) were cut from sheet with a final thickness of 1.30mm, and the specimens cut  $90^\circ$  to the ED were cut from sheet with a final thickness of 1.67mm. Optical microscopy and EBSD were used to characterize the initial microstructure, during which the anisotropic nature of the material was discovered. The grain size measured on the transverse face of the specimens loaded  $0^\circ$  to the ED was approximately  $18\mu\text{m}$  where as on the specimens loaded  $90^\circ$  to the ED the initial grain size was measured as approximately  $9\mu\text{m}$  (figure 2.4 describes with more clarity the exact face that was observed). This suggests that during the extrusion process the grains were elongated in the extrusion direction. Figure 2.5 shows optical micrographs the specimens oriented  $0^\circ$  and  $90^\circ$  to the ED where this effect can be observed. A disparity also exists between the textures of the two orientations as recorded using EBSD. Pole figures and an EBSD texture map for the specimen oriented  $0^\circ$  to the ED is shown in figure 2.6, and similarly for the specimen oriented  $90^\circ$  to the ED in figure 2.7. As observed in figure 2.6, the grains are mostly oriented with the basal plane normal to the surface for the specimen oriented  $0^\circ$  to the ED, whereas the grains of the specimen oriented  $90^\circ$  to the ED are mostly oriented in the  $\langle 10\bar{1}0 \rangle$  and  $\langle 11\bar{2}0 \rangle$  directions (figure 2.7). This suggests that the extrusion process tends to elongate and rotate the grains so that the basal plane is aligned along the extrusion direction. Thus, when the specimen is loaded  $0^\circ$  or  $90^\circ$  to the ED with respect to the tensile axis, the apparent grain size and the orientation of the grains will change.



## 2.2.2 Heat Treatment Effects

From the beginning, understanding elevated temperature forming of magnesium and its alloys was the principle objective. Thus, a natural place to start to characterize the material was to perform annealing experiments. Two sets of experiments were performed on the pure magnesium material. In the first test, test specimens were held at various temperatures, 350°C, 400°C and 450°C for a constant period of time, 30 minutes. In the second test, test specimens were held for various time periods, 15, 30, 45, and 60 minutes, at a constant temperature. 450°C was chosen because it is the temperature for the QPF process in aluminum alloy 5083. Micrographs of the material after the completion of each of these tests can be seen in figure 2.8 and 2.9. There is very little grain growth at 350°C, where the final grain size is 33 $\mu$ m. However, with an increase in temperature to 400° and then 450°C there was a substantial increase in grain size to 90 $\mu$ m and 150 $\mu$ m, respectively. When the grain growth at 450°C is inspected with respect to time there does not seem to be a strong effect. Substantial grain growth occurs within 15 minutes at temperature and does not increase or decrease substantially with increased time in the furnace.

Specific annealing tests were not performed on the magnesium alloy AZ31 material. However, the gauge section of the tensile samples was observed after all tensile tests, some of which took approximately 30 minutes to complete. In all cases there was no appreciable increase in grain size in the gauge section. Thus, it was concluded that although grain growth due to temperature is substantial in pure magnesium there is little effect in AZ31.

## 2.2.3 Elevated Temperature Tensile Tests

### 2.2.3.1 Pure Magnesium

Constant strain rate to failure tests were performed on the pure magnesium tensile specimens at two different strain rates ( $1.0 \times 10^{-1} \text{s}^{-1}$  and  $1.0 \times 10^{-3} \text{s}^{-1}$ ) and at two different temperatures ( $350^\circ\text{C}$  and  $450^\circ\text{C}$ ). The true stress vs. true strain curves for these tests can be observed in figure 2.10. As would be expected when comparing temperature, testing at lower temperature leads to a greater flow stress in the specimen, and when comparing strain rate, testing at a faster strain rate leads to greater flow stress. There is little hardening or softening during each of the tests; the stress remains fairly constant from after the yield stress is reached until failure. It is interesting to note that even with an increase in the strain rate of two orders of magnitude and an increase in testing temperature of one hundred degrees there is very little change in the ductility. Ductility in pure magnesium is fairly independent of strain rate and temperature in this range.

As was mentioned above, immediately after the test was completed, the samples were removed from the furnace and quenched in water to preserve the final microstructure. Each specimen that was tested at a constant strain rate to failure was examined by optical microscopy. Micrographs from multiple positions along the gauge length of the tested sample, which correspond to increasing amounts of strain, are shown in figure 2.11 for the specimen pulled at a strain rate of  $1.0 \times 10^{-3} \text{s}^{-1}$  at  $450^\circ\text{C}$ , and in figure 2.12 for the specimen pulled at the same strain rate but at a temperature of  $350^\circ\text{C}$ . In both cases there is a substantial increase in grain size when strain is induced in the

sample, but grain size does not increase with increasing strain. The grain size of the specimen tested at 450°C grew to about three to four times as large as the grain size measured after the annealing tests at 450°C, from approximately 150 $\mu$ m to 550 $\mu$ m. The grain size of the specimen strained at 350°C expanded to grain sizes about twice as large as during the annealing tests. However, as is shown in figure 2.13, grain size is not a function of strain. Grain size increases due to the imposed strain rate to an approximate threshold which varies with temperature and then remains at that grain size until failure.

The stress vs. strain rate curves that were obtained from the step strain rate tests on pure magnesium are shown in figure 2.14 for three different temperatures. In each case the specimen was annealed at 450°C for fifteen minutes and allowed to air cool before the test was begun so that each specimen had an equal starting microstructure. If each curve is fit to equation 2.1, the stress exponent for each curve is shown to be approximately five, suggesting that dislocation creep was the dominant mechanism of deformation in the sample. This is reinforced by the large grain size in the gauge section of the specimens which also suggests that dislocation creep would be dominant. Grain boundary sliding is known to be less prevalent at such large grain sizes. The step strain rate test performed at 350°C was repeated with a specimen that had been annealed at 350°C for fifteen minutes rather than 450°C, which will give a smaller starting grain size in the specimen, on the order of 33 $\mu$ m for the test at 350°C and 117 $\mu$ m for the test at 450°C. As seen in figure 2.15, there is no difference in the stress vs. strain rate curve due to this change, suggesting that the results of this test, including the stress exponent, are independent of starting grain size in this range.

It is useful to consider the activation energy for creep in pure magnesium to

understand the deformation; however, in this case the results are inconclusive. The activation energy was determined by interpolating the results of the step strain rate tests, and calculated to be approximately 160 kJ/mol. Frost and Ashby list the activation energy for creep in pure magnesium with a grain size of 0.1mm to be 134 kJ/mol for temperatures from 325°C to 500°C, which is very close to the value self diffusion of magnesium, 135 kJ/mol. They state that above 500°C ( $\sim 0.78 T_M$ ) the activation energy increases to 230 kJ/mol (Frost & Ashby, 1982). The value obtained in this work is greater than that listed by Frost and Ashby for the range of temperatures where the tests were completed. This could be a result of the large grain sizes that develop in the specimens which grow to six times greater than the value listed by Frost and Ashby.

### **2.2.3.2 Magnesium Alloy AZ31**

A similar analysis was completed for the extruded magnesium alloy AZ31 sheet as was done for the pure magnesium material. Constant strain rate to failure tests were performed at two different strain rates at 450°C for tensile specimens loaded parallel and perpendicular to the extrusion direction, the results of which are seen in figure 2.16. As before, a greater flow stress was reached in the material when the specimen was pulled at a faster strain rate. However, in the case of the alloy material there was a dependence of ductility on strain rate; the material exhibited more ductility at the lower strain rate. Due to alloy strengthening, the strength of the alloy is more than double that of the pure magnesium material as would be expected. At the strain rate of  $0.001\text{s}^{-1}$ , the specimen loaded  $0^\circ$  to the ED increases to a peak at the yield stress followed by softening. Whereas

the specimen loaded  $90^\circ$  to the ED rises to a slightly lower yield stress, which is followed by a period of hardening and then softening. At the faster strain rate there is less of a dramatic peak to the curve for the specimen loaded  $0^\circ$  to the ED, but it still shows only softening to failure. The curve for the specimen loaded  $90^\circ$  to the ED is similar to the  $0^\circ$  to the ED curve, but the softening is not as fast. In both cases, the specimen is loaded  $90^\circ$  to the ED the material exhibits greater ductility than the specimens loaded  $0^\circ$  to the ED.

The orientation of the tensile axis with respect to the extruded direction also had an effect on the necking and eventual fracture of the specimens. As seen in figure 2.17, for the specimens where the tensile axis was oriented parallel to the extruded direction thinning of the specimen during testing occurred primarily in the thickness direction, where as for the specimens oriented with the tensile axis perpendicular to the extruded direction thinning occurred primarily in the width direction.

Step strain rate tests were performed to show the effect of strain rate on flow stress. Strain rate as a function of flow stress is plotted for each orientation in figure 2.18. In figure 2.19 the strain rate sensitivity is plotted as a function of strain rate. The strain rate sensitivity for both orientations is equal to approximately 0.2 for high strain rates. When the strain rate is decreased the strain rate sensitivity for specimen loaded  $90^\circ$  to the ED increases above 0.5, where as for the specimen loaded  $0^\circ$  to the ED it increases to approximately 0.3. The dynamic nature of the strain rate sensitivity suggests a change in the deformation mechanism from fast to slow strain rates. As suggested previously, strain rate sensitivity on the order of 0.5 is characteristic of grain boundary sliding as the dominant deformation mechanism, where as for a lower strain rate sensitivity, on the order of 0.2, it is likely that dislocation creep is dominant. The strain rate sensitivity for

the specimen loaded perpendicular to the ED is greater at low strain rates, which suggests that anisotropy affects the strain rate sensitivity. This effect can also be observed in figure 2.18, where the shapes of the curves diverge to a larger extent at the slower strain rate.

The effect of temperature on the magnesium AZ31 extruded sheet was evaluated by performing SSR tests at 350°C to compare to the results described earlier for 450°C. As shown in figure 2.20, for a decrease in testing temperature there is an increase in flow stress across the range of strain rates tested. The stress exponent remains at approximately 5 at fast strain rates, but only transitions to approximately 4 for the specimen oriented with the tensile axis 0° to the ED and approximately 3 for the specimen oriented with the tensile axis 90° to the ED at slow strain rates. Thus, there is likely a greater contribution from dislocation creep during deformation at lower temperature.

The activation energy can be calculated as described above for each orientation of the tensile axis with respect to the extruded direction. Figure 2.21 shows the variation of activation energy as a function of stress. At low stress the activation energy is approximately 118 kJ/mol, but at higher values of flow stress the activation energy increases to a range of ~125 kJ/mol to ~145 kJ/mol. This is in the range of lattice diffusion in magnesium which is listed at 135 kJ/mol by Frost and Ashby (Frost & Ashby, 1982), and approaches the activation energy for aluminum diffusion in magnesium, 143 kJ/mol (Vagarali & Langdon, 1981). The lower value of 118 kJ/mol is greater than the activation energy of boundary diffusion and core diffusion in magnesium, both listed at 92 kJ/mol, but lower than that of lattice diffusion (Frost & Ashby, 1982). From the results shown in figure 2.21, it is evident that there is a change in the deformation mechanism for

both sample orientations as the stress in the sample is increased, which based on the strain rate vs. stress results is comparable to an increase in strain rate. This supports the results presented above of a transition in the dominant deformation mechanism from slow to fast strain rates, and furthermore that the transition occurs at a different strain rate for the two orientations.

### **2.3 Experimental Conclusions**

At this point it is a good idea to stop and take stock of what has been discovered thus far about deformation of magnesium at elevated temperatures. The pure magnesium specimens showed large grain growth during annealing and even larger grain growth when strain energy was induced in the specimens. However, in both cases a grain size threshold was reached, thus grain growth in pure magnesium is a function of temperature and strain rate, but is not a function of time or strain. Although the material showed extensive grain growth, grain size was not shown to have an effect on the flow stress as a function of strain rate. Ductility was shown to be independent of temperature and strain rate, but yield strength was dependent on both variables. The strain rate sensitivity remained constant at approximately 0.2 across all strain rates tested, and similarly the activation energy remained constant at approximately 160 kJ/mol. This suggests that dislocation creep is the dominant mechanism for deformation for strain rates from  $3.0 \times 10^{-2} s^{-1}$  to  $1.0 \times 10^{-4} s^{-1}$  at temperatures from 350°C to 450°C.

The alloy material showed a much more dynamic response to an imposed strain rate in general, and much more so when the orientation of the tensile axis is considered.

For magnesium alloy AZ31 ductility and yield strength were both shown to be dependent on temperature and strain rate. There was little grain growth with temperature. The strain rate sensitivity increased from 0.2 at high strain rates to 0.3 when the tensile axis was oriented parallel to the extrusion direction and 0.5 when the tensile axis was perpendicular to the extrusion direction at low strain rates. This suggests a change in the dominant deformation mechanism from dislocation creep at high strain rates to grain boundary sliding at low strain rates. A change in the dominant deformation mechanism is also suggested by the dynamic nature of the activation energy.

The extruded sheet shows dependence on the orientation of the tensile axis with respect to the extruded direction. When the tensile axis and the extrusion direction are parallel to each other the specimen exhibits greater yield strength and decreased ductility compared to when the tensile axis is rotated 90 degrees. Necking occurs primarily on opposite faces for the two specimens. The strain rate sensitivity ranges from approximately 0.2 at high strain rates for both orientations to approximately 0.3 when the tensile axis and extrusion direction are parallel, and approximately 0.5 when they are perpendicular. Thus, due to the results of the tensile tests there are multiple differences in the response of the differently oriented specimens to an induced strain rate. It is assumed that the origin of these discrepancies lies in the extrusion process which elongates the grains and aligns the basal plane parallel to the extrusion direction. The apparent grain size of the microstructure for the specimen with the tensile axis aligned  $0^\circ$  to the extruded direction is  $18\mu\text{m}$  and the grains on this face are strongly oriented in the basal direction, whereas for the specimen with the tensile axis aligned  $90^\circ$  to the extruded direction the apparent grain size is  $9\mu\text{m}$  and the grains are oriented in the directions perpendicular the

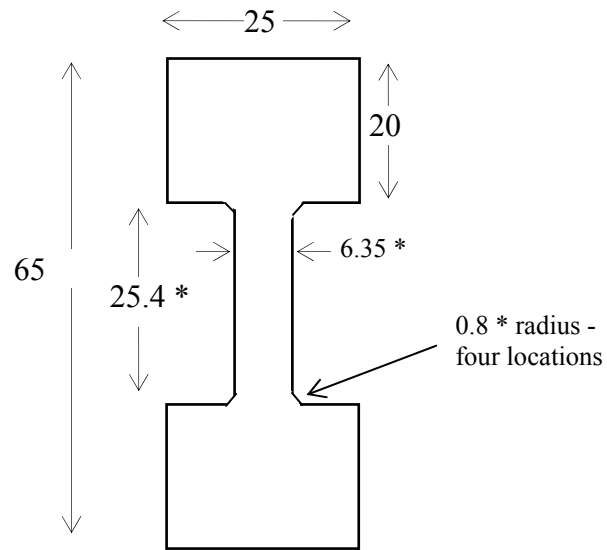


basal direction along this face. In conclusion, the orientation of the tensile axis to the extruded direction generates significant changes in the deformation response to a tensile strain rate, including strength, ductility, strain rate sensitivity, and fracture geometry. From a microstructural viewpoint there are two distinct differences between the two orientations, the apparent grain size and the orientation of the grains with respect to the tensile axis.

Thus, in light of the conclusions drawn from this experimental work, the need for a microstructure based model for high temperature deformation in magnesium due to an imposed tensile strain rate is apparent to help decipher the experimental conclusions. A continuum finite element model was developed to predict the response of magnesium alloy AZ31. The microstructure based model, originally developed for fcc materials, has been modified to model the elevated temperature deformation mechanisms which occur in magnesium, an hcp material. The model idealizes a polycrystal as a set of single crystal grains separated by grain boundaries. It accounts for the following deformation mechanisms, dislocation creep within the grains including the effects of anisotropy, as well as grain boundary sliding and grain boundary diffusion. The model predicts the detailed distribution of stress and strain within the microstructure, as well as the macroscopic flow stress as a function of strain rate and grain size. The predictions of the model are shown to be in excellent agreement with experimental measurements of elevated flow behavior in magnesium alloy AZ31 for multiple grain sized material. Following this validation that utilized literature data, the model is applied to the results explained above and used to further the understanding of the anisotropic behavior of extruded magnesium alloy AZ31 sheet.

In the following chapter, the finite element model is explained in detail.

### SPF Tensile Test Specimen



All dimensions are in millimeters.

\* Critical dimensions: Tolerance:  $\pm 0.1$  mm

Figure 2.1: Schematic of an elevated temperature test specimen.

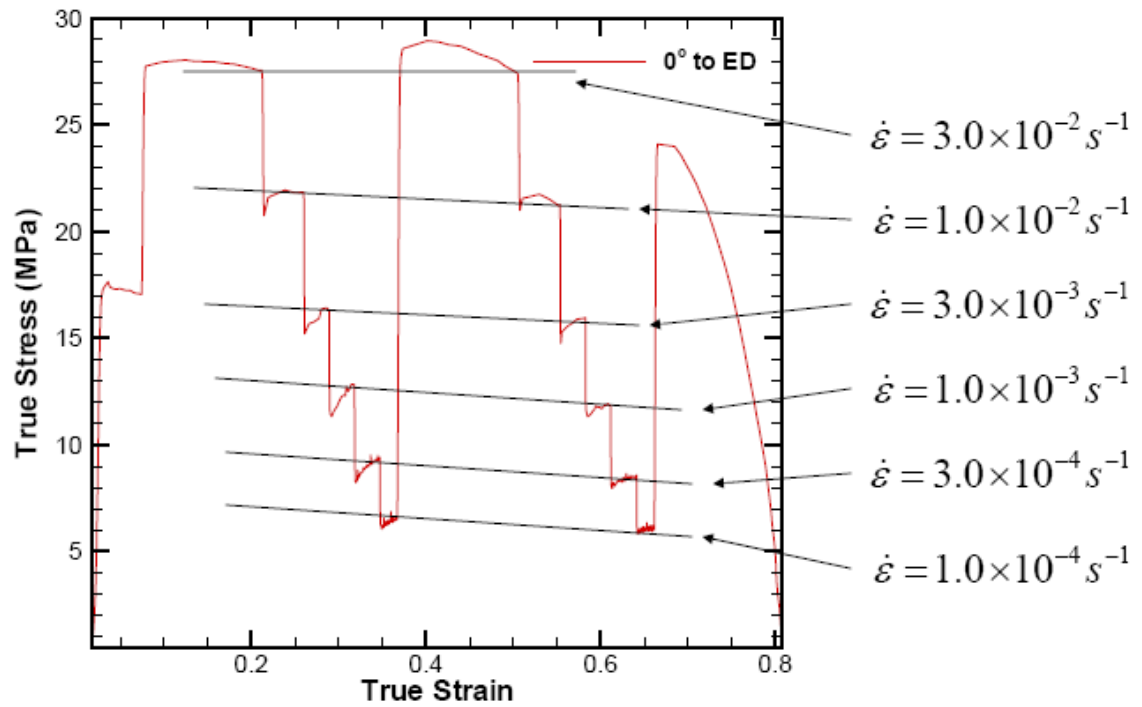


Figure 2.2: The true stress vs. true strain curve for two cycles of a step strain rate test. The flow stress at a given strain for a specific strain rate is interpolated from the linear fits to the steady state stress at each strain rate.

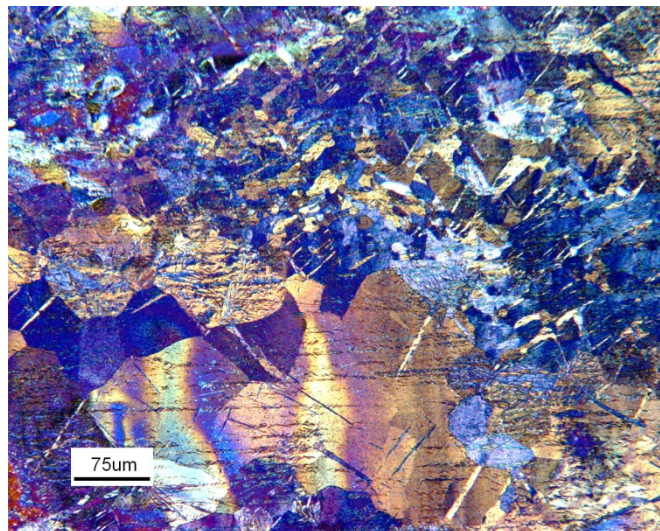
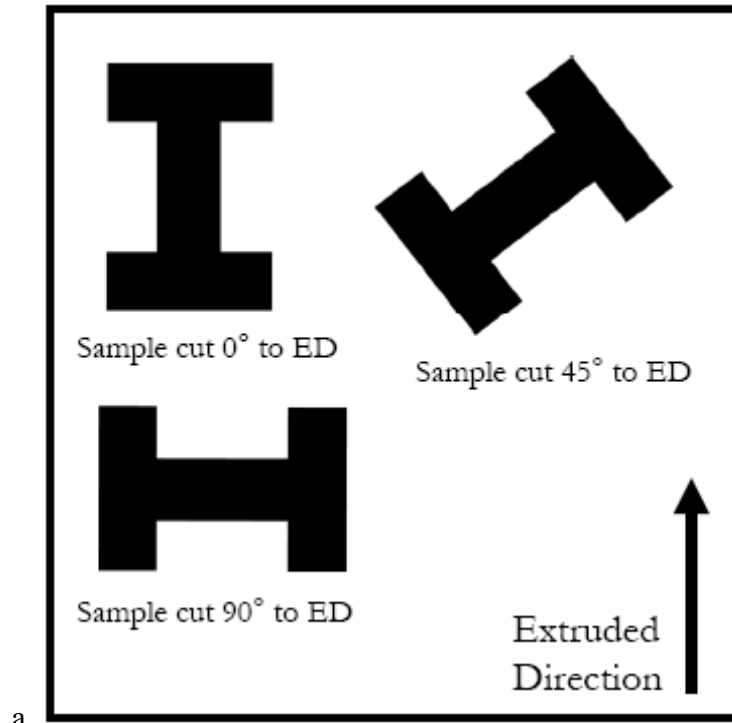
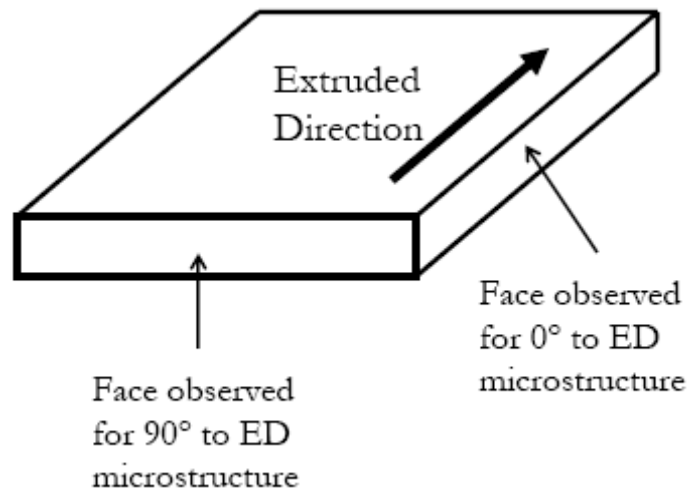


Figure 2.3: Micrograph of as received 99.999% pure magnesium sheet warm rolled to a final thickness of 1.6mm.



a



b

Figure 2.4: Schematic of the extruded sheet, detailing the orientation of tensile specimens and the face observed during microscopy measurements.

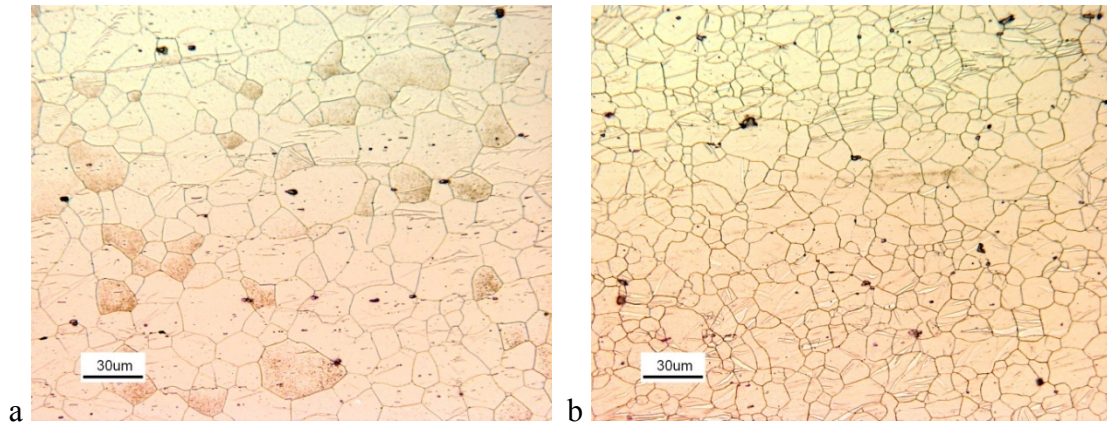


Figure 2.5: Optical micrographs of the specimen oriented  $0^\circ$  to the ED (a) and  $90^\circ$  to the ED (b).

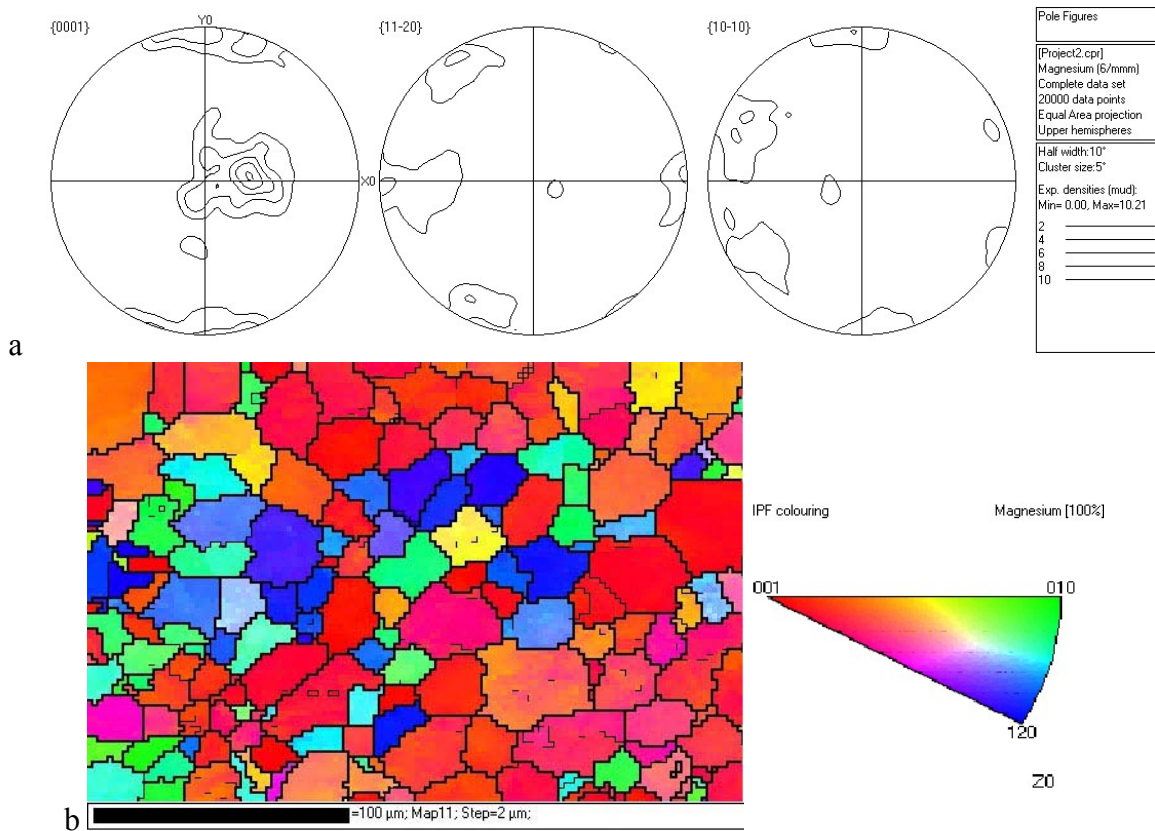


Figure 2.6: Pole figures (a) and texture map (b) for the specimen oriented with the tensile axis parallel to the extruded direction.

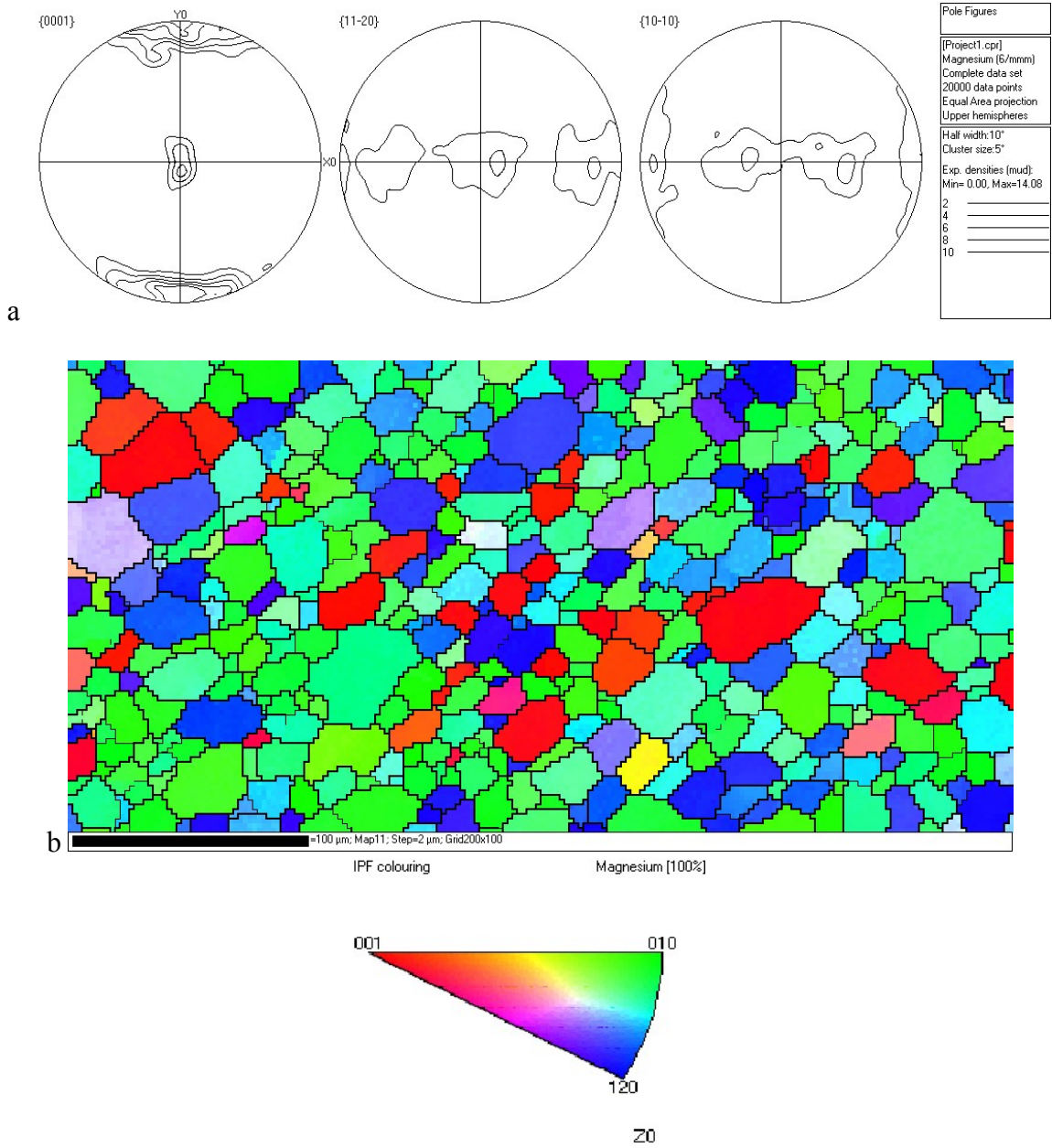
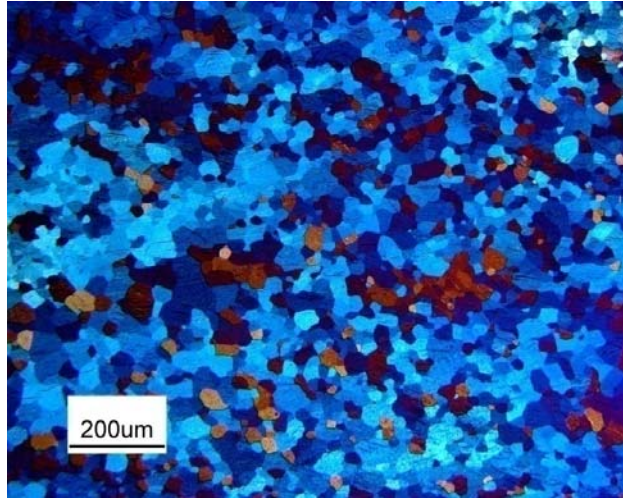
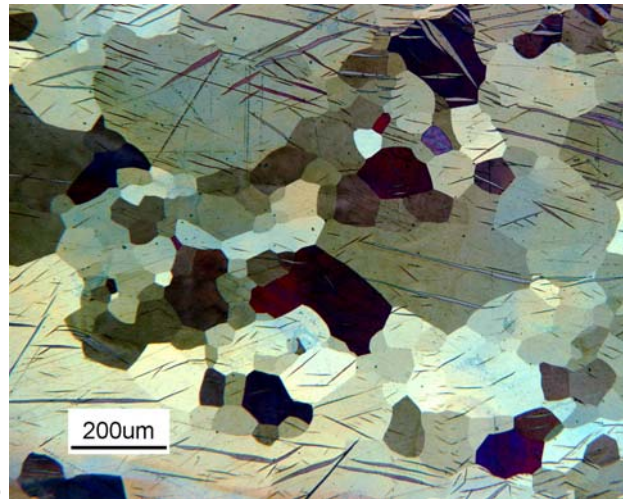


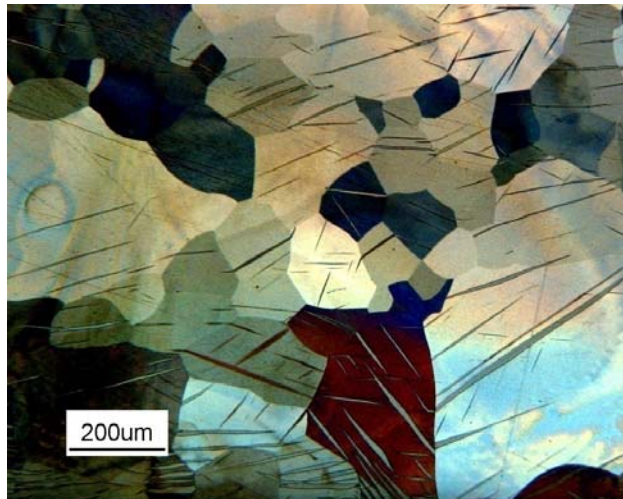
Figure 2.7: Pole figures (a) and texture map (b) for the specimen oriented with the tensile axis perpendicular to the extruded direction.



a



b



c

Figure 2.8: Micrographs of pure magnesium sheet annealed for 30 minutes at (a) 350°C, (b) 400°C, (c) 450°C. The average grain size is 33 $\mu\text{m}$  at 350°C, 90 $\mu\text{m}$  at 400°C, and 150 $\mu\text{m}$  at 450°C. The surface twins are due to polishing of the soft metal.



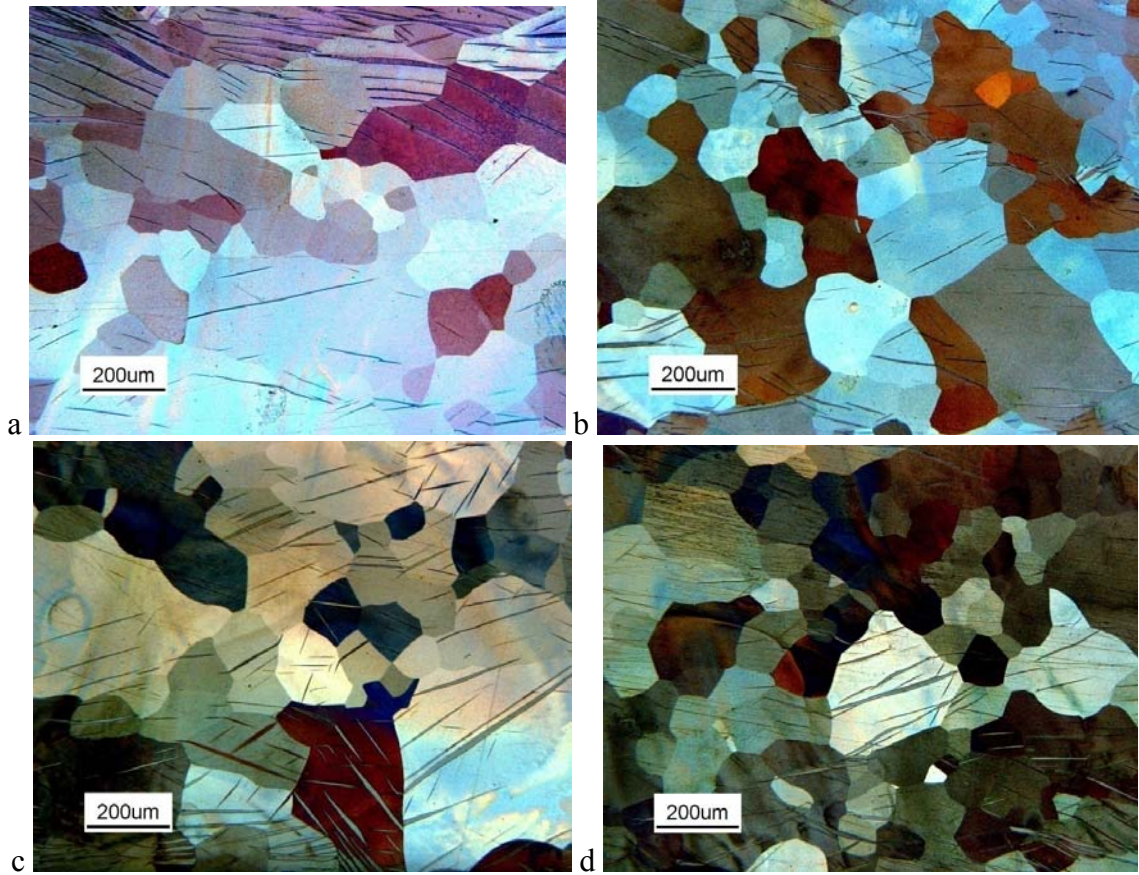


Figure 2.9: Micrographs of pure magnesium sheet annealed at 450°C for (a) 6 minutes, (b) 15 minutes, (c) 30 minutes, (d) 60 minutes. The average grain size is 141 $\mu\text{m}$  at 6 minutes, 117 $\mu\text{m}$  at 15 minutes, 150 $\mu\text{m}$  at 30 minutes, and 127 $\mu\text{m}$  at 60 minutes. The surface twins are due to polishing of the soft metal.

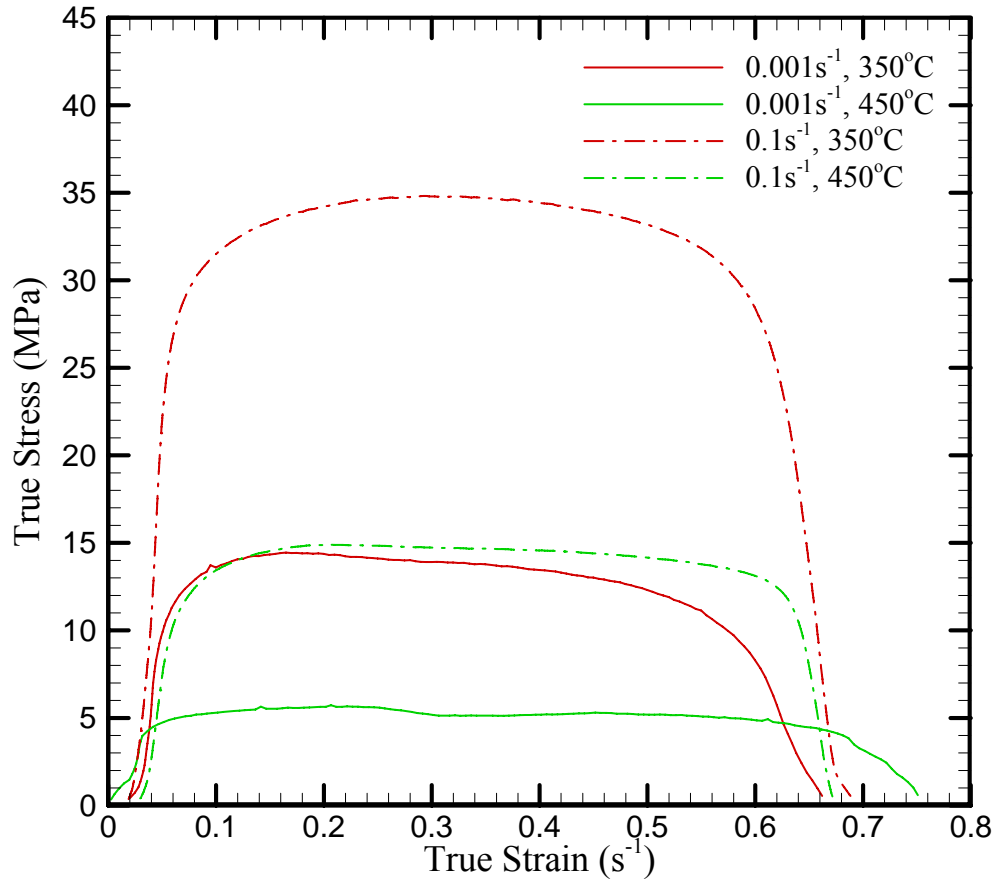


Figure 2.10: Stress vs. strain curves for pure magnesium specimens tested at 350°C and 450°C at a constant strain rate to failure of 0.1s<sup>-1</sup> and 0.001s<sup>-1</sup>.

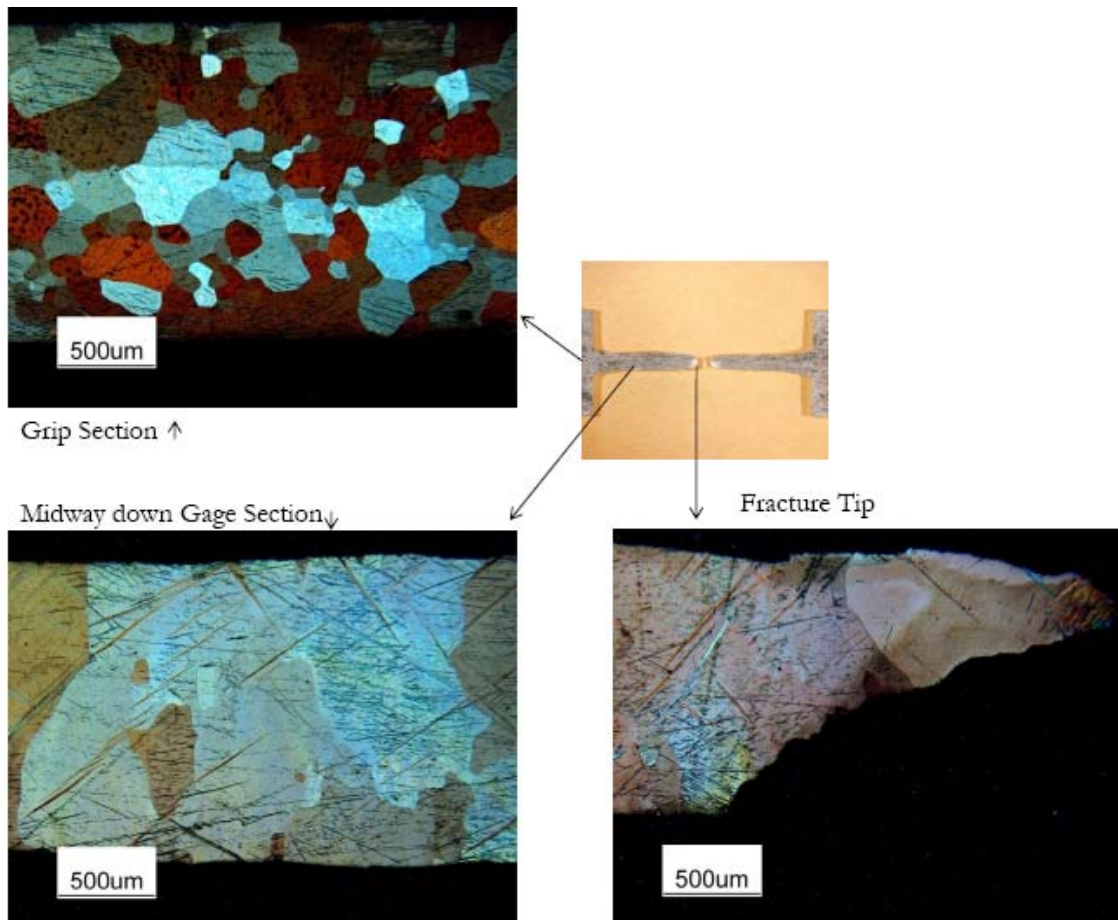


Figure 2.11: Micrographs from various points along a tensile specimen of pure magnesium pulled at a constant strain rate to failure of  $0.001\text{s}^{-1}$  at a constant temperature of  $450^\circ\text{C}$ . Each micrograph exhibits the result of increasing amounts of strain from the top left counter clockwise to the bottom right.

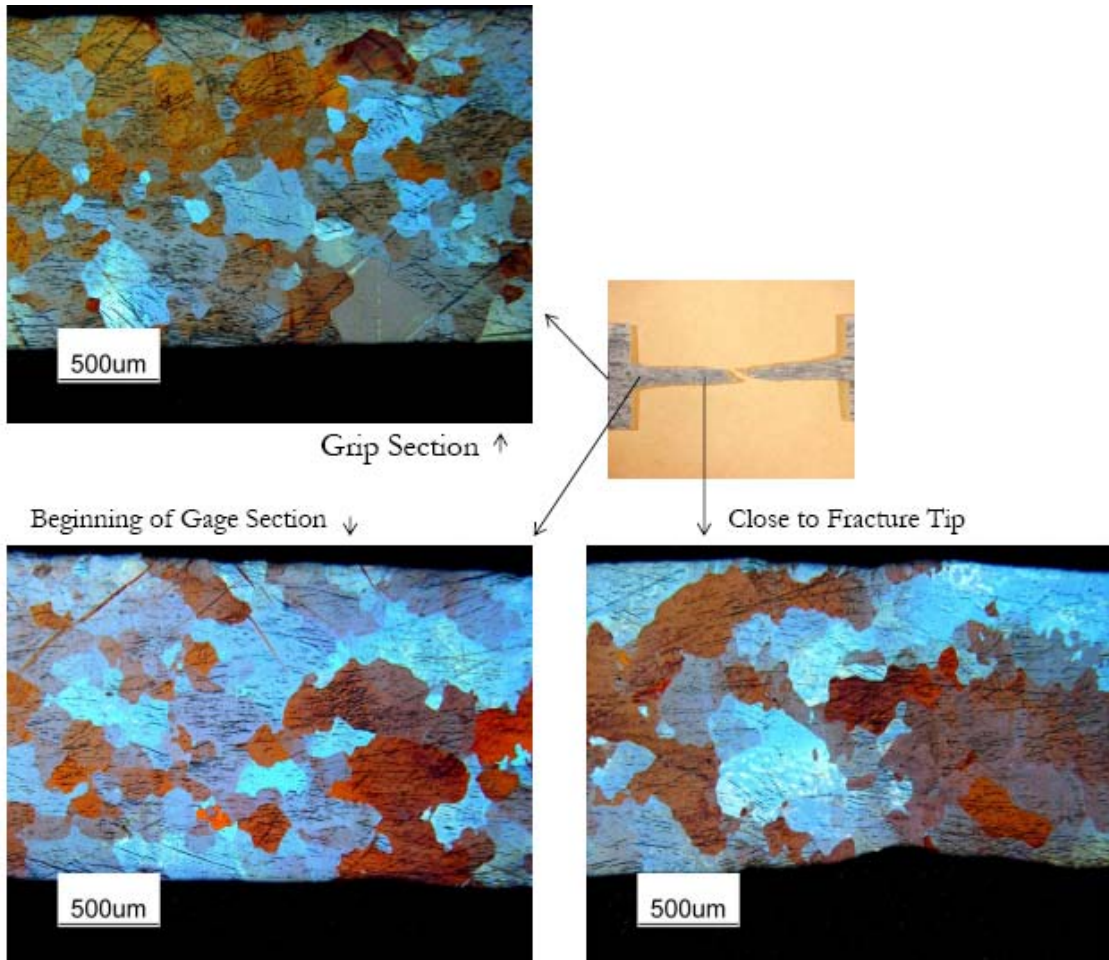


Figure 2.12: Micrographs from various points along a tensile specimen of pure magnesium pulled at a constant strain rate to failure of  $0.001\text{s}^{-1}$ , at a constant temperature of  $350^\circ\text{C}$ . Each micrograph exhibits the result of increasing amounts of strain from the top left counter clockwise to the bottom right.

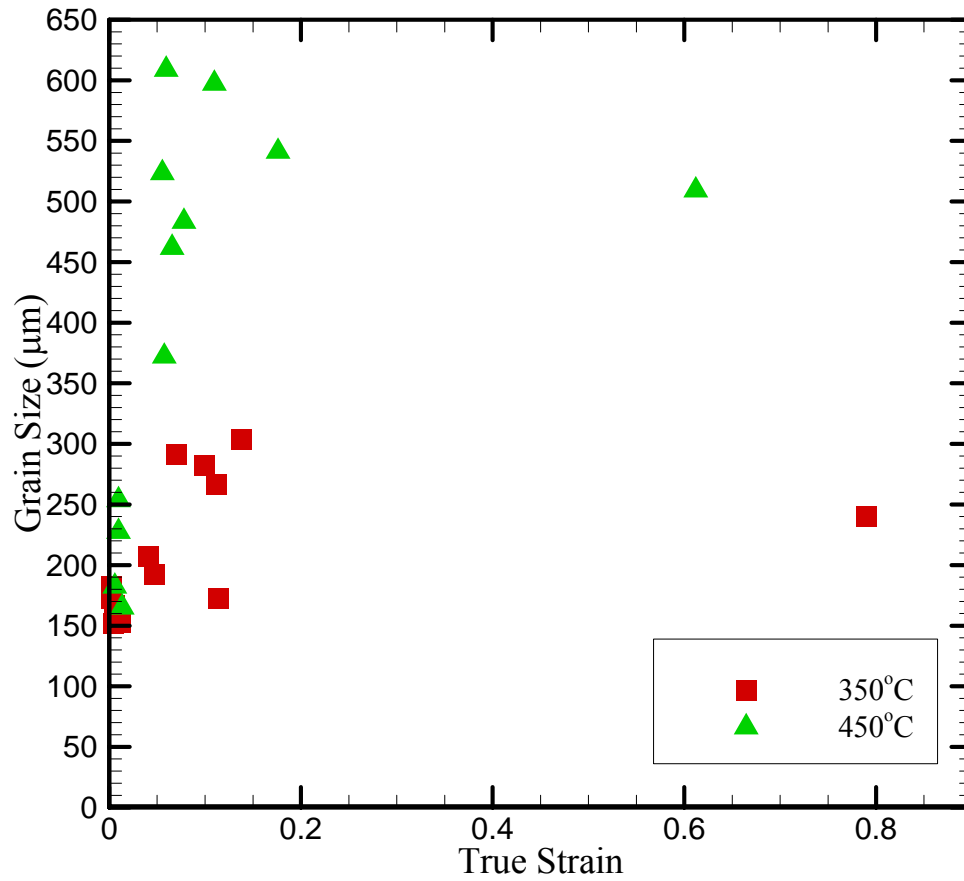


Figure 2.13: Average grain size shown as a function of the true strain measured in the thickness direction for pure magnesium tensile samples pulled at a constant strain rate of  $0.0001 \text{ s}^{-1}$  to failure at 350°C and 450°C.

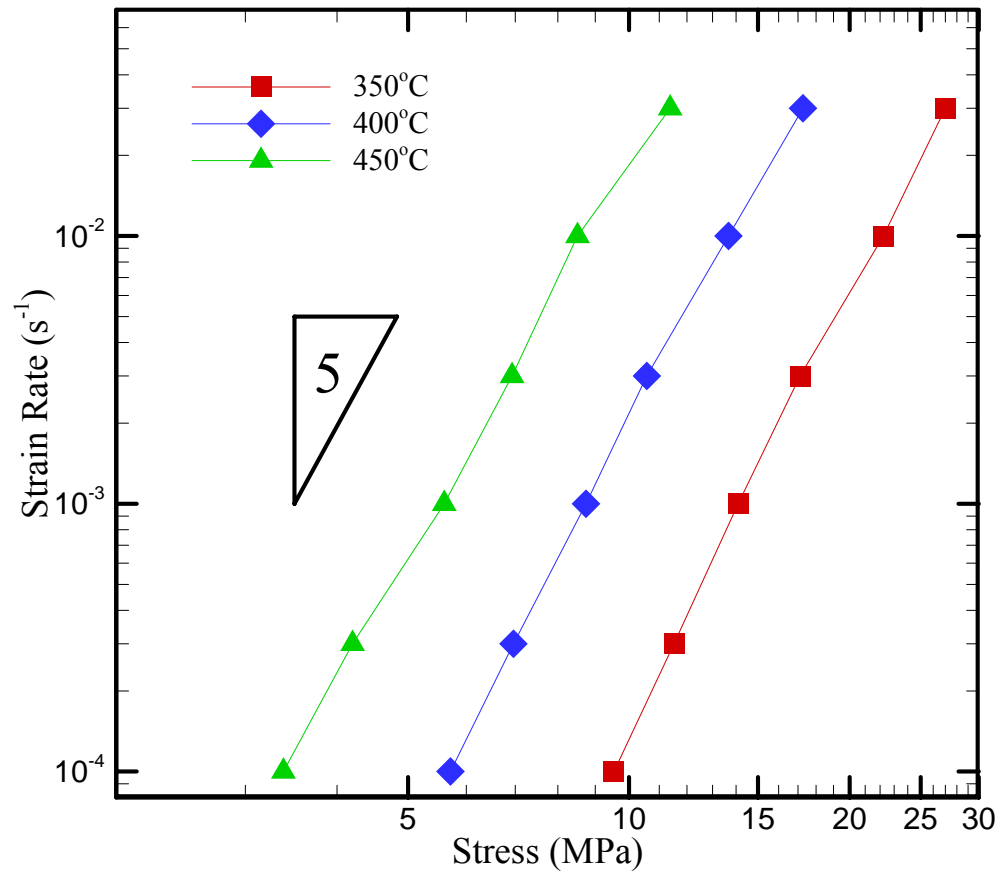


Figure 2.14: Strain rate as function of flow stress for pure magnesium tensile samples tested at 350°C, 400°C and 450°C. This plot was compiled from the results of the step strain rate tests.

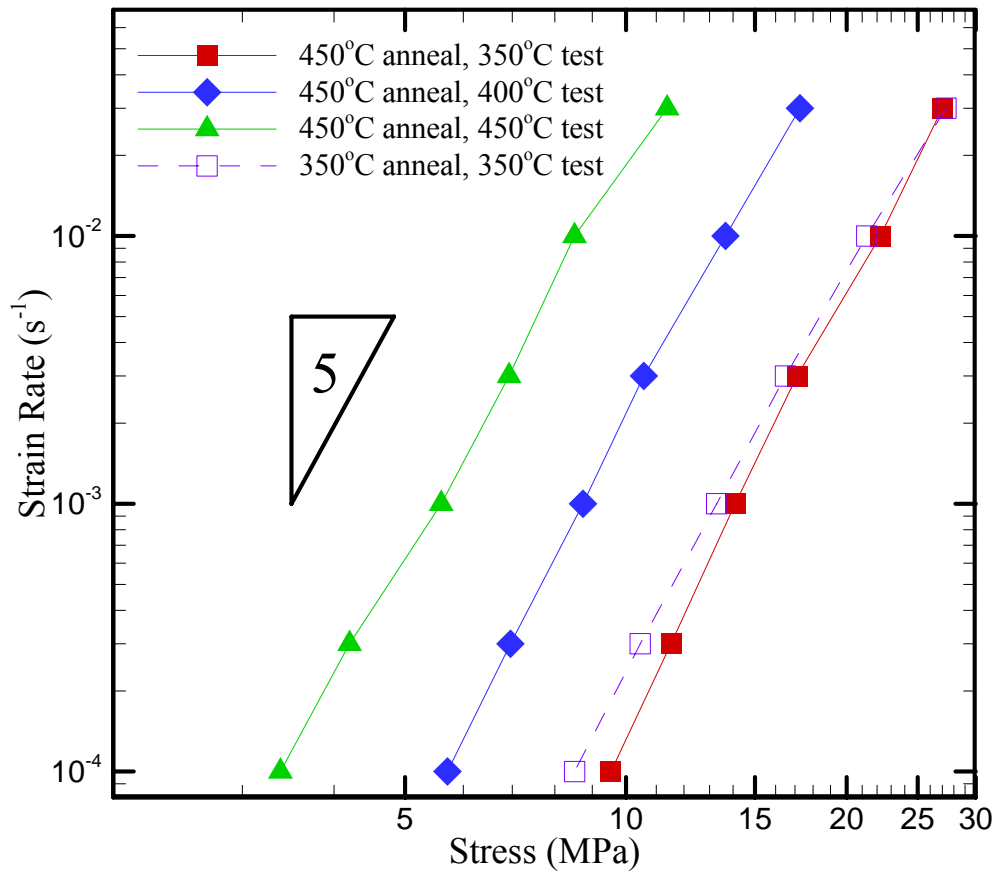


Figure 2.15: A fourth set of data points have been added to the plot from figure 2.13 to show the effect of annealing temperature, and thus the effect of initial grain size, on the strain rate as a function of flow stress in pure magnesium.

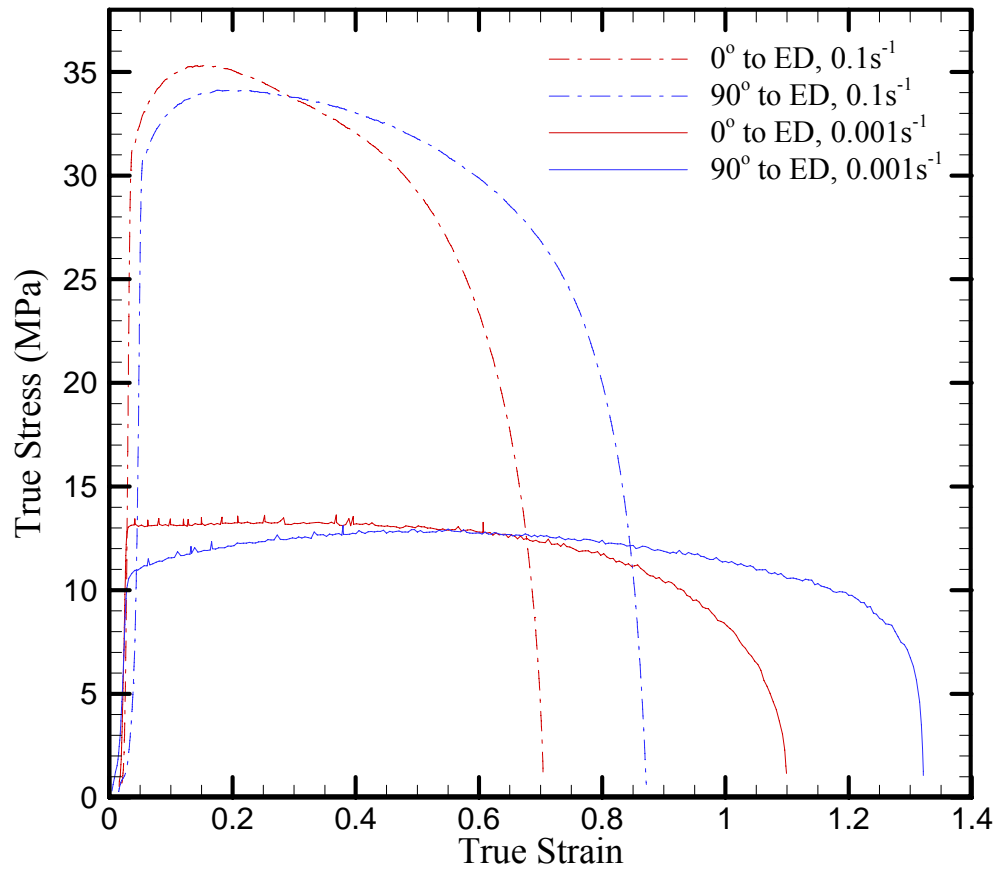


Figure 2.16: Stress vs. strain curves for magnesium AZ31 specimens oriented with the tensile axis 0° and 90° to the extruded direction tested at 450°C at a constant strain rate to failure of 0.1s<sup>-1</sup> and 0.001s<sup>-1</sup>.



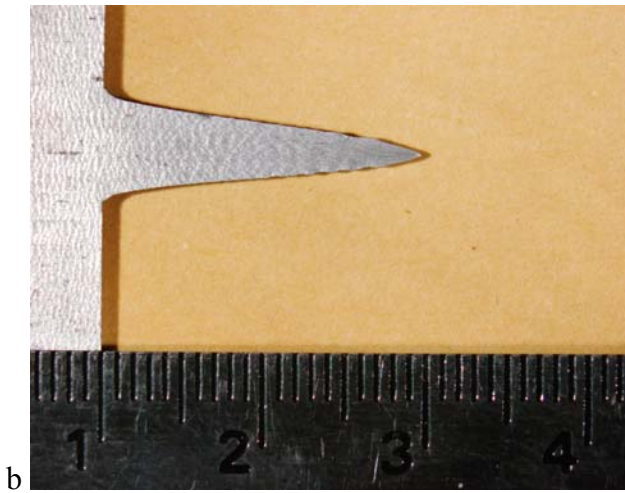


Figure 2.17: Fractured tensile specimens pulled at a constant strain rate of  $0.1\text{s}^{-1}$  to failure at  $450^\circ\text{C}$ . The tensile axis of (a) is oriented  $0^\circ$  to the ED and (b) is oriented  $90^\circ$  to the ED.

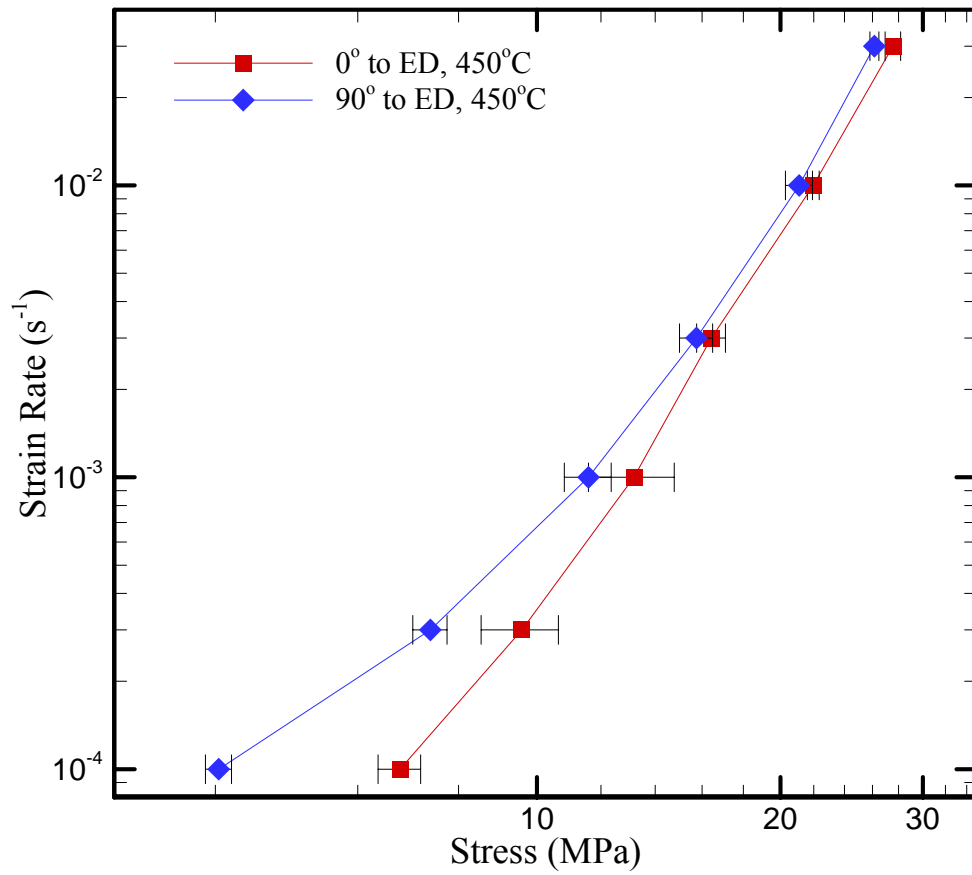


Figure 2.18: Strain rate as function of flow stress for the magnesium AZ31 specimens oriented so that the tensile axis is  $0^{\circ}$  and  $90^{\circ}$  to the extruded direction. This plot was compiled from the results of the step strain rate tests at  $450^{\circ}C$ .

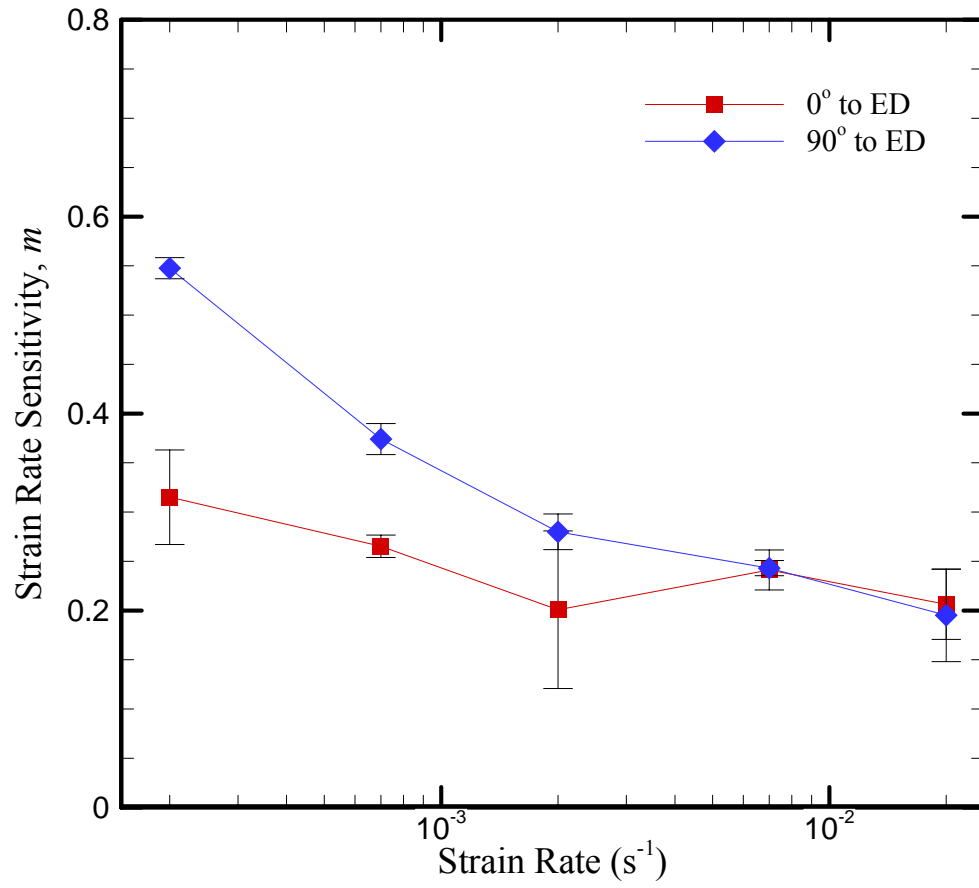


Figure 2.19: Strain rate sensitivity,  $m$ , plotted as a function of strain rate for both orientations, compiled from the results of the step strain rate tests at 450°C.

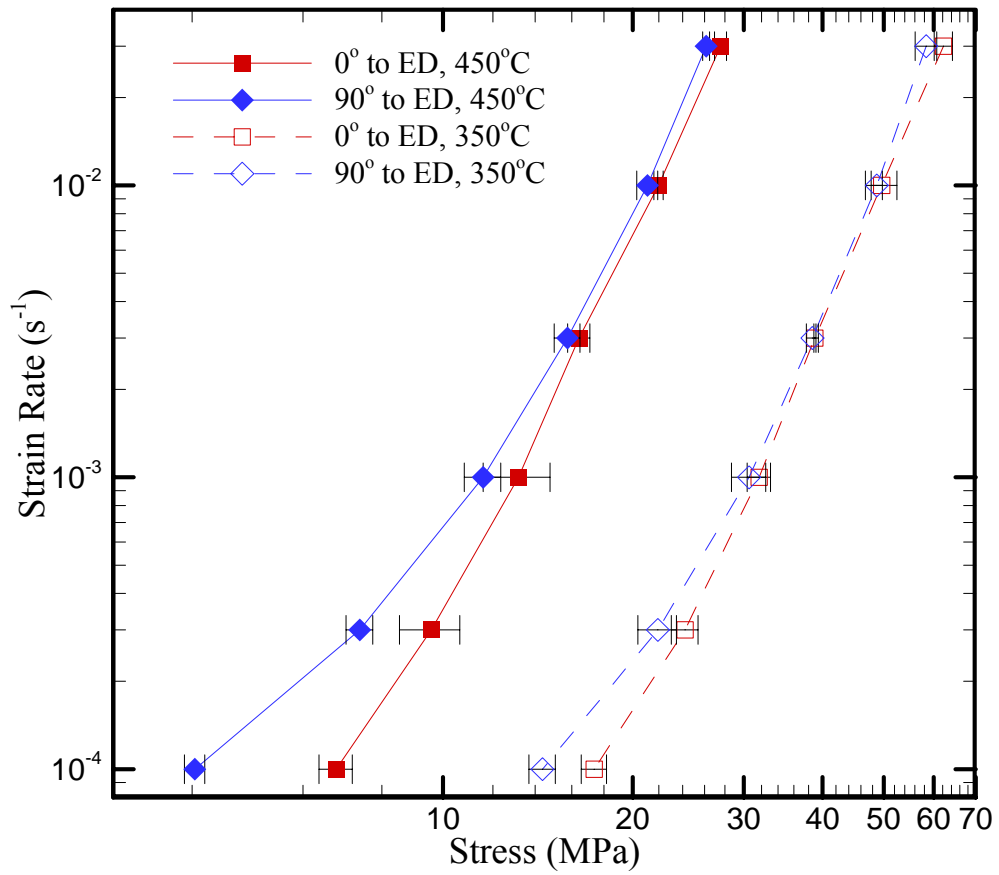


Figure 2.20: Strain rate plotted as a function of stress for tensile test where the loading was 0° and 90° to the ED at 350°C and 450°C.

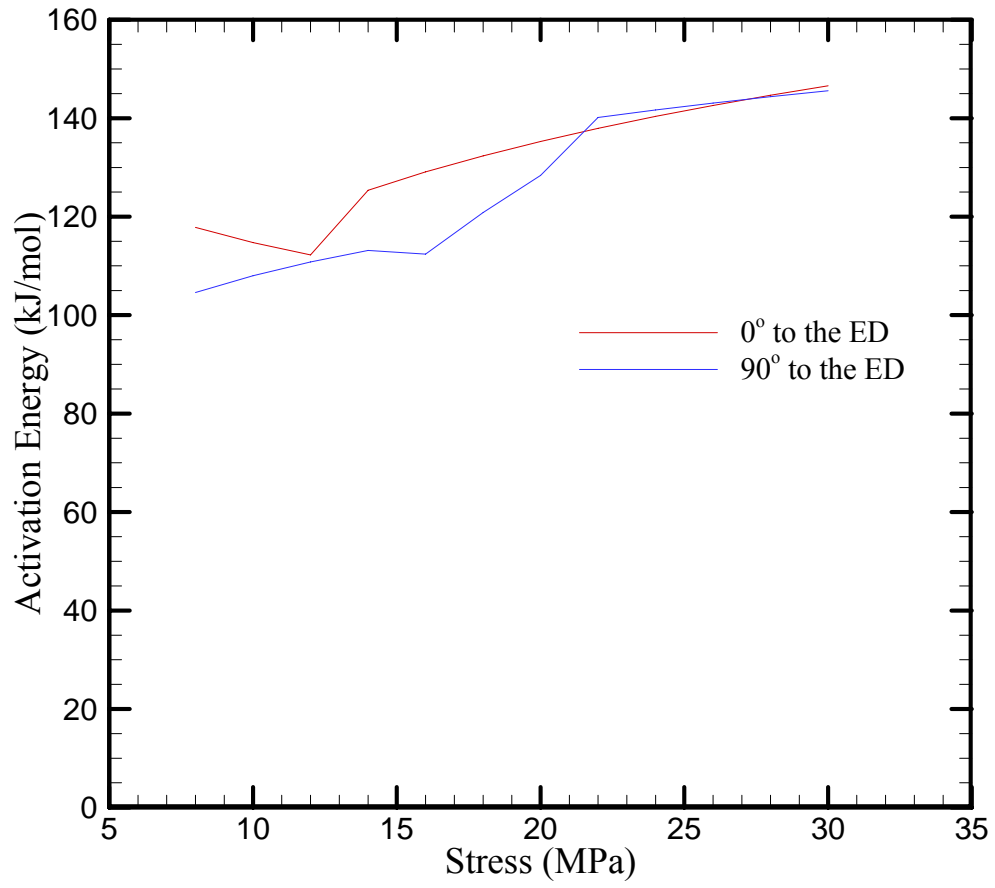


Figure 2.21: Activation energy for creep during elevated temperature tensile tests for both orientations of the tensile axis with respect to the ED plotted as function of stress.

## **CHAPTER 3: THE FINITE ELEMENT MODEL**

A microstructure based two-dimensional continuum finite element model was recently developed by Bower and Wininger to simulate the constitutive response of a polycrystalline material during high temperature plastic deformation (Bower & Wininger, 2004b). The model accounts for the following deformation mechanisms: dislocation creep within the grains as well as grain boundary sliding, grain boundary diffusion, grain boundary migration, and surface diffusion. Capabilities of the model include: computing the microstructure evolution, computing stress vs. strain curves, and computing the relative contribution to plastic strain from the various deformation mechanisms. Previously, the model has been used to predict the constitutive response of deformation in aluminum alloy 5083, (Agarwal, Briant, Krajewski, Bower, & Taleff, 2007a). This work was extended to study the constitutive behavior in AA5083 in response to a threshold stress for GBS, void growth, and heterogeneity in grain boundary sliding resistance (Du, 2009; Du, Bower, & Krajewski, 2010; Du, Bower, Krajewski, & Taleff, 2008; Chapter 6). The model has also been extended to three dimensions to study growth of tin whiskers (Buchovecky, Du, & Bower, 2009c).

A complete description of the finite element model, including the front tracking

method to model grain structure evolution and the method of mesh generation can be found in Bower and Winerger (Bower & Winerger, 2004b). A description of the model for small strain deformation is given in this chapter as background for its use to study the deformation mechanisms during elevated temperature straining of magnesium alloy AZ31. The results of this study will be given in Chapter 4 and 5 of this dissertation.

### **3.1 Formulation of the Finite Element Model**

The simulations use a continuum finite element method to simulate high temperature deformation mechanisms in polycrystals. The model idealizes a polycrystal as a two dimensional assembly of grains separated by sharp grain boundaries, an example of which can be observed in figure 1.14. The grains are modeled as single crystals that deform by intragranular dislocation creep. The grain boundaries are modeled as mobile interfaces that are allowed to displace along the interface due to grain boundary diffusion and grain boundary sliding. A more detailed description of the aforementioned deformation mechanisms that lead to plasticity in the idealized polycrystal are described in the following sections.

The polycrystal is subjected to boundary conditions that are intended to represent plane strain uniaxial extension. The boundaries at  $x_1 = 0$  and  $x_2 = 0$  are assumed to be symmetry planes, while the boundary at  $x_2 = L_2$  is traction free. The boundary at  $x_1 = L_1$  is free of vertical traction, and is subjected to history of displacement, which is intended to emulate uniaxial extension at constant strain rate  $\dot{\epsilon}_{11} = \dot{\epsilon}$ . The loading induces a distribution of displacement,  $u_i$ , and Cauchy stress,  $\sigma_{ij}$ , in the solid. The main objective

of the calculations is to determine the average stress,

$$\sigma = \frac{1}{V} \int_V \sigma_{11} dV \quad (3.1)$$

as a function of the applied strain rate.

The finite element simulations are used to calculate the stress and displacement distributions induced in the microstructure shown in figure 1.14 by plane-strain uniaxial extension. The results are used to deduce the volume average uniaxial stress  $\sigma$  (defined in eq. 3.1) as functions of the applied uniaxial strain and strain rate (calculated from the displacements applied to the boundary of the microstructure). After a brief elastic transient, the uniaxial stress settles to a constant value, which depends on the applied strain rate. Consequently, focus is placed on the variation of steady-state flow stress  $\sigma$  as a function of uniaxial strain rate  $\dot{\epsilon}$ .

### 3.1.1 Intragranular Dislocation Creep

The idealized polycrystal is composed of an assembly of individual grains that are modeled as single crystals that deform by intragranular dislocation creep. Deformation is defined in the usual manner for crystal plasticity. A displacement vector  $\mathbf{u}(\mathbf{x}, t)$  is defined to describe the motion from a point  $x_i$  in the undeformed solid to a point  $y_i$  in the deformed solid,  $y_i = x_i + u(x_1, x_2, x_3, t)$ . The displacement gradient tensor is defined with respect to the undeformed configuration as  $\partial u_i / \partial x_j$ , and thus the deformation tensor  $\mathbf{F}$ , can be defined in the following manner



$$F_{ij} = \delta_{ij} + \frac{\partial u_i}{\partial x_j} = \frac{\partial y_i}{\partial x_j} \quad (3.2)$$

where  $\delta_{ij}$  is the Kronecker delta. Strain in the solid is defined using the infinitesimal strain tensor by assuming small strains, and thus the strain rate in the grains are defined as

$$\dot{\epsilon}_{ij} = \frac{1}{2} \left( \frac{\partial \dot{u}_i}{\partial x_j} + \frac{\partial \dot{u}_j}{\partial x_i} \right) \quad (3.3)$$

The strain rate can be decomposed into its components of elastic and plastic deformation as follows

$$\dot{\epsilon}_{ij} = \dot{\epsilon}_{ij}^e + \dot{\epsilon}_{ij}^p \quad (3.4)$$

In the case of magnesium the grains are modeled as single crystals with a hexagonal close packed (hcp) atomic packing structure with the relevant Young's modulus  $E$ , shear modulus  $\mu$ , and Poisson's ratio  $\nu$ . The elastic strain rate is related to the stress in the solid by the linear elastic constitutive equations for a transversely isotropic material,

$$\dot{\epsilon}_{ij}^e = S_{ijkl} \dot{\sigma}_{kl} \quad (3.5)$$

where the elastic constants for magnesium are taken from Freund and Suresh (Freund & Suresh, 2003) and listed in table 3.1. Plastic deformation within the grains is defined by shearing on the active slip systems. For each slip system  $\alpha$ , the slip plane is defined by the unit vector normal to the slip plane  $\mathbf{m}$  and the slip direction is defined by the unit vector parallel to the slip direction  $\mathbf{s}$ . The magnesium model accounts for the following slip systems: the basal slip system  $(0001)[11\bar{2}0]$ , the prismatic slip system  $(10\bar{1}0)[11\bar{2}0]$ , and the pyramidal slip system  $(11\bar{2}2)[\bar{1}\bar{1}23]$ . The basal and prismatic

system contain  $\langle a \rangle$  type Burgers vectors and the pyramidal slip system contains the  $\langle c + a \rangle$  Burgers vector. The plastic strain rate is defined as the sum of the shear rate on each slip system as follows,

$$\dot{\epsilon}_{ij}^p = \sum_{\alpha=1}^N \dot{\gamma}^{\alpha} (q^{\alpha}, \tau_o^{\alpha}) \frac{(s_i^{\alpha} m_j^{\alpha} + s_j^{\alpha} m_i^{\alpha})}{2} \quad (3.6)$$

where  $\dot{\gamma}^{\alpha} (q^{\alpha}, \tau_o^{\alpha})$  is the shear rate on slip system  $\alpha$ , and  $N$  is the number of slip systems.

The shear rate on each system is calculated as a function of the resolved shear stress,  $q^{\alpha} = s_i^{\alpha} \sigma_{ij} m_j^{\alpha}$ , and the strength  $\tau_o^{\alpha}$ , of the slip system  $\alpha$ , which in the case of magnesium is different for the various slip systems. The shear rate on the slip system is defined using a power-law viscous relation as follows

$$\dot{\gamma}^{\alpha} = \dot{\gamma}_o^{\alpha} \left( \frac{q^{\alpha}}{\tau_o^{\alpha}} \right)^n \quad (3.7)$$

where  $n$  is the stress exponent. The power law relation has shown better agreement to experimental data for aluminum and magnesium material models, than the thermally activated dislocation climb-plus-glide model that was originally employed in this model. The model does not account for twinning, which is not evident during elevated temperature deformation in magnesium. Although strain hardening the model is able to account for strain hardening in the solid, it has been turned off in this case. As seen in figure 2.10 for pure magnesium, where dislocation creep is dominant for the entire range of strain rates, there is negligible amounts of hardening during tensile tests at a constant strain rate to failure at 450°C. Hardening is also assumed to be negligible during the step strain rate tests used to compile the strain rate vs. stress curves, which are used to calibrate the model. Thus, it will not be considered here.

### 3.1.2 Grain Boundary Diffusion

Individual grains are separated by grain boundaries that are modeled by a sharp interface approximation. A sample grain boundary between two generic grains can be observed in figure 3.1. In the figure,  $s$  denotes arc length measured from some convenient point on the grain boundary,  $\mathbf{t}$  and  $\mathbf{n}$  denote unit vectors in the tangent and normal direction to the boundary respectively,  $j_n$  denotes the volumetric flux of material from one grain to the other, and  $j_t$  denotes the volumetric flux of material tangent to the grain boundary. The flux of material along the grain boundary is driven by a change in the chemical potential across the interface. For grain boundary diffusion the chemical potential gradient is a function of the normal stress  $\sigma_n = \sigma_{ij}n_i n_j$ , acting on the interface

$$\mu = -\Omega\sigma_n \quad (3.8)$$

The flux of atoms moving along the grain boundary is defined as a function of the chemical potential  $\mu$ , and likewise as a function of the normal stress on the grain boundary as

$$\bar{j} = -\frac{\delta D_{GBD} \exp\left(-Q_{GBD}/kT\right)}{kT} \frac{\partial}{\partial s} \mu = \frac{\Omega \delta D_{GBD} \exp\left(-Q_{GBD}/kT\right)}{kT} \frac{\partial}{\partial s} \sigma_n \quad (3.9)$$

where  $D_{GBD}$  is the pre-exponential for diffusion,  $Q_{GBD}$  is the activation energy for diffusion,  $\delta$  is the total thickness of the diffusion layer,  $s$  is the arc length measured from some convenient point on the grain boundary,  $k$  is the Boltzmann constant, and  $T$  is the temperature.

During the grain boundary diffusion process a gradient in the chemical potential drives atom migration so that the total free energy of the system is relaxed. Mass transport occurs between regions of the grain boundary under a compressive normal stress and regions of the grain boundary under tension. Due to the opposing stresses, material points on the interface are stretched in opposing directions leading to a discontinuity in the velocity field across the grain boundary. The velocity jump in the normal direction to the boundary in terms of the displacement on each side of a generic grain boundary is defined as follows,

$$[v_n] = (\dot{u}_i^+ - \dot{u}_i^-) n_i \quad (3.10)$$

and in terms of the flux of material across the grain boundary,

$$[v_n] = -\frac{\partial}{\partial s} \cdot \vec{j} \quad (3.11)$$

where  $u_i$  denotes displacement of the grains immediately adjacent to the boundary and  $\mathbf{n}$  is the normal vector to the grain boundary. Thus the velocity discontinuity is defined in terms of the normal stress on the grain boundary by the following linear diffusion law

$$[v_n] = -\frac{\Omega \delta D_{GBD} \exp\left(\frac{-Q_{GBD}}{kT}\right)}{kT} \frac{\partial^2}{\partial s^2} \sigma_n \quad (3.12)$$

### 3.1.3 Grain Boundary Sliding

The grain boundaries also provide a path for grain boundary sliding to occur between neighboring grains. The resolved shear stress on the grain boundary causes a discontinuity in the velocity field to develop along the grain boundary in the tangential direction. This is similar to the case for grain boundary diffusion and can be defined as

$$[v_t] = (\dot{u}_i^+ - \dot{u}_i^-) t_i \quad (3.13)$$

where  $u_i$  denotes displacement of the grains immediately adjacent to the boundary and  $\mathbf{t}$  is the tangent vector to the grain boundary. The velocity discontinuity is related to the resolved shear stress on the grain boundary by the following linear viscous equation

$$[v_t] = \eta \sigma_t \quad (3.14)$$

where  $\eta$  is the fluidity of the grain boundary or likewise as the inverse of the grain boundary viscosity, and the shear stress is defined as  $\sigma_t = \sigma_{ij} t_i n_j$ . The fluidity of the grain boundary  $\eta$  is defined in the following manner

$$\eta = \frac{\Omega \eta_o \exp\left(\frac{-Q_{GBS}}{kT}\right)}{kT} \quad (3.15)$$

where  $\eta_o$  is a characteristic sliding velocity,  $Q_{GBS}$  is the activation energy for grain boundary sliding,  $k$  is the Boltzmann constant, and  $T$  is temperature, however in this work  $\eta$  has been defined independently.

### 3.1.4 Grain Boundary Triple Junctions

All grain boundaries end at either a triple junction or at the edge of the microstructure. For the grain boundaries that end at a triple junction, atoms are allowed to diffuse through the triple junction from one boundary to another. To maintain the restriction that the chemical potential at the endpoint of each grain boundary within a generic triple junction must remain in equilibrium, it is assumed that the flux of material

occurs at a rapid rate. To enforce this restriction a penalty method is used to ensure thermodynamic equilibrium. There is no mass flux through the endpoint of a grain boundary on the edge of the microstructure.

### 3.1.5 Mechanical Equilibrium

The objective is to calculate the distribution of stress and strain along with the change in crystallographic orientation within each grain as well as the motion of the grain boundaries and surfaces as a function of time. As is the case for any finite element solution to a deformable solid, the mechanical field quantities are approximated by a finite element method that utilizes a form of the virtual work equation. The form below is a general form of the virtual equation that allows for the velocity field to be discontinuous across the grain boundaries.

$$\int_{V_{t+\Delta t}} \sigma_{ij} \delta L_{ij} dV - \int_{\partial V_{t+\Delta t}} p_i^* \delta v_i ds + \int_{\Gamma_{t+\Delta t}} \sigma_n (\delta v_i^+ - \delta v_i^-) n_i ds + \int_{\Gamma_{t+\Delta t}} \sigma_t (\delta v_i^+ - \delta v_i^-) t_i ds = 0 \quad (3.16)$$

where  $V_{t+\Delta t}$  denotes the volume occupied by grains at time  $t + \Delta t$ ,  $\sigma_{ij}$  denotes the Cauchy stress inside the grains as a function of the change in displacement  $\Delta u_i$  at time  $t + \Delta t$ ,  $\delta v_i$  is a virtual velocity field which is continuous across the grains and may be discontinuous across the grain boundary at time  $t + \Delta t$ ,  $\delta L_{ij} = (\partial v_i / \partial x_j + \partial v_j / \partial x_i) / 2$  is the virtual velocity gradient,  $\sigma_n$  is the stress normal to the grain boundary, and  $\sigma_t$  is the stress tangential to the grain boundary. Equation 3.16 is altered using a Lagrange

multiplier to take into account the constraints on the movement of the grain boundary due to grain boundary diffusion (equation 3.12) and sliding (equation 3.14). Changes in the reference configuration are neglected over  $\Delta t$ , thus  $V_{t+\Delta t} \approx V_t$ , and so forth for each integral. Thus the virtual work equation becomes

$$\begin{aligned}
& \int_{V_t} \sigma_{ij} \delta L_{ij} dV - \int_{\partial V_t} p_i^* \delta v_i ds + \int_{\Gamma_t} \sigma_n (\delta v_i^+ - \delta v_i^-) n_i ds \\
& + \int_{\Gamma_t} \left( (v_i^+ - v_i^-) n_i - \frac{\Omega \delta_{GB} D_{GBD} \exp\left(-Q_{GBD}/kT\right)}{kT} \frac{\partial^2}{\partial s^2} \sigma_n \right) \delta \sigma_n ds \\
& + \int_{\Gamma_t} \sigma_t (\delta v_i^+ - \delta v_i^-) t_i ds + \int_{\Gamma_t} \left( (v_i^+ - v_i^-) t_i - \eta \sigma_t \right) \delta \sigma_t ds = 0
\end{aligned} \tag{3.17}$$

If integration by parts is applied to the fourth integral of equation 3.17 and then the divergence theorem is applied to the result the previous equation can be simplified to give

$$\begin{aligned}
& \int_{V_t} \sigma_{ij} \delta L_{ij} dV - \int_{\partial V_t} p_i^* \delta v_i ds + \int_{\Gamma_t} \sigma_n (\delta v_i^+ - \delta v_i^-) n_i ds \\
& + \int_{\Gamma_t} (v_i^+ - v_i^-) n_i \delta \sigma_n ds + \int_{\partial \Gamma_t} j_i n_i \delta \sigma_n ds \\
& + \int_{\Gamma_t} \left( \frac{\Omega \delta_{GB} D_{GBD} \exp\left(-Q_{GBD}/kT\right)}{kT} \frac{\partial}{\partial s} \sigma_n \right) \frac{\partial \delta \sigma_n}{\partial s} ds \\
& + \int_{\Gamma_t} \sigma_t (\delta v_i^+ - \delta v_i^-) t_i ds + \int_{\Gamma_t} \left( (v_i^+ - v_i^-) t_i - \eta \sigma_t \right) \delta \sigma_t ds = 0
\end{aligned} \tag{3.18}$$

where  $j$  is the total flux of atoms flowing into a grain boundary by grain boundary diffusion.

In response to a prescribed displacement applied to the boundary over a time  $\Delta t$ , equation 3.18 is solved by the finite element method to determine the velocity field ( $v_i$ ) in the microstructure and the stress along the grain boundaries ( $\sigma_n, \sigma_t$ ). For this to occur a

mesh was generated using the advancing front algorithm (Peraire, Vahdati, Morgan, & Zienkiewicz, 1987). The grains are meshed using six-noded triangular elements that have degrees of freedom for displacement (in the 1 and 2 direction for two dimensions). The interface elements are added after the grain interiors have been meshed to connect the neighboring grains. These nine-noded line elements are implemented along the boundary so that nodes 1-6 share the displacement degrees of freedom with the upper and lower grain, and nodes 7-9 carry the normal and tangential stress degrees of freedom. The three sets of three nodes coincide in space so that the boundary has essentially no thickness.

### 3.1.6 Strain Rate Computations

The stress and displacement fields in the microstructure are provided by the finite element calculations, but a secondary function of the code is to determine the contribution to the total strain rate from each of the deformation mechanisms (dislocation creep, grain boundary diffusion, and grain boundary sliding). The plastic strain rate due to dislocation creep can be determined from the shearing rates on each slip systems within the grains, whereas the plastic strain rate due to grain boundary diffusion and sliding can be determined from the velocity discontinuity across the grain boundaries. The definitions for the strain rate calculations are as follows

$$\begin{aligned}
 \dot{\epsilon}_{ij}^{dislocation} &= \frac{1}{V} \int_V \sum_{\alpha} \dot{\gamma}^{\alpha} \frac{1}{2} (s_i^{\alpha} m_j^{\alpha} + s_j^{\alpha} m_i^{\alpha}) dV \\
 \dot{\epsilon}_{ij}^{diffusion} &= \frac{1}{V} \int_{\Gamma} [v_n] n_i n_j ds \\
 \dot{\epsilon}_{ij}^{sliding} &= \frac{1}{V} \int_{\Gamma} [v_t] \frac{1}{2} (n_i t_j + n_j t_i) ds
 \end{aligned} \tag{3.19}$$



where  $V$  is the area of the entire microstructure and  $\Gamma$  is the sum of all grain boundaries within  $V$ .

Calibration and validation of the fitting parameters for the constitutive laws for dislocation creep, grain boundary diffusion, and grain boundary sliding will be explained in the following chapter.

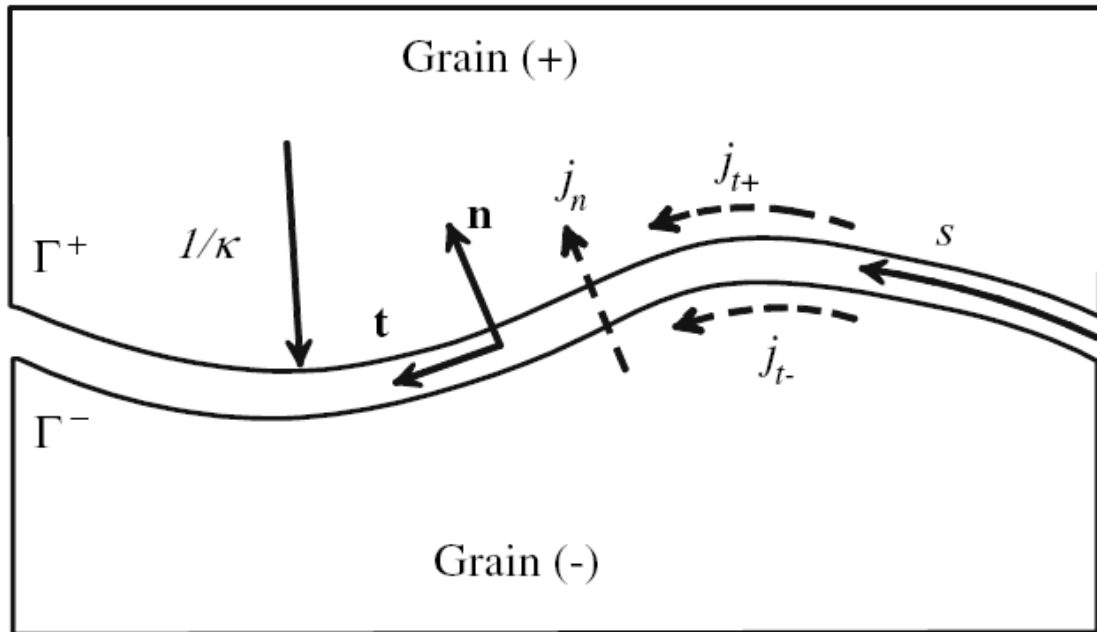


Figure 3.1: Schematic of a grain boundary in the finite element model.

Table 3.1: Elastic constants for magnesium (Freund and Suresh, 2003).

*Elastic Constants for Magnesium*

$c_{11}$	59.7
$c_{33}$	61.7
$c_{44}$	16.4
$c_{12}$	26.2
$c_{13}$	21.7

(\*all values are in GPa, given in the form,  $\sigma_{ij} = C_{ijkl}\epsilon_{kl}$ )

## **CHAPTER 4: VALIDATION AND APPLICATION OF THE MODEL TO MAGNESIUM ALLOY AZ31**

Calibration and validation of the model has been performed by utilizing experimental data of elevated temperature tensile tests on magnesium alloy AZ31 sheet with various starting grain sizes. The data was used to calibrate the fitting parameters of the model and then to validate the predicted results. This process is explained within the present chapter. Next, the validated model was then applied to investigate the anisotropic behavior of extruded magnesium AZ31 sheet described in chapter 2. This investigation will be explained in chapter 5.

The model was validated using experimental data performed at the General Motors Research and Development Center in Warren, MI by Verma (Verma, 2010e). The data was ideal for validating the model because it involved results for multiple grain sized material. The benefit of utilizing data from multiple grain sizes is that different mechanisms are likely to become dominant based on the grain size, and thus calibrating the model against the different grain sizes and the mechanisms that are dominant at those grain sizes is necessary. Furthermore, it is crucial that the model is valid over a range of grain sizes.

In an attempt to model magnesium AZ31 most accurately, the starting microstructure used by the finite element simulations was taken directly from an actual micrograph of magnesium AZ31. In this way the topography of the actual material could be captured as input to the model including the grain shape, the relative size of the grains, the path of the grain boundaries, and the orientation of the grains. This was done by taking a micrograph obtained using the EBSD method on the SEM and mapping the grain and grain boundary information into a format that could be understood by the finite element code. Figure 4.1 shows a comparison between the micrograph obtained by EBSD and the simulation micrograph. The grains show good agreement with the actual data and although the texture is not shown on the simulation micrograph it has been mapped directly from the EBSD data. The grain size of the experimental micrograph was measured to be  $16\mu\text{m}$ . Rather than construct two additional simulation micrographs for the other grain size material used in the calibration and validation, a scaling technique was used to scale the simulation parameters to simulate the smaller and larger grain sizes. Three dimensionless parameters were constructed to describe strain rate, sliding, and plasticity using the material parameters listed in table 4.1, each of which included the grain size,  $L$ , of the material. The dimensionless parameters are defined as follows:

$$\begin{aligned}
 K_{StrainRate} &= \frac{\dot{\epsilon}kTL^3}{\sigma_Y\Omega\delta D_{GBD} \exp\left(-Q_{GBD}/kT\right)} \\
 K_{Plasticity} &= \frac{\dot{\gamma}_o kTL^3}{\sigma_Y\Omega\delta D_{GBD} \exp\left(-Q_{GBD}/kT\right)} \\
 K_{Sliding} &= \frac{\eta kTL^2}{\Omega\delta D_{GBD} \exp\left(-Q_{GBD}/kT\right)}
 \end{aligned} \tag{4.1}$$

Alternatively, three dimensionless parameters were also constructed to describe strain rate, sliding, and plasticity using the parameters provided as input to the finite element model. Equality is required between the corresponding parameters. Thus, a change in grain size can be accounted for in the model by scaling the simulation parameters based on a change in the grain size.

#### **4.1 Determination and Calibration of Model Parameters**

The first step in calibrating the model was to determine values for the number of material properties in the model, which are listed in table 4.1. The values of most parameters were taken from literature data, including: the atomic volume for magnesium, a common constant found in literature; the elastic constants used to determine the elastic component of strain rate in the microstructure, taken from Freund and Suresh (Freund & Suresh, 2003); the activation energy for grain boundary diffusion, from Frost and Ashby (Frost & Ashby, 1982); and the critical resolved shear stress (CRSS) for the slip systems in magnesium, of which there is some debate on the appropriate values. It is universally accepted that the plastic response of magnesium single crystals is highly anisotropic, with a low CRSS for basal slip, and higher CRSS for pyramidal and prismatic slip. The strength of the different slip systems in magnesium was taken into account in the model by adjusting the characteristic flow stress  $\tau_0$  in equation 3.7. However, there is some uncertainty in the literature over what ratio should be used in polycrystal models. In this work the flow stresses of the HCP slip systems have the ratio, basal: prismatic: pyramidal = 4:10:11. These values were obtained from experimental work on single crystal

magnesium in both tension and compression, many of which are summarized by Barnett in his work to develop an expression for the proof stress in magnesium AZ31 (Barnett, 2003; Obara, Yoshinga, & Morozumi, 1973; Reed-Hill & Robertson, 1957; Ward Flynn, Mote, & Dorn, 1961; Yoo, Agnew, Morris, & Ho, 2001; Yoshinaga & Horiuchi, 1963). However, Hutchinson and Barnett have suggested that experiments on single crystals may not provide an accurate measure of the strengths of slip systems under the conditions of multiple slip that occur during deformation of polycrystals (Hutchinson & Barnett, 2010), and previous polycrystal models have used a range of values of slip system strengths. For example, Beausir et al used a ratio of basal: prismatic: pyramidal = 1:8:6 (Beausir, Toth, & Neale, 2007). The computations were repeated with this ratio, but the predicted flow stresses were found to change by less than 2.5 percent.

In addition to the material parameters taken from literature, there are four adjustable parameters which must be fit to experimental results. These are the stress exponent  $n$  defined in eq.3.7, the fluidity of grain boundary sliding,  $\eta$ , defined in eq. 3.14, the grain boundary diffusion coefficient,  $\delta_{GB}D_{GBD}$ , defined in eq. 3.12, and the characteristic strain rate,  $\dot{\gamma}_0$ , defined in eq. 3.7. Values for these parameters were determined by fitting the predicted flow behavior to experimental measurements reported by Verma (Verma, 2010e). In his work, a thermomechanical process was developed to produce sheet materials of various grain sizes. This process involved annealing the as-received sheet for 15 minutes at 350°C, then cold rolling the sheet at various reductions per pass ranging from 0.5 to 14.5 percent, before annealing the sheet a final time. Due to the various amounts of cold work induced in the sheet from rolling, different grain sizes were produced. Micrographs of these materials are shown in figure 4.2, their grain size

was measured using the linear intercept method in accordance with ASTM standard E112-96 to be  $50\mu\text{m}$ ,  $16\mu\text{m}$  and  $8\mu\text{m}$ , and will hereby be referred to by these values. The sheet material was tested in tension at multiple strain rates under elevated temperature by utilizing step strain rate tests. Plots of flow stress vs. strain rate for each material are shown in figure 4.3.

As can be observed in figure 4.3 the grain size has a significant effect on the flow stress as a function of the induced strain rate. The adjustable parameters were fit to this experimental data by making assumptions about the dominant mechanisms of deformation for the coarse and fine grain size material. The strain rate vs. stress curve for the  $50\mu\text{m}$  material remains fairly straight (on the logarithm plot), suggesting that there is very little change if any in the dominant deformation mechanism from high to low strain rates. If the curve is fit to the following general equation relating strain rate and stress, equation 2.1, the stress exponent is approximately 5 at high strain rates and drops closer to 4 at low strain rates. A stress exponent of this magnitude is characteristic of dislocation creep dominated flow. Furthermore, as previously stated GBS is unlikely for large grain size material. Thus, dislocation creep is assumed to be dominant for the coarse grain size samples and consequently, the stress exponent was chosen to fit the variation of flow stress with strain rate in this material. Subsequently, the value of grain boundary sliding fluidity and the grain boundary diffusion coefficient were chosen to fit the flow behavior of the material with  $8\mu\text{m}$  grain size. The strain rate vs. stress curve for this material shows a transition from high to low strain rates indicating a change in the dominant deformation mechanisms. At high strain rates the stress exponent is approximately equal to 5, but at low strain rates the stress exponent drops to below 2, a value characteristic of grain



boundary sliding.

The model's prediction of flow stress as a function of strain rate for a starting microstructure of  $50\mu\text{m}$ ,  $16\mu\text{m}$  and  $8\mu\text{m}$ , is shown in figure 4.4 along with the experimental results. The model shows good agreement with experiment for the  $50\mu\text{m}$  and  $8\mu\text{m}$  plots, as expected because the fitting parameters were calibrated with this data. To prove the validity of the fitting parameters and the assumptions, the data for the material with  $16\mu\text{m}$  grain size was *not* used in fitting, and therefore, the comparison in figure 4.4 for the  $16\mu\text{m}$  material serves to validate the predictions of the model. The model clearly captures the variation of flow stress over the entire range of strain rate, for all three grain sizes.

However, the model assumes an equiaxed grain structure, which is true for the  $8\mu\text{m}$  and  $16\mu\text{m}$  grain size material (figure 4.2a and 4.2b), but is not true for the  $50\mu\text{m}$  material (figure 4.2c). The  $50\mu\text{m}$  material displays a bimodal microstructure dominated by large grains on the order of  $50\mu\text{m}$  with pockets of smaller grains on the order of  $8\mu\text{m}$ . The small grains do not form a necklace structure around the large grains but are clumped together in patches distributed throughout the micrograph. Due to the small grain size of these grains it is assumed that they will deform by grain boundary sliding and thus the stress in these pockets will be greatly reduced. However, due to the substantially lower stresses that are needed for grain boundary sliding to occur and the small fraction of these pockets of small grains compared to the total area, deformation will be dominated by dislocation creep within the large grains. This is evident by the fairly constant stress exponent for the  $50\mu\text{m}$  material. Although, the flow curve has probably shifted to the left slightly due to the grain boundary sliding that dominates deformation within these

pockets of small grains.

## 4.2 Distribution of Strain Rate by Deformation Mechanism

A distinct advantage of the model is the ability to parse the total strain rate into the contribution from each of the deformation mechanisms considered in the model. The relative contributions to plastic strain from dislocation creep, grain boundary sliding, and grain boundary diffusion, are shown in figure 4.5. These results confirm that the increase in stress exponent observed at high strain rates and in coarse grained solids is caused by a transition in deformation mechanism. In fine grained solids, and coarse grained materials deformed at low rates, deformation occurs primarily by grain boundary sliding, accompanied by either grain boundary diffusion (in fine grained materials) or dislocation creep (in coarse grained materials). At sufficiently high strain rates, the deformation transitions to predominantly dislocation creep. The critical strain rate where this transition occurs is highly sensitive to grain size; the transition point for the  $8\mu\text{m}$  grain size material occurs at about  $2.0 \times 10^{-3} \text{ s}^{-1}$ , whereas the transition point for the  $50\mu\text{m}$  grain size material occurs at  $10^{-5} \text{ s}^{-1}$ .

For magnesium it is instructive to consider the breakdown of strain rate due to dislocation creep into the fraction of slip on each slip system due to the varying strength and geometry of each system. Figure 4.6 shows the contributions from each slip system to the total plastic strain rate caused by dislocation creep. Note that the strain rate on each system is normalized by total plastic strain rate due to plastic shearing within the grains, which is significantly smaller than the total strain rate at low strain rates. The prismatic

slip systems contribute most significantly to slip, followed by the basal and pyramidal slip systems, respectively. The relative contribution from the various systems is weakly dependent on strain rate and grain size; the difference is almost nonexistent at high strain rates where dislocation creep is the dominant deformation mechanism. The dominance of the prismatic system is due to its orientation and the general basal texture of the starting microstructure. If all systems are assigned equal strengths, the prismatic system contribution is still dominant at approximately 65 percent of the strain, while basal and prismatic systems contribute 20 percent and 15 percent, respectively. Numerical tests suggest that the flow stress of the polycrystal is weakly sensitive to the relative strengths of the slip systems. Consequently, modifying dislocation core structure and mobility through alloying, which is a promising route to improving room temperature formability, is unlikely to significantly influence elevated temperature behavior.

### **4.1.3 Comparison of Magnesium and Aluminum**

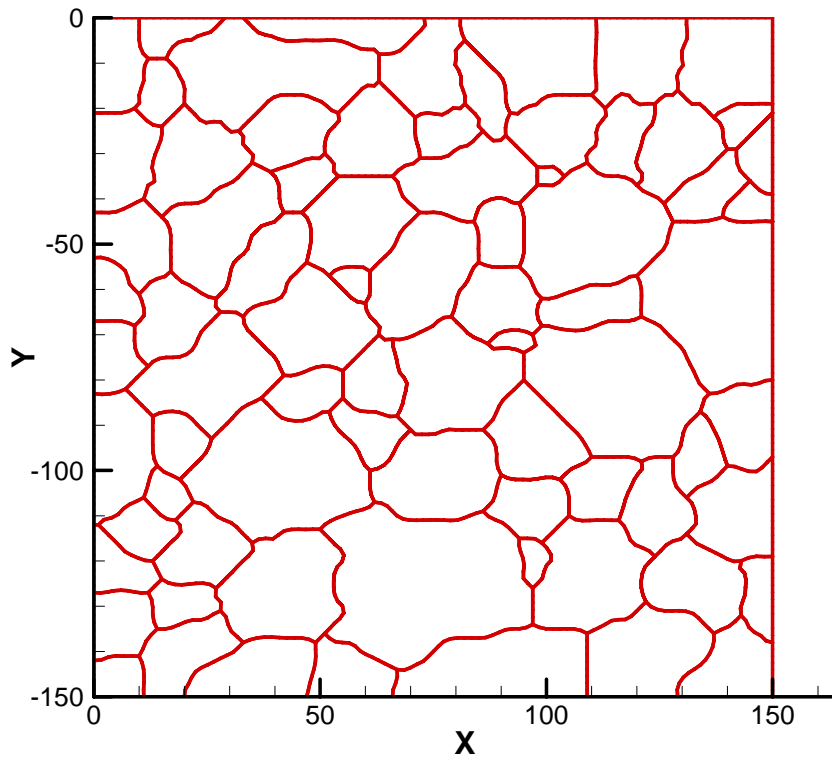
It is instructive to compare the behavior of magnesium alloys with the behavior of aluminum alloys. Magnesium shows a larger variation in stress exponent with strain rate than aluminum: for example, in the aluminum alloy 5083,  $n$  varies between 2.7 at low strain rates to approximately 4 at high strain rates (Kulas, Green, Taleff, Krajewski, & McNelley, 2005d), whereas in magnesium AZ31,  $n$  varies from 1.5 to 5. In addition, the transition from GBS dominated deformation to dislocation creep occurs at significantly higher strain rates in magnesium alloys than in aluminum alloys of similar grain size (approximately  $2.0 \times 10^{-3} s^{-1}$  in magnesium, compared to  $5.0 \times 10^{-4} s^{-1}$  in aluminum

(Agarwal, Briant, Krajewski, Bower, & Taleff, 2007a)). This difference is caused primarily by enhanced grain boundary sliding and diffusion in the magnesium alloy. Magnesium has higher grain boundary fluidity and higher rates of diffusion at 450°C than aluminum (Cipoletti, Bower, Qi, & Krajewski, 2009b). Furthermore, the simulations suggest that there is no threshold stress for grain boundary sliding in magnesium alloys, while AA5083 was found to have a 1 MPa grain boundary sliding threshold stress (Du, Bower, Krajewski, & Taleff, 2008c). Previous work on elevated temperature deformation in aluminum alloys used an equation similar to eq. 3.14 to model grain boundary sliding, but it was found that the low strain rate flow stress of aluminum cannot be predicted without a threshold stress for grain boundary sliding (Du et al., 2008c). Thus, an equation similar to the equation shown in this work, but with a threshold stress for activation of GBS included, was developed to model GBS in aluminum. Interestingly, including a threshold stress was not required to model magnesium, thus equation 3.14 does not include a threshold stress. This conclusion is supported by the following work of del Valle and separately, of Zhang, which shows that a threshold stress becomes unnecessary to model deformation in magnesium AZ31 at elevated temperature (del Valle, Carreno, & Ruano, 2007; Zhang, Yin, Wang, & Han, 2006). However, in their models the threshold stress is contained in the power law for creep controlled by GBS, whereas, the threshold stress that was originally considered in this work was contained in equation 3.14. These trends discussed here are consistent with several recent studies which observed significant grain boundary sliding during warm deformation of magnesium alloys (Panicker, Chokshi, Mishra, Verma, & Krajewski, 2009). Sliding has also been suggested to contribute to room temperature deformation of fine-grained magnesium alloys

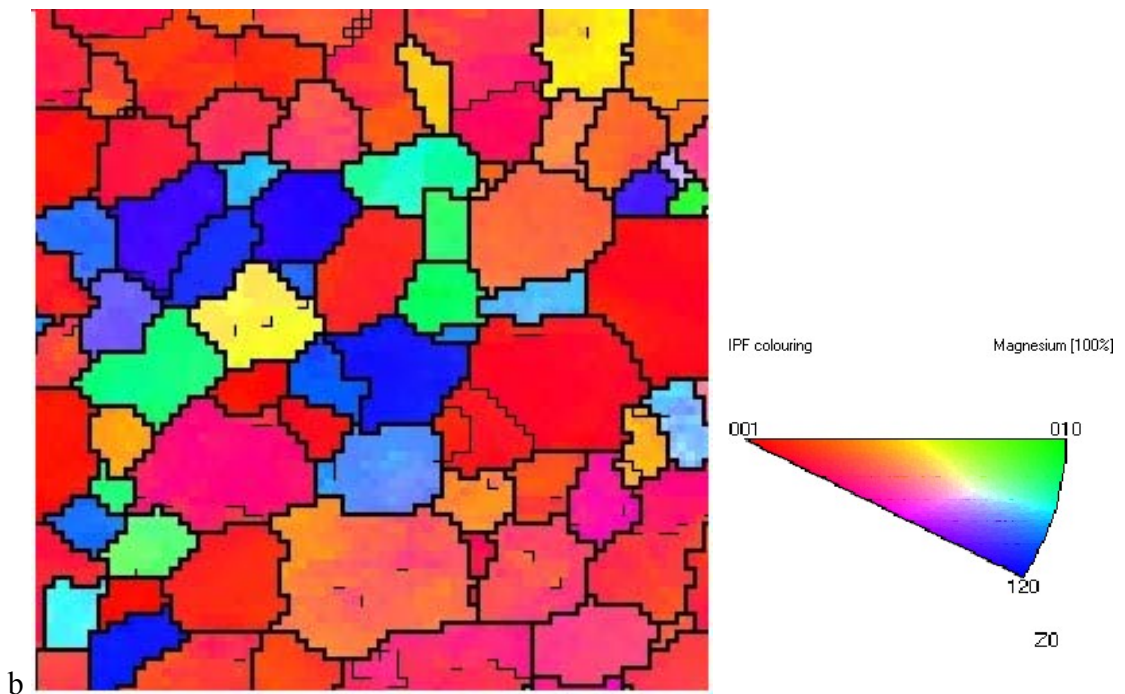
(Barnett, Ghaderi, Sabirov, & Hutchinson, 2009).

#### **4.1.4 Conclusions from Model Calibration and Validation**

In summary, it has been shown that the flow stress and deformation mechanisms in magnesium AZ31 alloy deforming at elevated temperature can be predicted by a polycrystal crystal plasticity model, which accounts for anisotropic dislocation creep within the grains, together with sliding and diffusion at grain boundaries. The predicted influence of grain size and strain rate on the flow stress was found to be in excellent agreement with experiment. The model shows that dominant deformation mechanism in magnesium transitions from dislocation creep to grain boundary sliding at a critical strain rate, which depends strongly on the grain size of the alloy. The behavior of magnesium alloys is similar to aluminum alloys, but the simulations suggest that magnesium has greater grain boundary fluidity and diffusion coefficients than aluminum, and no threshold stress for grain boundary sliding. It should be noted that only a small amount of strain is imposed on each system and thus the simulation microstructure is deformed only slightly. This is necessary for the continuity of the grains being deformed in the finite element mesh, however this allows for limited grain refinement or rotation of the grains. It is believed that this does not have a major impact on the conclusions of this work.



a



b

Figure 4.1: Comparison of the simulation microstructure (a) and the experimentally obtained microstructure using EBSD (b) for the specimen oriented  $0^\circ$  to the ED. The tensile direction is horizontally to the right.

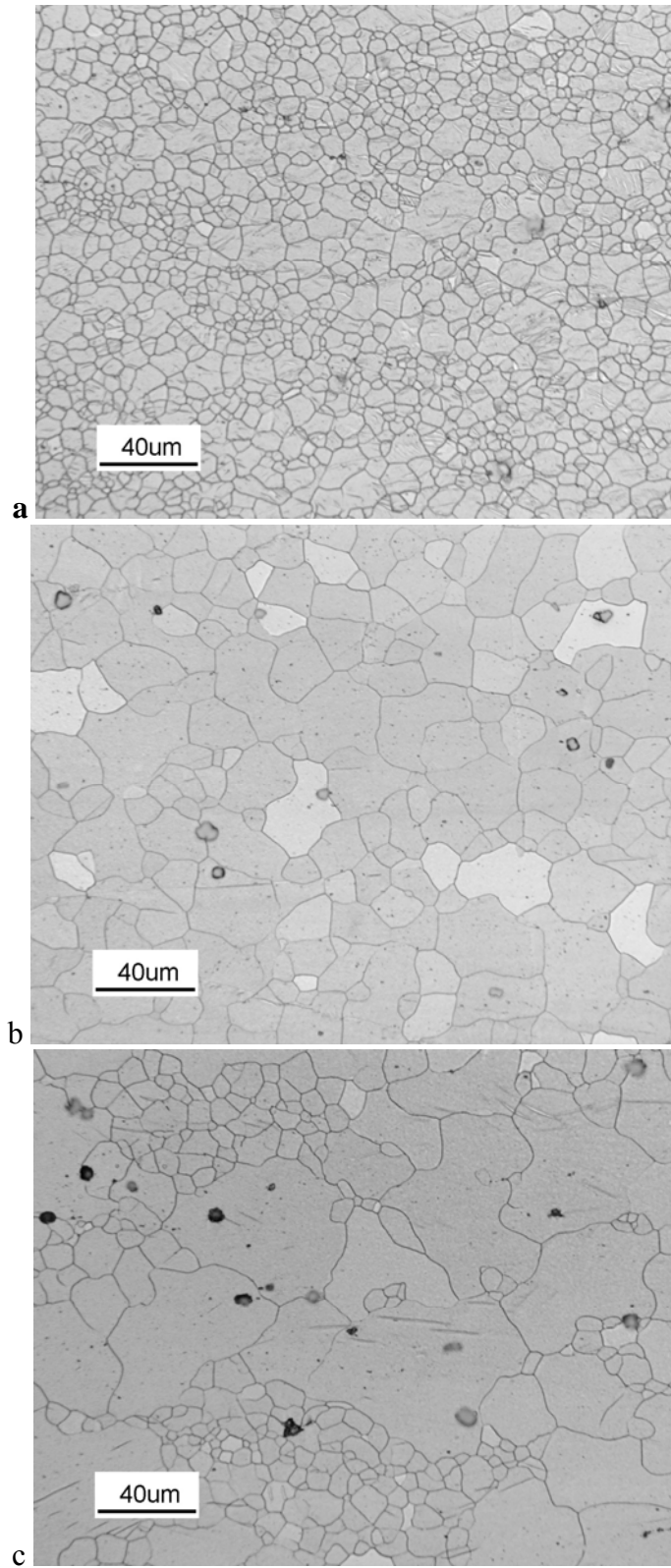


Figure 4.2: Optical micrographs of the three magnesium AZ31 sheet specimens with average grain size (a)  $8\mu\text{m}$ , (b)  $16\mu\text{m}$ , and (c)  $50\mu\text{m}$ .

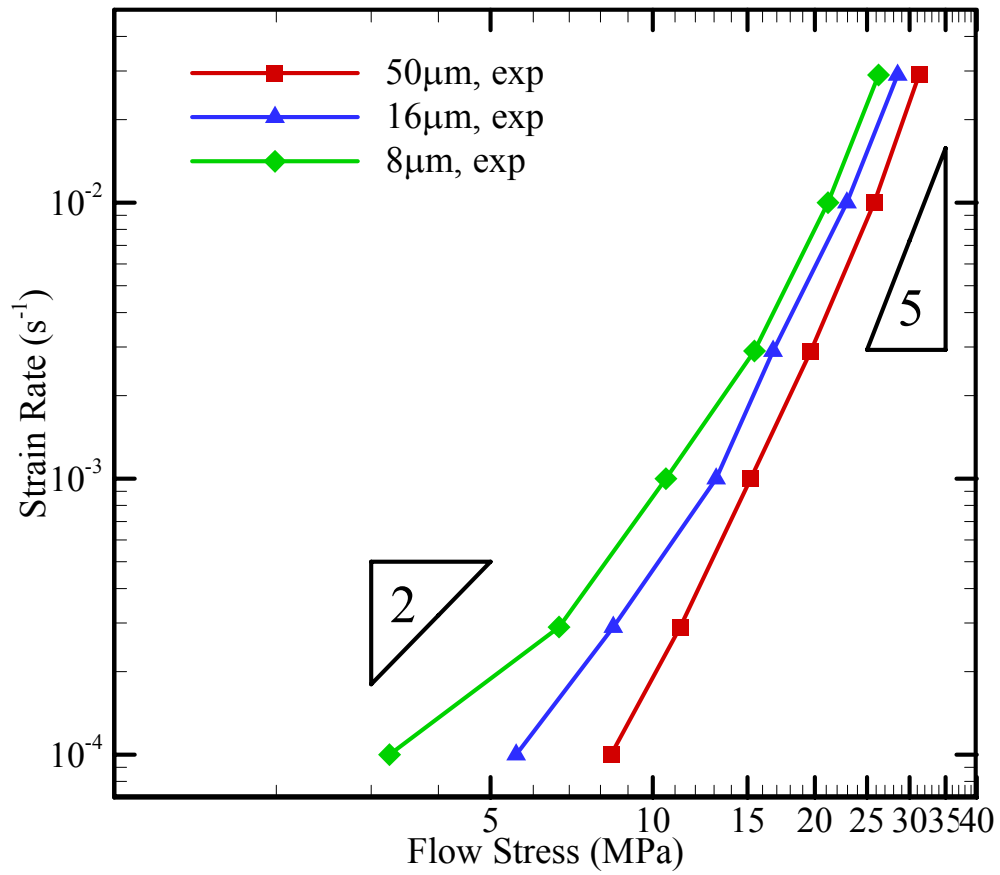


Figure 4.3: Experimentally produced strain rate vs. stress curves compiled from step strain rate tests at 450°C for the 8  $\mu m$ , 16  $\mu m$ , and 50  $\mu m$  material.



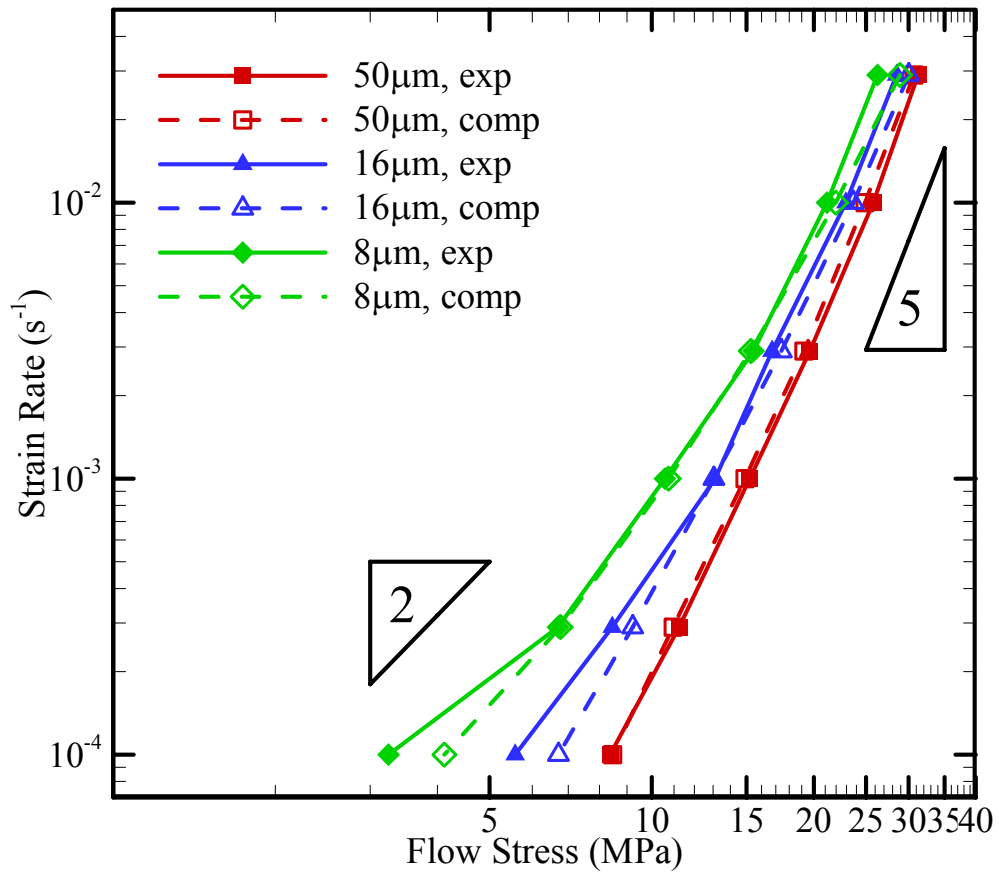


Figure 4.4: Computational and experimental strain rate vs. stress curves for the 8 $\mu m$ , 16 $\mu m$ , and 50 $\mu m$  material at 450°C. The simulation shows good fit to experiment.

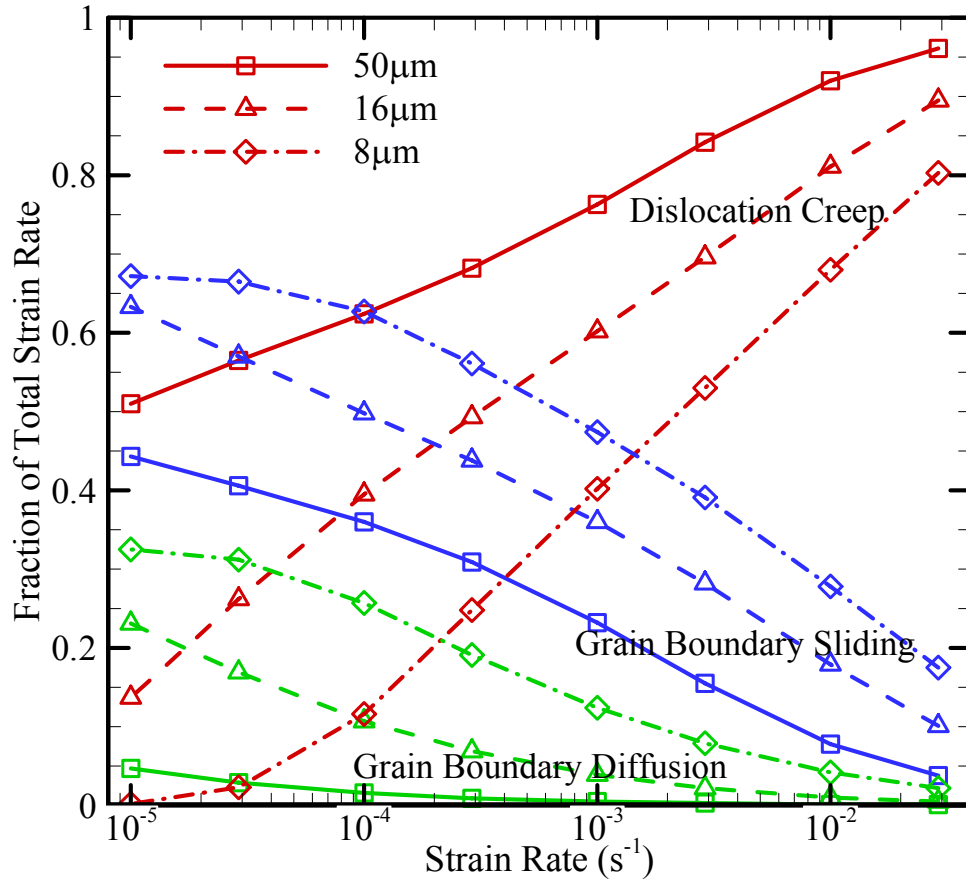


Figure 4.5: The predicted percent contribution to total strain rate from each deformation mechanism, DC, GBD, and GBS as a function of strain rate and average grain size at 450°C.

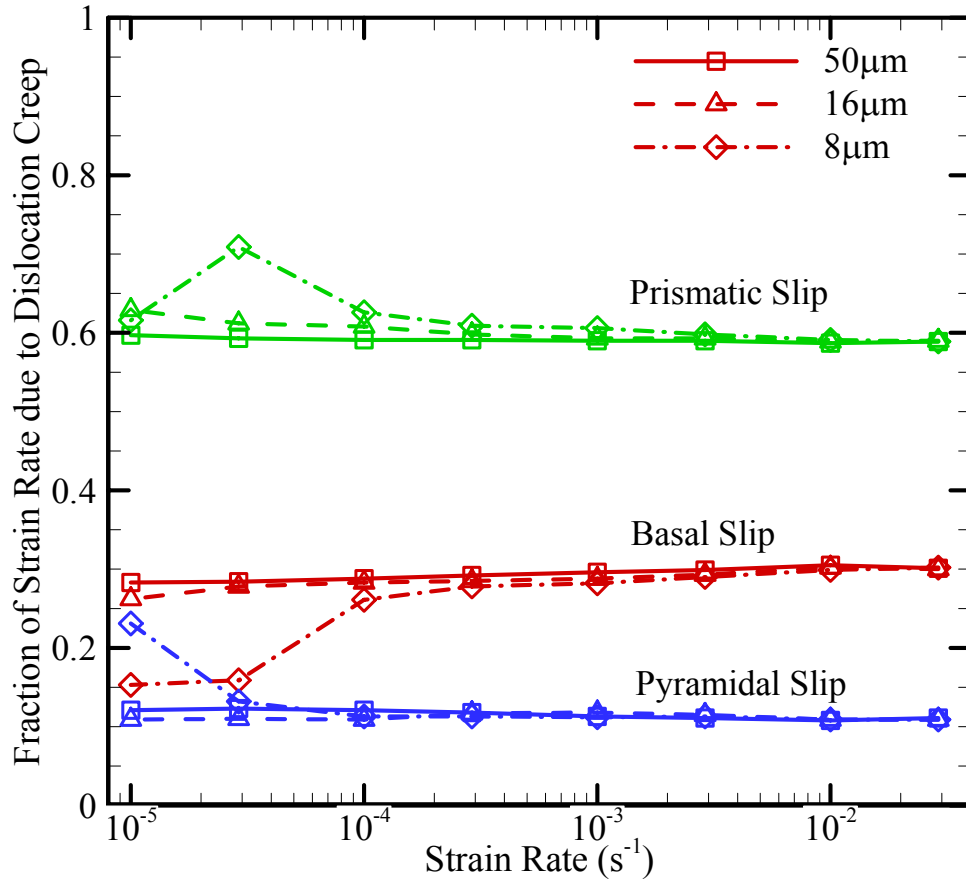


Figure 4.6: The predicted percent contribution to the total strain rate due to dislocation creep from slip on the basal, prismatic and pyramidal slip system in magnesium as a function of strain rate and average grain size at 450°C.

Table 4.1: Values for the material parameters used in the finite element simulations for magnesium alloy AZ31 (Barnett, 2003; Freund & Suresh, 2003; Frost & Ashby, 1982; Obara, Yoshinga, & Morozumi, 1973; Reed-Hill & Robertson, 1957; Ward Flynn, Mote, & Dorn, 1961; Yoo, Agnew, Morris, & Ho, 2001; Yoshinaga & Horiuchi, 1963).

Parameter	Value
Grain size $L$	$16\mu\text{ m}$
Atomic volume $\Omega$	$2.32 \times 10^{-29} \text{ m}^3$
Elastic constant, $c_{11}$	$59.7 \text{ GN m}^{-2}$
Elastic constant, $c_{33}$	$61.7 \text{ GN m}^{-2}$
Elastic constant, $c_{44}$	$16.4 \text{ GN m}^{-2}$
Elastic constant, $c_{12}$	$26.2 \text{ GN m}^{-2}$
Elastic constant, $c_{13}$	$21.7 \text{ GN m}^{-2}$
Characteristic strain rate $\dot{\gamma}_0$	$7.0 \times 10^{-3} \text{ s}^{-1}$
Initial yield stress, basal slip system $\tau_0$	$4 \text{ MN m}^{-2}$
Initial yield stress, prismatic slip system $\tau_0$	$10 \text{ MN m}^{-2}$
Initial yield stress, pyramidal slip system $\tau_0$	$11 \text{ MN m}^{-2}$
Solute drag creep stress exponent $n$	5.5
Grain boundary diffusion pre-exponential $\delta_{GB} D_{GBt}$	$4.74 \times 10^{-8} \text{ m}^3 \text{ s}^{-1}$
Grain boundary diffusion activation energy $Q_{GBt}$	$1.53 \times 10^{-19} \text{ J}$
Grain boundary sliding fluidity coefficient $\eta$	$3.65 \times 10^{-13} \text{ m}^3 \text{ MN}^{-1} \text{ s}^{-1}$

# **CHAPTER 5: APPLICATION OF THE MODEL TO STUDY PLASTIC ANISOTROPY IN MAGNESIUM ALLOY AZ31 EXTRUDED SHEET**

Magnesium alloys commonly display anisotropic behavior during deformation, which has generally been associated with the distinct texture that develops during plastic forming (Gehrmann, Frommert, & Gottstein, 2005). The influence of texture on deformation has been studied since an interest in magnesium alloys first started to develop a half century ago, however, its effect is not completely understood (Kelley & Hosford, 1968; Philippe, 1994). Texture has been studied in a wide variety of the hexagonal metals and has been shown to influence plastic deformation for a majority of them, including titanium, zinc, and zirconium (Ecob & Ralph, 1983; Lebensohn & Tome, 1993; Lee, C. Esling, & Bunge, 1988; Philippe, Beaujean, et al., 1994; Philippe, Bouzy, & Funderberger, 1998; Philippe, C. Esling, & Hocheid, 1988; Philippe, Serghat, Vanhoutte, & C Esling, 1995; Philippe, Wagner, Mellab, C Esling, & Wegria, 1994). Thus, the hcp atomic stacking structure is believed to play an important role. At room temperature plastic deformation is assumed to occur mostly by  $\langle a \rangle$  slip on the basal

plane or by  $\{10\bar{1}2\}\langle\bar{1}011\rangle$  twinning. The limited number of systems for plastic deformation cause low ductility, which is exacerbated by the parallel nature of the basal planes, and results in the development of a strong texture (Hutchinson, Barnett, Ghaderi, Cizek, & Sabirov, 2009). As temperature is increased  $\langle a \rangle$  slip on the prismatic plane becomes active as well as  $\langle c + a \rangle$  slip on the pyramidal plane (Reed-Hill & Robertson, 1957, 1958; Ward Flynn, Mote, & Dorn, 1961). The additional slip systems allow for cross slip to occur more easily, and along with the activation of additional deformation mechanisms, including GBS and GBD, significantly increase ductility. However, there is still debate on whether the increase in ductility is due to the activation of additional slip systems or the additional deformation mechanisms (Agnew & Duygulu, 2005)). Specifically, the importance of  $\langle c + a \rangle$  slip to increase ductility during elevated temperature deformation is discussed in the work of Hutchinson (Hutchinson et al., 2009).

Although the hcp stacking structure of magnesium may be responsible for the development of texture during forming, it also serves to aid in analysis to determine the root of the increased ductility in magnesium AZ31 sheet at elevated temperatures. When the sheet is formed the basal planes tend to become aligned creating a strong basal texture in the extruded direction. This is observed in the pole figures of the sample oriented so that the tensile axis is parallel to the extruded direction (figure 2.6). When a strain rate is applied, the resolved shear stress on the various slip systems is similar for most grains because they are all oriented in a similar manner. Thus, investigating the deformation mechanisms for different orientations can be instrumental in determining the underlying

causes of increased ductility. The model is uniquely poised for this analysis because the fraction of strain rate from each deformation mechanism and each slip system can be parsed from the total strain rate induced in the microstructure.

With this in mind, the finite element model that was validated in chapter 4 for magnesium alloy AZ31 was applied to the extruded magnesium AZ31 sheet material that was investigated in chapter 2.

## **5.1 Application of the Model to Extruded Magnesium AZ31 Sheet Deformed at 450°C**

First the model was applied to study deformation in magnesium AZ31 extruded sheet deformed at 450°C, the temperature of the QPF process in aluminum alloy 5083. From an experimental perspective it was shown that magnesium alloy AZ31 extruded sheet exhibits anisotropic behavior during tensile tests at elevated temperatures in multiple ways. The ductility increased when the loading direction was oriented perpendicular to the extruded direction, and the yield strength was increased when the loading direction was oriented parallel to the extruded direction. The strain rate sensitivity transitioned from 0.2 at high strain rates for both orientations to a value at low strain rates of about 0.3 for the specimens loaded parallel to the extruded direction and approximately 0.5 for the specimens loaded perpendicular to the extruded direction. This transition suggested a change in the prevalent deformation mechanism from dislocation creep at high strain rates to grain boundary sliding at low strain rates; the transition was more pronounced for the perpendicular oriented specimen. Necking was shown to occur

primarily on the opposite faces of the two specimens. By examination of the microstructure of the specimens from each orientation, a possible basis for the anisotropy was uncovered. Due to the extrusion process a strong texture developed in the sheet. Thus, for the specimens oriented with the extruded direction parallel to the tensile axis, the grains were aligned with the basal plane along the tensile direction (the c-axis and tensile axis were perpendicular) and the apparent grain size was equal to  $18\mu\text{m}$ . Whereas for the specimen with the extruded direction perpendicular to the tensile axis, the grains were aligned so that the  $\langle 10\bar{1}0 \rangle$  and  $\langle 11\bar{2}0 \rangle$  directions were perpendicular to the tensile direction (the c-axis and tensile axis were parallel) and the apparent grain size was equal to  $9\mu\text{m}$ . In an effort to further understand the results of the experimental work and the mechanisms involved in elevated temperature deformation, the finite element model has been employed to explore the anisotropic behavior of the extruded magnesium AZ31 sheet material.

### **5.1.1 Setup of Initial Conditions**

The material parameters listed in table 4.1 that were validated using the process described in the section 4.1 to predict the deformation response of AZ31 sheet at elevated temperature were not adjusted to model the extruded sheet, because there was no change in the alloy. However, due to the orientation of the tensile specimens, changes were necessary in the simulation microstructure. As seen in figure 2.5 and 2.6, the microstructure of the tensile specimens oriented with the extrusion direction parallel to the tensile axis was shown to have a grain size of approximately  $18\mu\text{m}$  and its grains were



shown to be strongly oriented in the basal direction. Thus, the simulation micrograph that was used in the validation section was utilized in this case as well, with the scaling technique used to correct the grain size. The microstructure of the tensile specimens oriented with the extrusion direction perpendicular to the tensile axis were shown to have a grain size of approximately  $9\mu\text{m}$  and its grains were aligned perpendicular to the basal plane (figure 2.5 and 2.7). For this case a second simulation micrograph was developed using the same method as described in section 4.1. The EBSD data for the microstructure of the tensile specimen  $90^\circ$  to the extruded direction is shown in figure 5.1 alongside the corresponding simulation microstructure. The grain shape and orientation show close correlation between the two micrographs (again the orientation data is not shown on the simulation micrograph but it corresponds directly to the EBSD data). Thus, the only changes to prepare the model for this study were to adjust the initial grain size and the initial microstructure based on the observations of the actual microstructure prior to testing.

### **5.1.2 Comparison of Computational and Experimental Results**

By only changing the initial microstructure input to the model, the finite element predictions show good agreement with the experimental curves of flow stress vs. strain rate for when the tensile axis is oriented  $0^\circ$  and  $90^\circ$  to the extrusion direction as shown in figure 5.2. In the high strain rate regime the stress exponent,  $n$ , approaches 5 for each curve (strain rate sensitivity equals 0.2), which suggests that dislocation creep is the dominant deformation mechanism in this range of strain rate. From the high strain rate

regime to the low strain rate regime the curves for each orientation show a transition in the stress exponent, which is captured by the computational model. The stress exponent decreases to approximately 2 in the low strain rate regime, which is considered to be indicative of deformation by grain boundary sliding. Within this range of strain rates, there is a greater discrepancy between the two orientations. The change in stress exponent is greater for the data from the sample oriented  $90^\circ$  to the extruded direction, and furthermore the flow stress extends to smaller values, suggesting that grain boundary sliding is more prevalent for this orientation. This variance is accurately captured by the model, which also shows a greater transition in the stress exponent for the sample oriented  $90^\circ$  to the extruded direction.

### **5.1.3 Distribution of Strain Rate by Deformation Mechanism**

If as before, the strain rate induced on the simulation microstructure is separated into the contribution from each deformation mechanism to the total strain rate by the finite element model and plotted as a function of strain rate, the distribution shown in figure 5.3 is produced. This allows for the direct interpretation of the model's prediction of the relevance of each deformation mechanism across the range of strain rates tested, and the transition of the dominant deformation mechanism that was observed in figure 2.17 as a change in the stress exponent, and in figure 2.18 as a transition in the strain rate sensitivity, becomes readily apparent. In general for each orientation, at slower strain rates the greatest contribution to the total strain rate is grain boundary sliding, while at faster strain rates dislocation creep emerges as the dominate deformation mechanism. The

simulation for the material oriented  $90^\circ$  to the ED shows more grain boundary sliding as a percentage of total strain rate than the  $0^\circ$  to the ED data at all strain rates, and correspondingly a smaller amount of dislocation creep across the range of strain rates tested. Thus, changing the loading direction from parallel to perpendicular to the ED drives the transition point of the dominant deformation mechanism from grain boundary sliding to dislocation creep to occur at higher strain rates. This corresponds to the transition in the strain rate sensitivity that occurred between the high and low strain rate regimes to a greater extent when the loading axis was  $90^\circ$  to the ED.

It is advantageous to plot the model's prediction of the contribution from each slip system to the total dislocation creep in the simulation, because of its significance for magnesium alloys where the geometry and strength of the each slip systems varies. Figure 5.4 plots the fraction of dislocation creep that occurs on each slip system as a function of strain rate. It should be noted that the strain rate on each system is normalized by total plastic strain rate due to plastic shearing within the grains, which is significantly smaller than the total strain rate at low strain rates. When the loading is parallel to the ED, slip on the prismatic system is dominant followed by the basal and pyramidal system respectively for the entire range of strain rates as observed in the previous work when the same initial microstructure was employed. However, when loading is  $90^\circ$  to the ED, slip on the basal system is dominant followed by slip on the prismatic and pyramidal, which each contribute approximately equal amounts to the total slip. At low strain rates for the sample oriented  $90^\circ$  to the ED there is a transition of basal dominated slip with slip on the prismatic and pyramidal planes. However, at these low strain rates there are small amounts of dislocation creep in the microstructure and the flow stress is decreased. In

conclusion, the substantial difference in the initial orientation of the two starting microstructures with respect to the tensile axis has an effect on the relative amount of sliding on each slip system for the two orientations.

#### **5.1.4 Comparison of Grain Size and Orientation**

In order to isolate the effect on grain size and texture on deformation two additional simulations were run where the orientation and grain size of the microstructure were swapped. The grain size of the sample oriented  $0^\circ$  to the ED was measured as  $18\mu\text{m}$  and the grain size of the sample oriented  $90^\circ$  to the ED was measured as  $9\mu\text{m}$ . Thus, simulations were run with the orientation of the sample oriented  $0^\circ$  to the ED and a  $9\mu\text{m}$  grain size, as well as for the orientation of the sample loaded  $90^\circ$  to the ED and an  $18\mu\text{m}$  grain size. The results of the strain rate vs. stress curves for these additional simulations along with the original results from the simulations with the correctly combined microstructure characteristics are plotted in figure 5.5. The flow curves with the same grain size show strong correlation whereas the curves with the same orientation with respect to the extruded direction show weak correlation. This suggests that the grain size of the material has a greater effect than the orientation on the flow stress as a function of strain rate. However, the orientation of the tensile axis has a significant effect on the distribution of slip due to dislocation creep, which is plotted against strain rate in figure 5.6. The contribution to dislocation creep from each slip system is based strongly on orientation and there is little effect of grain size.

If the contribution to the total strain rate from each deformation mechanism is

plotted against strain rate for the four simulations as shown in figure 5.7 and 5.8, the curves with equal grain size are closer in proximity to each other. However, there is a change between the different orientations at each grain size. For both grain sizes, but to a greater extent for the larger grain size, there is a greater contribution of strain rate due to dislocation creep for the sample oriented  $0^\circ$  to the ED. As was discussed in chapter 4, it is expected that the greater grain size material will have a greater contribution from dislocation creep. Thus a change in the orientation, which affects the distribution of slip on the various systems, would most likely have a greater effect when dislocation creep is more prevalent. This is observed for the larger grain sized material, but this is also applicable in general to the dislocation creep regime. At high strain rates where the contribution to grain boundary sliding is decreased, anisotropic behavior is more dependent on orientation than grain size. However, there is less of an anisotropic effect on the flow curves at the high strain rates as observed in the plot of strain rate vs. stress.

For both grain sizes, grain boundary sliding is greater for the sample oriented  $90^\circ$  to the ED. This is partly due to the greater contribution of dislocation creep in the sample oriented  $0^\circ$  to the ED, but for the comparison at the  $9\mu\text{m}$  grain size, the increase in GBS is greater than the decrease in DC for a change in orientation. This suggests that GBS is more likely for loading oriented  $90^\circ$  to the ED, which may be due to the more even distribution of slip on the various systems for this orientation, which would promote a more even distribution of stress, allowing for greater sliding. Thus, the orientation does have an effect on the response of the microstructure to deformation; however, the root of the anisotropy is a result of the difference in the effective grain size rather than orientation.

### 5.1.5 Conclusions from Deformation at 450°C

In an attempt to understand what was uncovered during the experimental investigation at temperature typical of the QPF process, the finite element model was employed to further investigate the anisotropic characteristics of the microstructure and their effect on the anisotropic results of the tensile tests. The model was able to capture the differences between the specimens oriented parallel and perpendicular to the ED with good agreement to the experimental results. By plotting the distribution of the strain rate for each deformation mechanism it was shown that, as was surmised from observations of the strain rate vs. stress curves, the sample loaded 90° to the ED transitioned from dislocation creep as the dominant deformation mechanism to grain boundary sliding at a faster strain rate than for the sample loaded 0° to the ED. For the sample loaded 90° to the ED this transition occurred at approximately  $2.0 \times 10^{-3} s^{-1}$ , whereas for the sample oriented 0° to the ED it occurred at approximately  $1.5 \times 10^{-4} s^{-1}$ .

The opposing texture of each orientation had a significant effect on the distribution of dislocation creep in the microstructure. When the loading was 0° to the ED, slip on the prismatic system was clearly dominant accounting for 60 percent of deformation due to dislocation creep. However, when the loading was 90° to the ED, slip on the basal system most prevalent, accounting for about 45 percent of the total strain rate due to dislocation creep at a strain rate of  $10^{-2} s^{-1}$  which lies in the regime where dislocation creep is the dominant deformation mechanism. There was a much more even distribution of slip for this orientation, where the pyramidal system and prismatic system

accounted for approximately 25 and 30 percent of the total strain rate due to dislocation creep respectively.

To isolate the effect of grain size and orientation in the simulation of the constitutive response of the extruded sheet, these two characteristics were switched in the simulation microstructure. By comparing the results of the simulations based on the actual micrographs with the simulations based on the fabricated microstructures, it was determined that although the orientation of the tensile axis strongly effected the distribution of slip on the various slip systems, it had only a small effect on the flow curves and the contribution of each deformation mechanism. The grain size was shown to have a much larger effect.

## **5.2 Application of the Model to a Change in Temperature in AZ31**

### **Extruded Sheet**

The model has also been shown to account for changes in temperature as long as testing remains at temperature values where the assumptions made for elevated temperature deformation are still valid. The temperature cannot be reduced to a point where twinning becomes integral to deformation or to where the critical resolved shear stress on the prismatic and pyramidal slip systems has increased substantially over that of the basal slip system.

#### **5.2.1 Comparison of the Model with Experiment**

In chapter 2 the effect of temperature on the strain rate as a function of flow stress was discussed for the magnesium AZ31 extruded sheet material. It was demonstrated that when the testing temperature was decreased from 450°C to 350°C, the flow stress increased over the range of strain rates tested. The stress exponent was equal to approximately 5 at fast strain rates for both testing temperatures, but for the 450°C tests the stress exponent decreased more substantially for both orientations. This suggested that grain boundary sliding is more prevalent at higher temperatures. In an attempt to further investigate the effect of temperature in magnesium alloy AZ31, the computational approach has been employed to model these experimental results.

To do so, three of the model parameters need to be adjusted based on the decrease in temperature from 450°C to 350°C. First, the grain boundary diffusion pre-exponential parameter was adjusted to account for the change in temperature using a ratio of boundary diffusion in magnesium calculated at 450°C and 350°C using the values from Frost and Ashby (Frost & Ashby, 1982). This adjustment of the diffusion pre-exponential will lead to a decrease in GBD. Although this ratio was constructed using Frost and Ashby's values for diffusion, the same ratio was used to adjust the grain boundary sliding fluidity parameter. Based on the literature, it is difficult to determine quantitatively how much sliding will be affected by a decrease in temperature. Thus, it was assumed that grain boundary sliding and diffusion will both decrease by similar amounts. Third, the characteristic strain rate parameter was decreased to fit the experimental data to account for the increase in the critical resolved shear stress on each slip system due to the decrease in temperature. The ratio between the slip systems was not changed.

First the model was applied to predict deformation for loading parallel to the ED.



Thus the same starting microstructure that was previously used for simulating deformation in the specimen oriented  $0^\circ$  to the ED was utilized again here. As can be observed in figure 5.9, the computational results are shown to compare well with experiment at  $350^\circ\text{C}$ . Due to a decrease in temperature there is increased resistance to GBS and GBD, and a greater CRSS on each slip system. All of which leads to a greater flow stress in response to an induced strain rate.

To validate the predictions for deformation at  $350^\circ\text{C}$  with the aforementioned parameters adjusted for the change in temperature, the model was applied to the specimen oriented  $90^\circ$  to the ED. In this case the only change was to use the simulation microstructure constructed for use with the appropriately oriented specimen. The comparison of experimental and computational results for the strain rate plotted as a function of stress for deformation at  $350^\circ\text{C}$  and  $450^\circ\text{C}$  for loading perpendicular to the ED is shown in figure 5.10. As in the case for loading parallel to the ED, the experimental curves are closely predicted by the model.

### **5.2.2 Distribution of Strain Rate by Deformation Mechanism**

Although there is increased resistance for each deformation mechanism dislocation creep is shown to be more dominant across the range of strain rates for the lower temperature tests for each orientation. As shown in figure 5.11 and 5.12, the decrease in temperature led to an increase in the amount of plasticity due to dislocation creep and a decrease in the amount of grain boundary sliding and grain boundary diffusion relative to the total strain rate in the microstructure. The transition point

between deformation dominated by dislocation creep and deformation due to grain boundary sliding migrated to slower strain rates. The strain rate of the transition point decreased one order of magnitude for the decrease in temperature of 100°C. For the specimen oriented 0° to the ED, the transition point decreased from  $1.5 \times 10^{-4} s^{-1}$  at 450°C to  $1.5 \times 10^{-5} s^{-1}$  at 350°C, and for the specimen oriented 90° to the ED the transition point migrated from  $2.0 \times 10^{-3} s^{-1}$  at 450°C to  $2.3 \times 10^{-4} s^{-1}$  at 350°C.

The deformation due to dislocation creep is investigated by parsing the contribution from each slip system as shown in figure 5.13 for loading parallel to the ED and in figure 5.14 for loading perpendicular to the ED. Although the flow stress increased substantially in the microstructure during the simulation at 350°C there was little change in the distribution of slip from the test at 450°C. For the sample oriented 0° to the ED, slip on the prismatic system remained dominant followed by slip on the basal and pyramidal slip systems respectively. Similarly, for the sample oriented 90° to the ED, the basal plane remained the most prevalent for slip followed by the pyramidal and prismatic plane respectively. These results are not entirely unexpected due to the fact that the ratio between the slip systems was unchanged, and for each orientation there was no change in the starting microstructure for the simulations at 350°C and 450°C.

### **5.2.3 Conclusions from Application of the Model to Temperature**

It has been demonstrated that the polycrystal crystal plasticity model that was shown to correctly predict the flow stress and deformation mechanisms in magnesium AZ31 alloy deformed at 450°C can also account for variation in temperature to 350°C.

The predicted influence of temperature on the flow stress was found to be in excellent agreement with experimental measurements. As temperature is decreased from 450°C to 350°C the model aptly predicts that the transition in the dominant deformation mechanism from dislocation creep to grain boundary sliding will shift to lower strain rates. The strain rate of the transition point decreased one order of magnitude for the decrease in temperature of 100°C for both orientations. There was no change in the model prediction of distribution of dislocation creep on the various slip systems due to a change in temperature.

### **5.3 Discussion**

As mentioned in the introduction to this chapter, there has been extensive work on textured magnesium. The results of these studies are worth discussing to compare to the results presented here. Gehrman et al. focused on the effect of texture during compression tests from 100°C to 200°C, thus the boundary conditions are different than those considered here (Gehrman et al., 2005). They determined that when basal slip was suppressed due to orientation of the basal planes parallel to the compression direction, large fracture strains were made possible by significant slip on the prismatic system that was activated as low as 100°C. In the work presented here for the sample oriented so that the tensile axis is parallel to the ED, as seen in the texture map in figure 2.6, the basal planes are also parallel to the tensile axis. Due to their orientation, slip on the basal planes is suppressed for a majority of the grains, and thus as seen in figure 5.3, dislocation creep is accommodated by slip on the prismatic system.

Using a combination of experimental and computational techniques, Agnew and Duygulu performed a comprehensive study of deformation in magnesium AZ31 from room temperature to 250°C and strain rates of  $10^{-5}\text{s}^{-1}$  to  $0.1\text{s}^{-1}$  (Agnew & Duygulu, 2005). They concentrated on the effect of strain hardening, strain rate sensitivity, anisotropy, and the stress and strain at fracture. In conclusion they found that the most important factor to increase formability, at temperatures on the high end of the range they investigated, was an increase in the strain rate sensitivity. This conclusion supports the results of the present work where it was shown that the material oriented such that the tensile axis was  $90^\circ$  to the ED exhibited greater strain rate sensitivity, figure 2.19, and also exhibited greater ductility, figure 2.16.

However, Agnew and Duygulu reason that an increase in the activity of the  $\langle c+a \rangle$  slip system, which is activated at elevated temperatures, is what leads to the increase in strain rate sensitivity (Agnew & Duygulu, 2005). However, the work of Hutchinson et al. comes to a different conclusion than that of Agnew and Duygulu. Their work used a similar material and experimental procedure to Agnew and Duygulu with additional analysis using optical and transmission electron microscopy to specifically look at the contribution of  $\langle c+a \rangle$  dislocations (Hutchinson et al., 2009). They observed multiple grains after deformation at elevated temperatures and found that two-thirds of those observed did not contain  $\langle c+a \rangle$  dislocations. Thus, they concluded that although slip on the pyramidal system is important to increasing the strain rate sensitivity, and thus increasing ductility, it cannot be the only factor. Their results suggested that increased ductility is more dependent on an increase in grain boundary sliding in the material, which is in turn dependent on the grain size of the material (Hutchinson et al., 2009).

This conclusion is supported by the work presented here, which shows that GBS is significant to increasing the strain rate sensitivity (decreasing the stress exponent) and that GBS is strongly influenced by the grain size of the material. The contribution from GBS increases for smaller grain size. Furthermore, pyramidal slip is shown to be influential but not dominant. The contribution of slip on the pyramidal plane is significant and is shown to be greater for the specimen loaded  $90^\circ$  to the ED, which is the specimen that also shows greater strain rate sensitivity at low strain rates and greater ductility overall.

It is worth reconsidering the stress vs. strain plot for the extruded magnesium AZ31 sheet, now that more is known about the deformation mechanisms (figure 2.16). The yield stress is greater for the specimens loaded  $0^\circ$  to the ED than for the specimens oriented with the tensile axis  $90^\circ$  to the ED. This is likely a result of the dominant slip system for each orientation. As shown in figure 5.4, with the tensile axis oriented  $0^\circ$  to the ED, the prismatic slip systems is dominant whereas for the  $90^\circ$  to the ED orientation, basal slip is dominant. Basal slip has a smaller CRSS than the prismatic slip system which allows for the smaller yield stress for the sample oriented  $90^\circ$  to the ED.

The difference in the hardening and softening of the curves can be explained by the onset of deformation dominated by GBS. The behavior of the sample oriented  $90^\circ$  to the ED, strained at  $0.001s^{-1}$  shows hardening followed by softening, suggesting that the grains rotate during the hardening stage to align themselves for decreased resistance to slip which then allows softening to occur. This grain rotation is aided by the grain boundary sliding mechanism, which as shown in figure 5.3, is the dominant deformation mechanism for this strain rate and orientation. The other three stress vs. strain curves (for

the  $0^\circ$  to ED orientation at a strain rate of  $0.001s^{-1}$  and both orientations at a strain rate of  $0.1s^{-1}$ ), do not show an extended hardening regime, but rather exhibit softening after yield. The testing conditions for these three specimens lie firmly within the range where dislocation creep is dominant.

## 5.4 Conclusions of the Anisotropy Study

In conclusion, the microstructure based continuum finite element model that was validated in chapter 4 has been successfully applied to predict the deformation behavior of extruded magnesium AZ31 sheet at  $350^\circ\text{C}$  and  $450^\circ\text{C}$ . The model accounts for the change in grain size and microstructure inherent to the specimens when the loading direction was oriented parallel and perpendicular to the extruded direction. The change in these two characteristics was observed as the two major differences in the microstructure that led to significant changes in the results of the tensile tests. The results of the model led the following observations about the deformation behavior at elevated temperature for extruded AZ31 sheet tested with the tensile axis  $0^\circ$  or  $90^\circ$  to the ED:

1. At  $450^\circ\text{C}$ , the critical strain rate where the dominant deformation mechanism transitions from dislocation creep to grain boundary sliding shifts from  $1.5 \times 10^{-4} s^{-1}$  when the tensile axis is  $0^\circ$  to the ED to  $2.0 \times 10^{-3} s^{-1}$  when the tensile axis is  $90^\circ$  to the ED.
2. At  $350^\circ\text{C}$ , the critical strain rate where the dominant deformation mechanism transitions from dislocation creep to grain boundary sliding shifts from

$1.5 \times 10^{-5} s^{-1}$  when the tensile axis is  $0^\circ$  to the ED to  $2.3 \times 10^{-4} s^{-1}$  when the tensile axis is  $90^\circ$  to the ED.

3. For both orientations the critical strain rate decreased one order of magnitude when the testing temperature decreased  $100^\circ\text{C}$ .
4. For deformation with the tensile axis  $0^\circ$  to the ED, slip on the prismatic system is dominant followed by slip on the basal and pyramidal system respectively.
5. For deformation with the tensile axis  $90^\circ$  to the ED, slip on the basal system is dominant followed by slip on the pyramidal and prismatic system respectively.
6. The contribution of each slip system to the total strain rate due to dislocation creep is not dependent on strain rate or temperature.

These conclusions led to the following analysis in response to recent work on the effect of anisotropy in textured magnesium AZ31 sheet.

The work of Agnew and Duygulu, and separately of Hutchinson, suggest that strain rate sensitivity is critical to increasing ductility in magnesium alloy AZ31. Agnew and Duygulu suggest this is due to slip on the pyramidal system, whereas Hutchinson suggests that although this is true, to a greater extent it is a function of increased grain boundary sliding (Agnew & Duygulu, 2005; Hutchinson et al., 2009). The work presented here reaches similar conclusions to the work of Hutchinson. The model demonstrated that a transition from dislocation creep to grain boundary sliding led to a rise in the strain rate sensitivity from 0.2 to 0.5 from fast to slow strain rates. If each orientation is considered separately, there is no transition in the distribution of dislocation creep on the various slip systems due to a change in strain rate or furthermore to a change

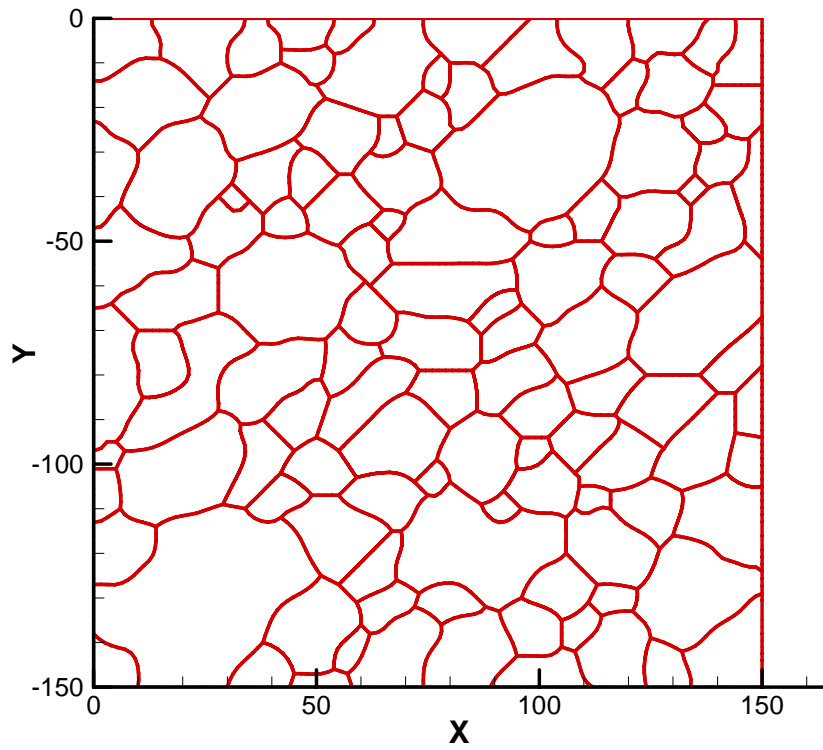
in temperature. However, due to the advantage of the anisotropy of the extruded material the change in orientation is influential and should be considered. During loading  $90^\circ$  to the ED there is a more prominent transition from dislocation creep dominated flow to grain boundary sliding, and this transition occurs at a higher strain rate. This could be a direct effect of the decrease in the apparent grain size at this orientation, which decreases from  $18\mu\text{m}$  when the loading is  $0^\circ$  to the ED to  $9\mu\text{m}$  when the loading is  $90^\circ$  to the ED. Or it could be due to the difference in the distribution of dislocation creep on the various slip systems, which specifically includes an increase in the amount of pyramidal slip during loading  $90^\circ$  to the ED.

By isolating the effects of grain size and orientation in the comparison study, it was determined that grain size as a stronger effect compared to the orientation of the grains with respect to the tensile axis. This conclusion is reinforced by the results of chapter 4, where it was determined that a decrease in grain size leads to an increase in the grain boundary sliding. The difference in the apparent grain size has a significant effect on the transition to grain boundary sliding and thus the transition to higher strain rate sensitivity. There is an additional effect of the orientation of the grains, which effects the distribution of dislocation creep and is responsible for anisotropy in the dislocation creep regime where the effect of grain boundary sliding is diminished. There is even an effect of orientation on the grain boundary sliding mechanism. However, the apparent grain size is the dominant effect on movement of the transition point.

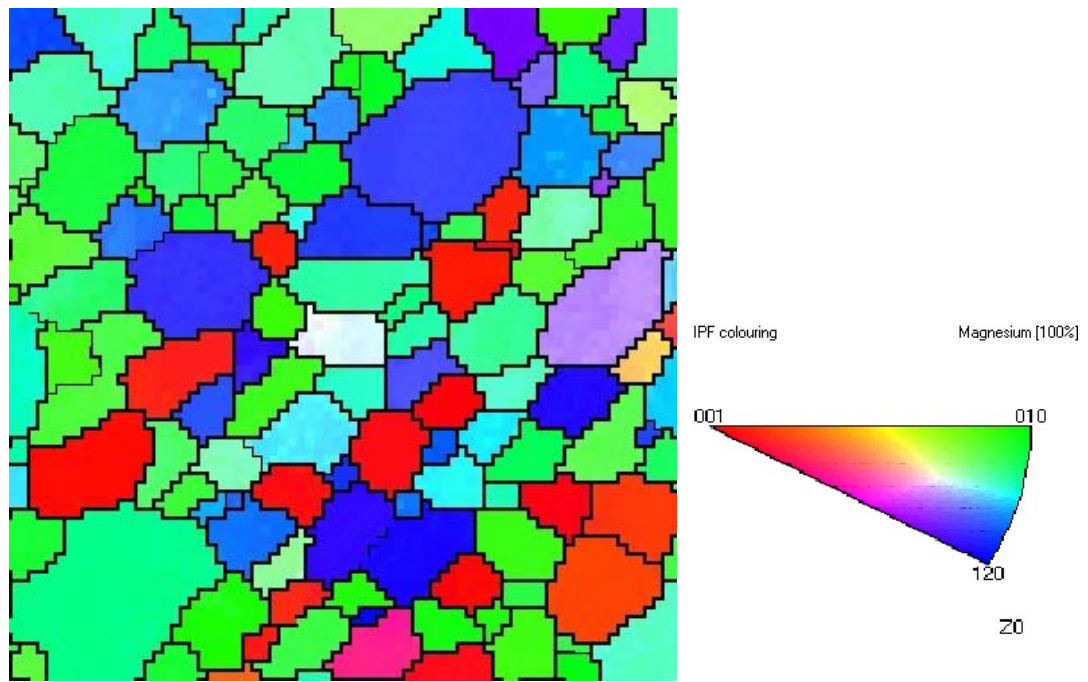
Thus, due to a smaller apparent grain size and more ideal grain orientation with respect to the tensile axis, the specimen oriented  $90^\circ$  to the ED contained a greater contribution from grain boundary sliding to the total strain rate in the solid. Thus the



specimen transitioned from the dislocation creep regime to grain boundary sliding regime at greater strain rates and displayed greater strain rate sensitivity. Furthermore, the specimen oriented  $90^\circ$  to the ED showed greater ductility than the specimen oriented  $0^\circ$  to the ED. Thus, this suggests that ductility in magnesium AZ31 increases for this orientation due to the decrease in grain size and preferential grain orientation which leads to a greater contribution from grain boundary sliding.



a



b

Figure 5.1: Comparison of the simulation microstructure (a) and the experimentally obtained microstructure using EBSD (b) for the specimen oriented  $90^\circ$  to the ED. The tensile direction is horizontally to the right.

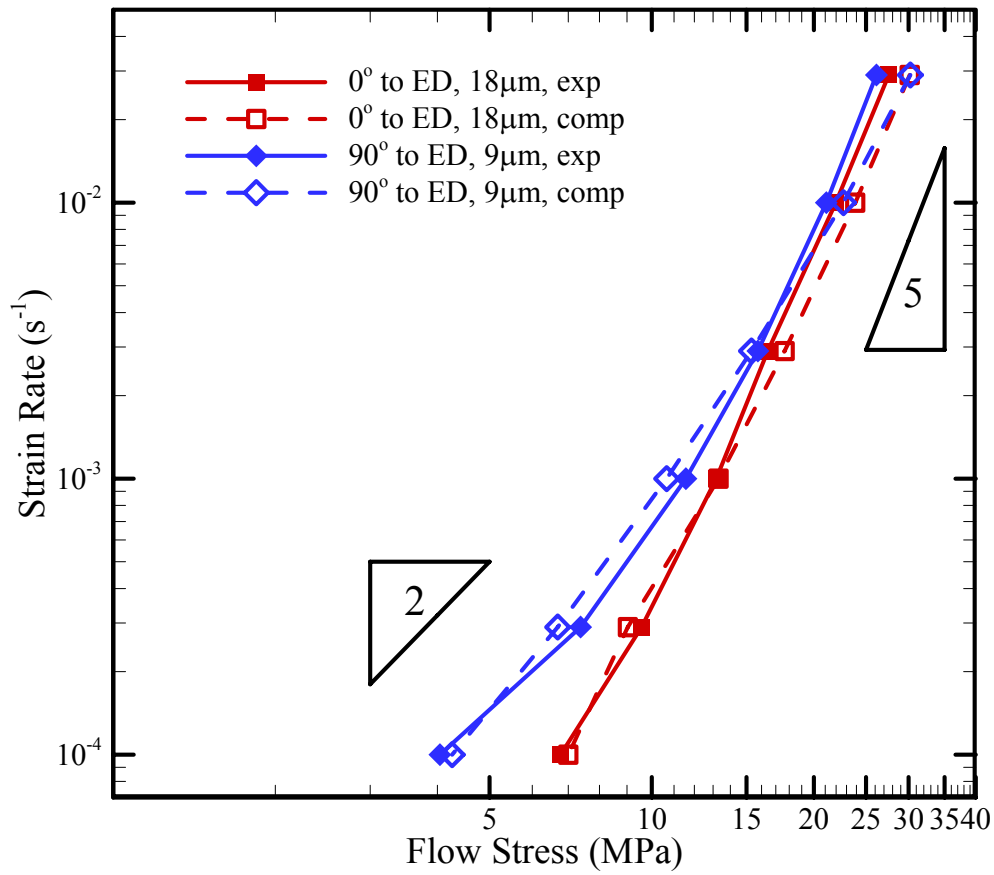


Figure 5.2: Computational and experimental flow stress curves for the AZ31 extruded sheet material tested at  $450^\circ C$  for the tensile axis rotated  $0^\circ$  or  $90^\circ$  from the extrusion direction. The simulation shows good fit to experiment.

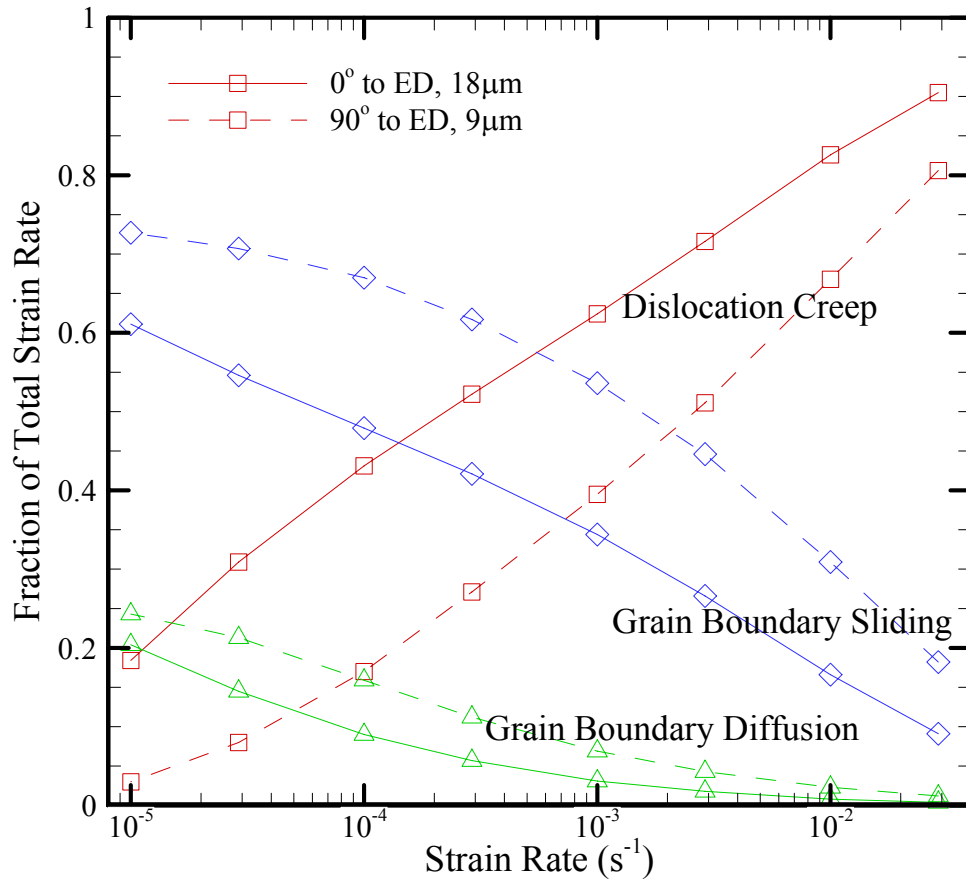


Figure 5.3: The predicted percent contribution to total strain rate from each deformation mechanism, DC, GBD, and GBS as a function of strain rate and orientation of the tensile axis at 450°C.

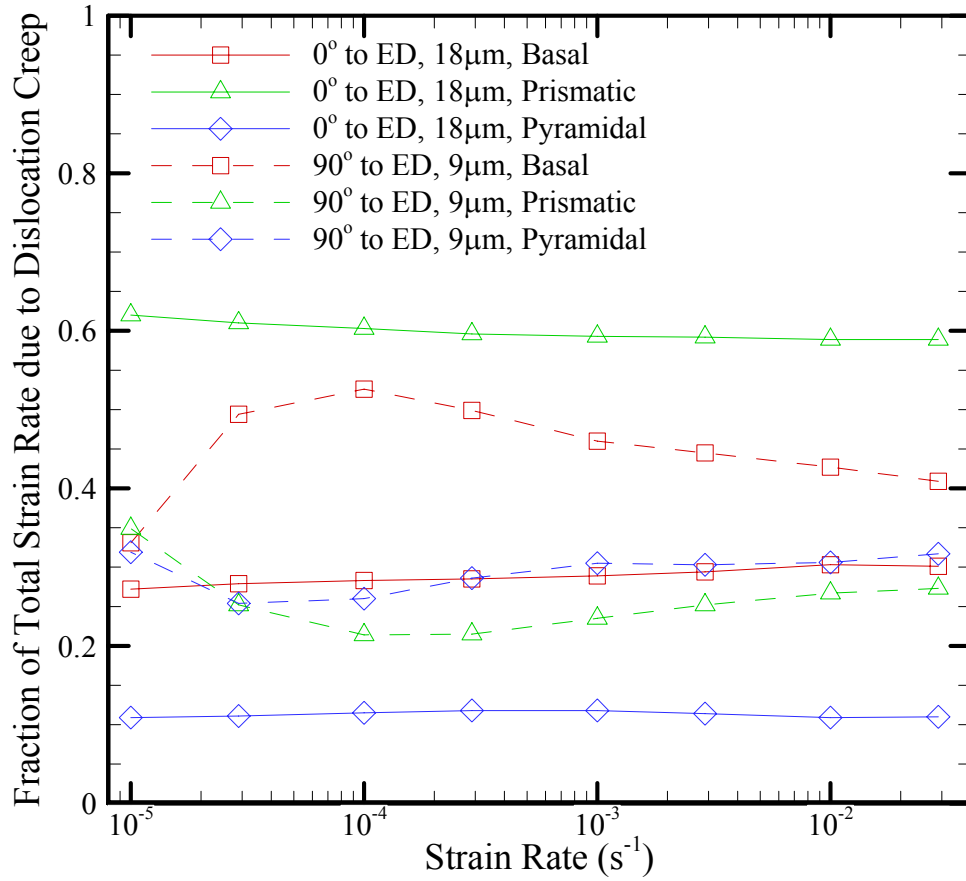


Figure 5.4: The predicted percent contribution to the total strain rate due to dislocation creep from slip on the basal, prismatic and pyramidal slip system in magnesium as a function of strain rate and orientation of the tensile axis at 450°C.

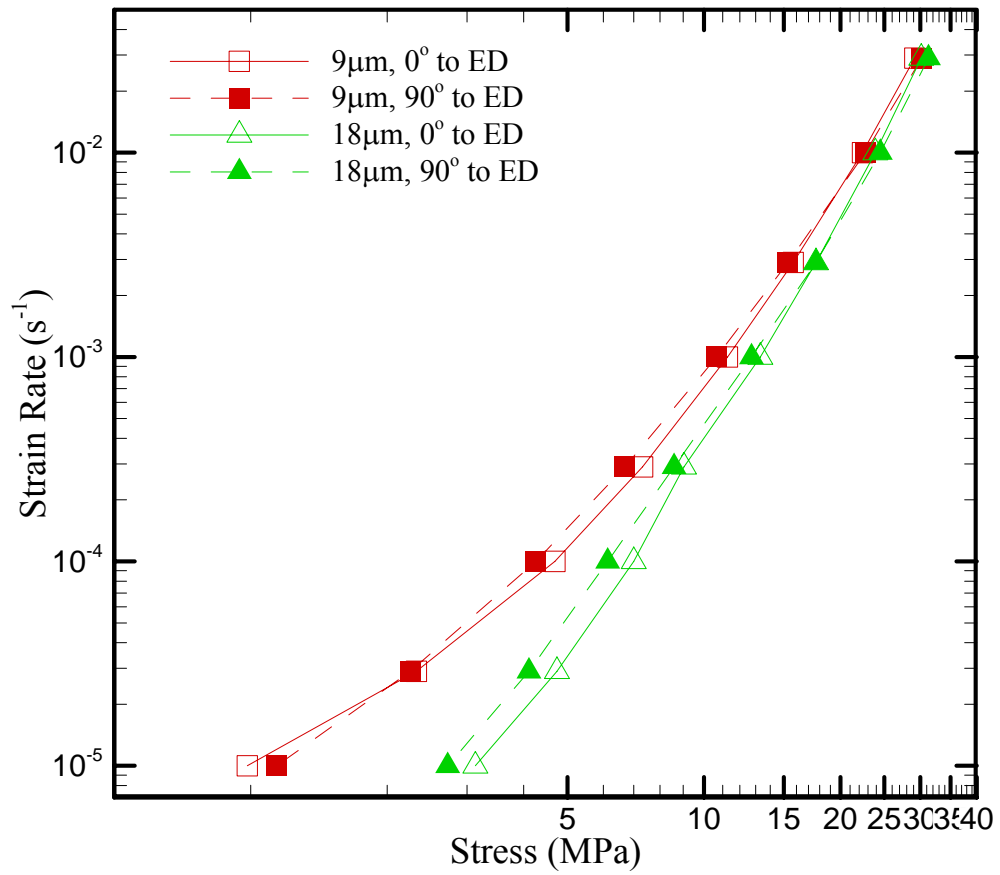


Figure 5.5: Computational flow curves for the simulations based on the actual micrographs of the differently oriented extruded magnesium AZ31 sheet and the fabricated simulations with alternate grain size and orientation at 450°C.

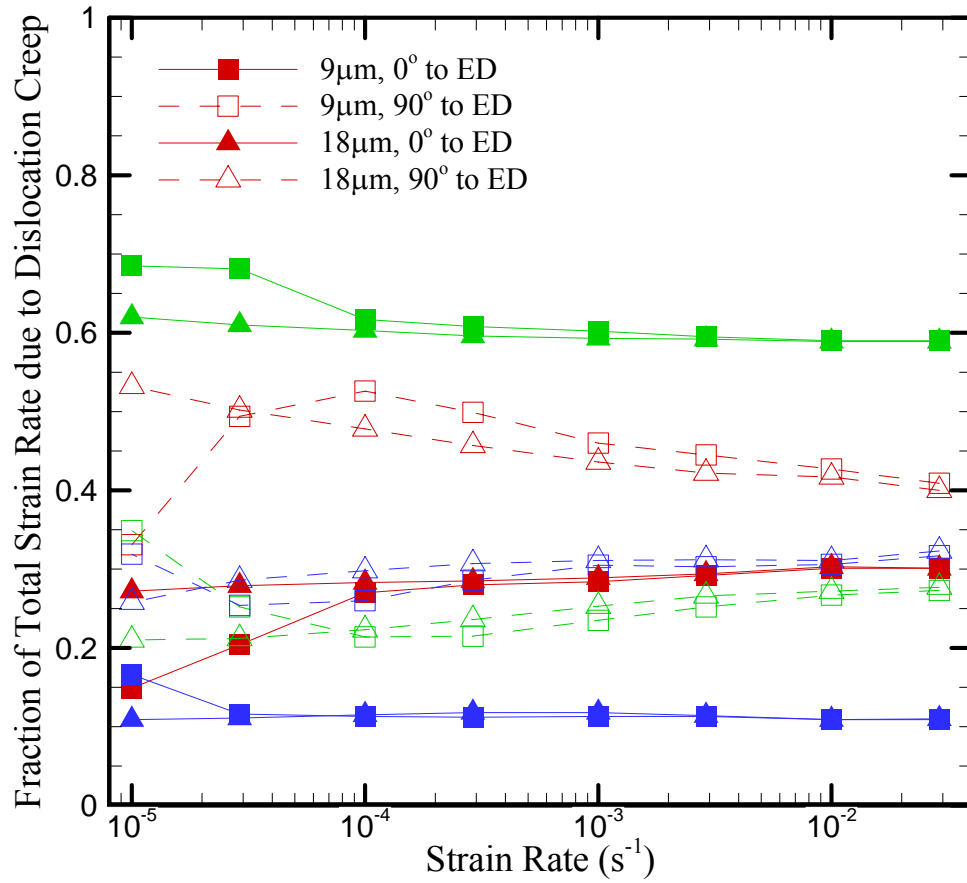


Figure 5.6: The predicted percent contribution to the total strain rate due to dislocation creep from slip on the basal, prismatic and pyramidal slip system as a function of strain rate for the simulations based on the actual material and the simulations based on a fabricated material with alternate grain size and orientation at 450°C.

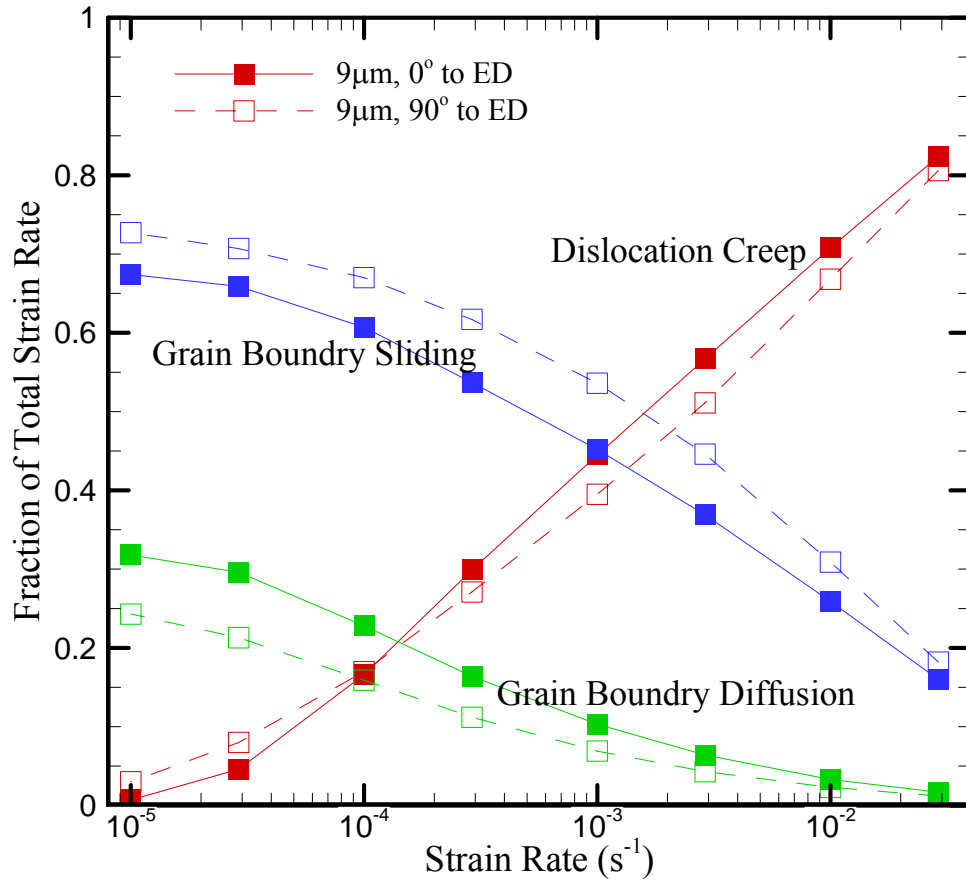


Figure 5.7: The predicted percent contribution to total strain rate from each deformation mechanism, DC, GBD, and GBS as a function of strain rate and orientation of the tensile axis at 450°C with constant grain size of 9 $\mu$ m.



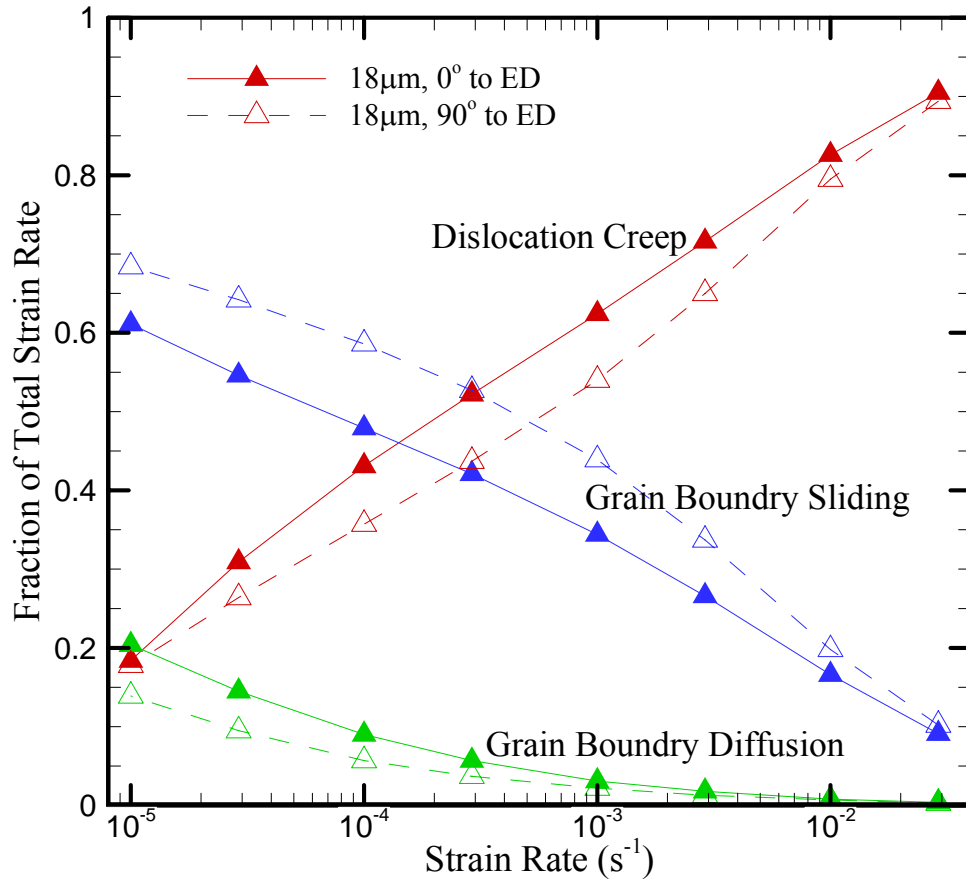


Figure 5.8: The predicted percent contribution to total strain rate from each deformation mechanism, DC, GBD, and GBS as a function of strain rate and orientation of the tensile axis at 450°C with constant grain size of 18 $\mu$ m.

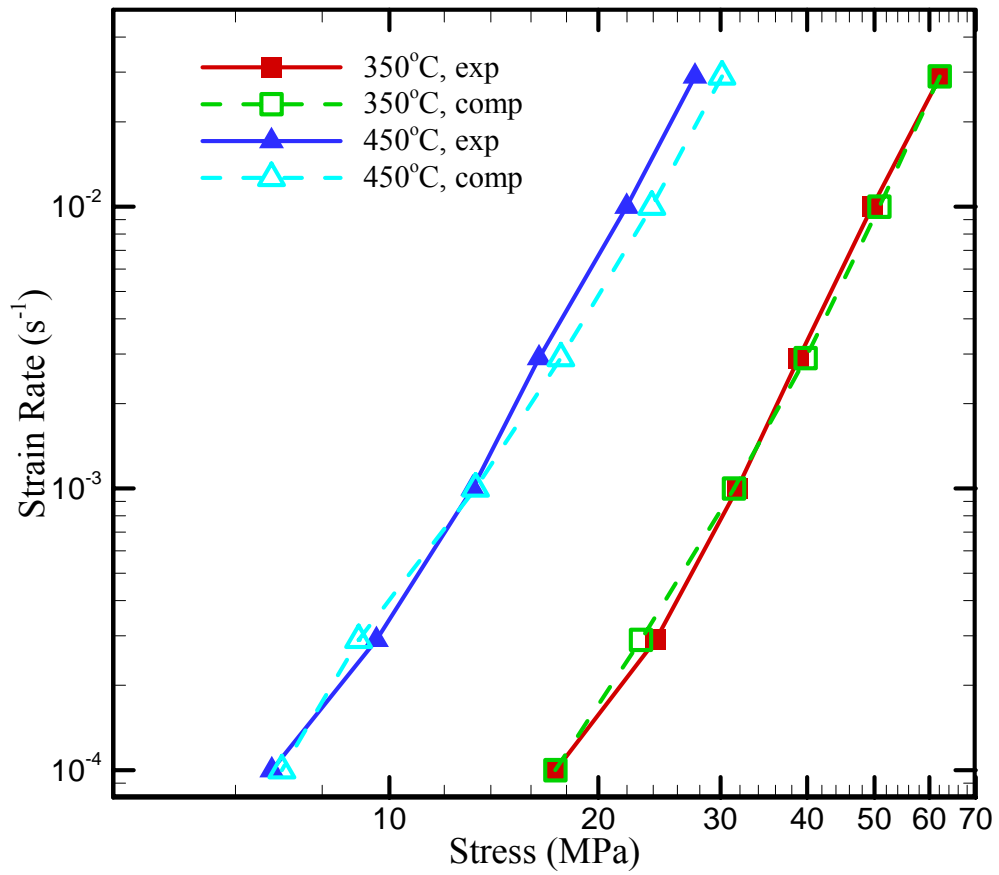


Figure 5.9: Computational and experimental strain rate vs. stress curves for the AZ31 extruded sheet material oriented with the tensile axis 0° to the extruded direction tested at 350°C and 450°C. The simulation shows good fit to experiment.

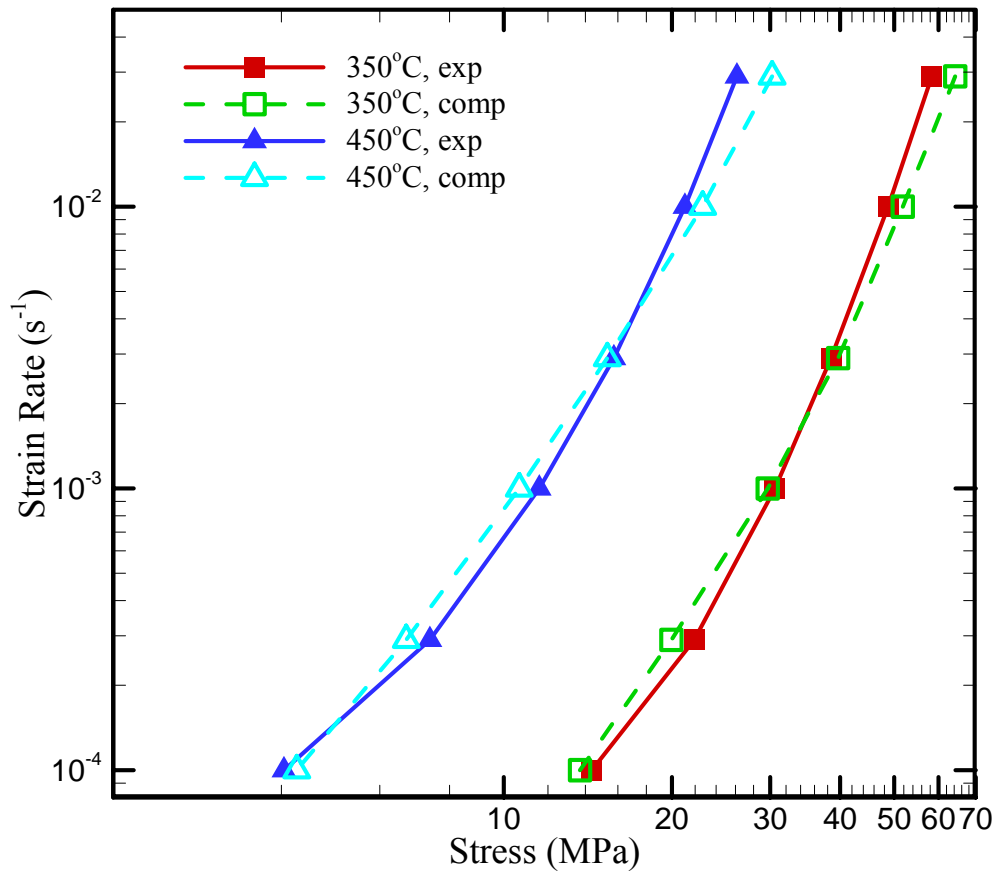


Figure 5.10: Computational and experimental strain rate vs. stress curves for the AZ31 extruded sheet material oriented with the tensile axis  $90^\circ$  to the extruded direction tested at  $350^\circ\text{C}$  and  $450^\circ\text{C}$ . The simulation shows good fit to experiment.

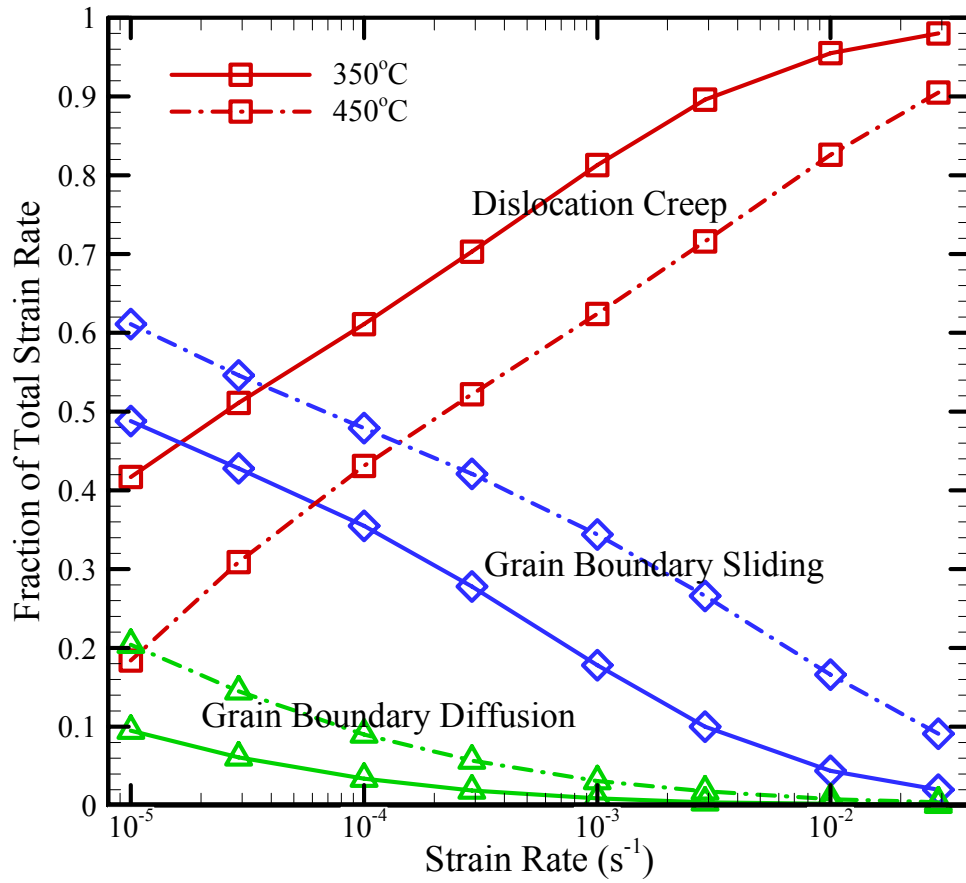


Figure 5.11: The predicted percent contribution to total strain rate from each deformation mechanism, DC, GBD, and GBS as a function of strain rate and temperature for loading 0° to the ED.

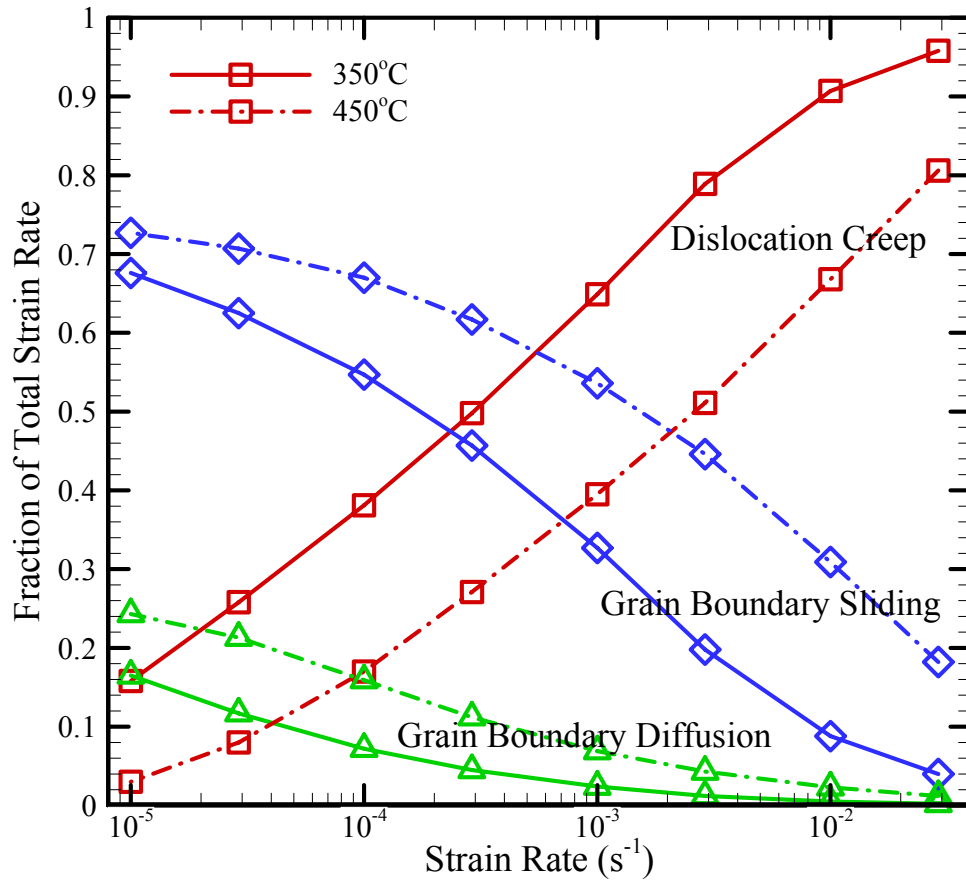


Figure 5.12: The predicted percent contribution to total strain rate from each deformation mechanism, DC, GBD, and GBS as a function of strain rate and temperature for loading 90° to the ED.

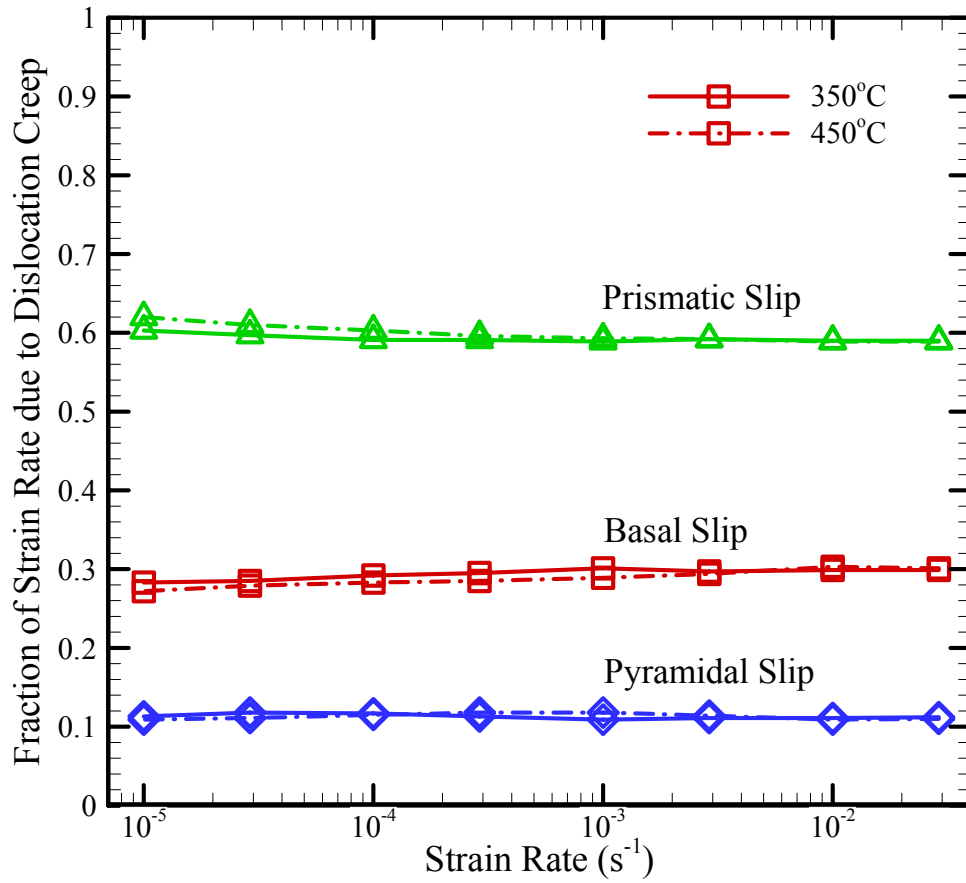


Figure 5.13: The predicted percent contribution to the total strain rate due to dislocation creep from slip on the basal, prismatic and pyramidal slip system in magnesium AZ31 as a function of strain rate and temperature for loading  $0^\circ$  to the ED.

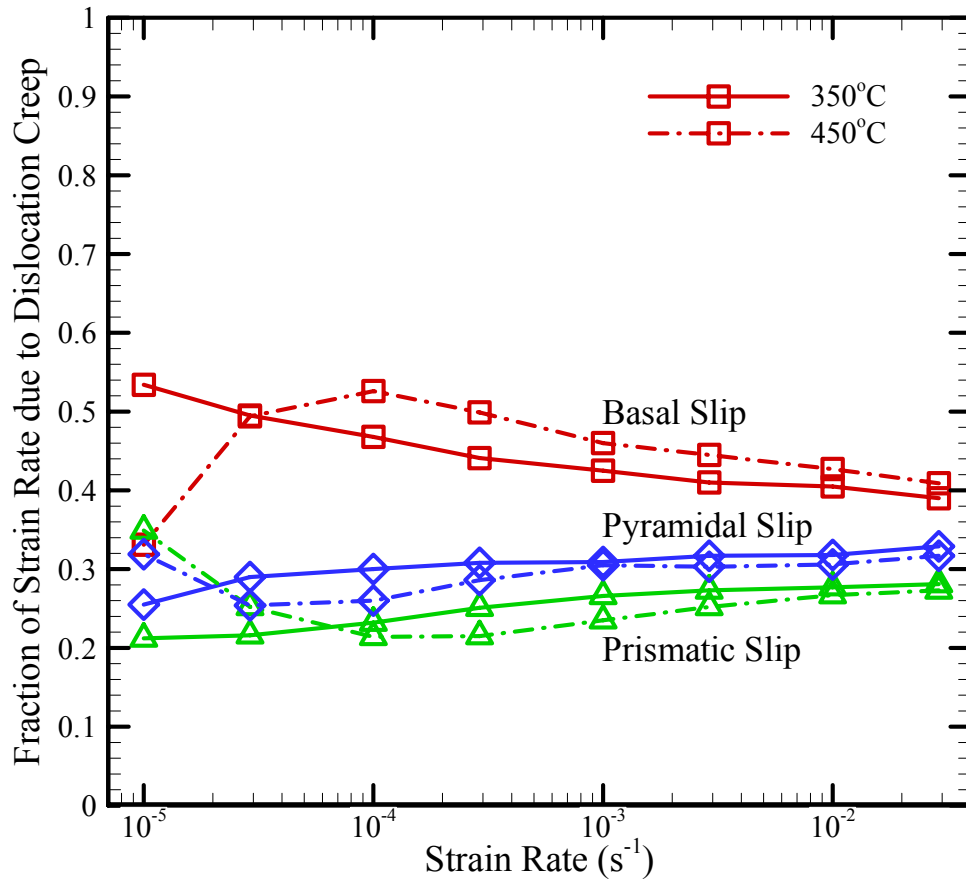


Figure 5.14: The predicted percent contribution to the total strain rate due to dislocation creep from slip on the basal, prismatic and pyramidal slip system in magnesium AZ31 as a function of strain rate and temperature for loading  $90^\circ$  to the ED.

# CHAPTER 6: A FINER EXAMINATION OF GRAIN BOUNDARY SLIDING

## 6.1 Introduction and Motivation

The model was also utilized in a more in-depth study of the nature of grain boundary sliding. The work was completed for aluminum alloy 5083, in an attempt to further efforts to investigate the various deformation mechanisms that contribute to elevated temperature deformation in aluminum (Kulas, Green, Taleff, Krajewski, & McNelley, 2005, 2006; McNelley, Oh-Ishi, Zhilyaev, Swaminathan, Krajewski, et al., 2007). Experiments show that under conditions which resemble QPF (at temperature of 450°C and strain rates of  $10^{-5} s^{-1} < \dot{\epsilon} < 10^{-2} s^{-1}$ ), the creep response of AA5083 undergoes a transition in deformation mechanism from grain boundary sliding at slow rates to solute drag – dislocation creep at higher strain rates. McNelley et al. has characterized this transition by a number of factors including an increase in strain rate sensitivity,  $m$ , from 2.7 to 4.0, an increase in texture intensity, macroscopic flow localization (necking), a decrease in the amount and rate of cavitation, and a change in activation energy (McNelley, Oh-Ishi, Zhilyaev, Swaminathan, Krajewski, et al., 2007).



Using a similar framework to the model described in chapter 3, a detailed computational study of the mechanisms of deformation and constitutive behavior of AA5083 was carried out by Agarwal et al. (Agarwal, Briant, Krajewski, Bower, & Taleff, 2007). The computations predicted macroscopic creep behavior that was in good agreement with experiment. Similar to the work described in chapter 4, the simulations were also used to compute the relative contributions to the overall plastic strain from dislocation creep, grain boundary diffusion, and grain boundary sliding. The results confirmed that grain boundary sliding dominates at low strain rates, while dislocation creep dominates at high strain rates, and predicted a critical strain rate for the transition which was in good agreement with experiment.

It is likely that the transition in deformation mechanism controls the maximum strain rate that can be achieved during quick plastic forming. It is therefore of particular interest to identify microstructural and material parameters that control the transition point. Preliminary simulations reported by Agarwal and Du et al. suggest that the transition point is particularly sensitive to the sliding resistance of grain boundaries (Agarwal, Briant, Krajewski, et al., 2007; Du, Bower, Krajewski, & Taleff, 2008). In each of these previous continuum simulation studies it was assumed for simplicity that each grain boundary in the polycrystal had identical grain boundary sliding properties. However, both experiments and atomic simulations have demonstrated the sliding resistance of a grain boundary is strongly sensitive to the relative orientations of the two grains adjacent to that boundary. Weinberg showed a dependence of grain-boundary sliding on the orientation of the grain boundary and temperature (Weinberg, 1958); Kokawa et al. observed different sliding behaviors and dislocation structures in aluminum

on ordered (coincidence) and random boundaries (Kokawa, Watanabe, & Karashima, 1981); and Fukutomi et al. showed that both the “internal stress” (below which no sliding occurs) and grain boundary sliding rate depend on grain boundary structures (Fukutomi, Yamamoto, Nonomura, & Takada, 1999). Furthermore, recent MD simulations suggest the existence of a threshold stress, which greatly depends on the grain boundary energy, with lower energy grain boundaries have higher threshold stress and lower levels of sliding (Qi & Krajewski, 2007). Consequently, the sliding resistance of the boundaries in a polycrystal is likely to be highly heterogeneous. Moreover, the fraction of boundaries with low sliding resistance can, in principle, be modified by adjusting the texture of the polycrystal.

## **6.2 Material Parameters and Deformation in Homogenous Material**

In a similar fashion to the validation process described in chapter 4, Agarwal et al. determined values for material properties in the constitutive equations listed in chapter 3 (Agarwal, Briant, Krajewski, et al., 2007). Parameters were selected that gave the best fit to experimental stress-v-strain rate data reported by Kulas et al., while also predicting a critical strain rate for a transition from grain boundary sliding creep to dislocation creep that matched measurements of texture (Kulas, Green, Taleff, Krajewski, et al., 2005). Agarwal et al. used a more elaborate exponential constitutive equation to model dislocation creep, in contrast to the simple power-law (equation 3.7) used here (Agarwal, Briant, Krajewski, et al., 2007). Consequently, the procedure was repeated to determine values of material parameters in the new creep law that best fit experimental data. To

account for the improvement of the creep law, the grain boundary diffusion pre-exponential was changed from  $\delta_{GB}D_{GBt} = 9.9 \times 10^{-14} \text{ m}^3/\text{s}$  to  $\delta_{GB}D_{GBt} = 1.02 \times 10^{-13} \text{ m}^3/\text{s}$  to ensure that the transition from dislocation creep to grain boundary sliding continued to correspond with texture measurements. All values were fit using a homogeneous grain structure with freely sliding grain boundaries, and are listed in Table 6.1. The grain size,  $L$ , is used to generate the mesh, and is included in the table along with the fitting parameters. The representative microstructure used in the simulations was taken directly from a micrograph of AA5083, including the orientation of each grain, and is shown in figure 6.1. The grain size was measured using the linear intercept method to be  $7\mu\text{m}$ . The major change in the crystal plasticity model that is described in chapter 3 is that the grains are idealized as fcc single crystals. Elastic deformation is defined by the linear-elastic constitutive equations for a cubic crystal with Young's modulus  $E$ , shear modulus  $\mu$ , and Poisson's ratio  $\nu$ , and plastic deformation is computed from plastic shearing on the twelve  $\{111\}\langle 110 \rangle$  slip systems.

The main objective is to determine the influence of heterogeneity in sliding resistance of the grain boundaries on the behavior of the polycrystal. Before considering a heterogeneous microstructure, however, it is instructive to examine the influence of grain boundary sliding resistance in a homogeneous material. To this end, figure 6.2 shows the strain rate- $\nu$ -stress response of a polycrystal in which all grain boundaries have an equal resistance to sliding. Results are shown for grain boundary fluidity

$4.74 \times 10^{-12} \text{ m}^3/\text{MN} \cdot \text{s} \leq \eta \leq 4.74 \times 10^{-8} \text{ m}^3/\text{MN} \cdot \text{s}$ . The contributions to the total strain rate from dislocation creep, grain boundary sliding, and grain boundary diffusion are shown in figure 6.3 for the extreme values of  $\eta$ . Two features of the results are notable: if

the fluidity satisfies  $\eta \leq 4.74 \times 10^{-12} \text{ m}^3/\text{MN} \cdot \text{s}$ , grain boundary sliding is completely suppressed, and dislocation creep is the dominant deformation mechanism at all strain rates. The strain rate-v-flow stress response of the solid is closely approximated by a power-law relationship of the form  $\dot{\epsilon} = A\sigma^n$ , with  $n \approx 4$  independent of strain rate. In contrast, if  $\eta \geq 4.74 \times 10^{-8} \text{ m}^3/\text{MN} \cdot \text{s}$ , the grain boundaries slide freely (further increases in  $\eta$  causes no change in the behavior of the material). Under these conditions, the strain rate-v-stress response of the material has two regimes. For strain rates  $\dot{\epsilon} > 3 \times 10^{-3} \text{ s}^{-1}$ , power-law behavior with  $n \approx 4$  is observed, while for  $\dot{\epsilon} < 3 \times 10^{-3} \text{ s}^{-1}$  the stress exponent  $n \approx 1.5$ . This change in behavior is caused by a transition in deformation mechanism from dislocation creep at high rates, to grain boundary sliding at low rates, as illustrated in figure 6.3. It should be noted that although the dominant deformation mechanism at high strain rates and high grain boundary fluidity is dislocation creep, grain boundary sliding still makes a significant contribution to deformation. This is valid for the small grain size used in the simulation and is similar to the results reported by Agarwal (Agarwal, Briant, Krajewski, et al., 2007). The fraction of strain due to grain boundary sliding continues to decrease if the strain rate is increased beyond  $0.01 \text{ s}^{-1}$ , and drops to essentially zero at a strain rate of  $1.0 \text{ s}^{-1}$  (not shown in the graph).

Adjusting the grain boundary sliding fluidity of all the grain boundaries is similar to increasing the grain size of the microstructure; it is one of the parameters that must be adjusted when the grain size is adjusted in the dimensionless parameters (equation 4.1). However, in this study the grain boundary sliding fluidity parameter will be adjusted individually for each grain boundary.

## 6.3 The Effect of Grain Boundary Sliding Heterogeneity on Deformation

The influence of heterogeneity in grain boundary sliding resistance is investigated by assuming that each grain boundary has one of two possible values of sliding resistance. A fraction,  $f$ , of the boundaries slide freely with  $\eta = 4.74 \times 10^{-8} \text{ m}^3 / \text{MN} \cdot \text{s}$ , while the remaining fraction of grain boundaries ( $1-f$ ) are assumed to completely resist sliding, with  $\eta = 4.74 \times 10^{-12} \text{ m}^3 / \text{MN} \cdot \text{s}$ . Each grain boundary is randomly assigned one of these values of sliding fluidity, where the ratio of the number of the total freely sliding grains to the total number of grain boundaries is  $f$ .

### 6.3.1 The Effect of $f$ on the Overall Constitutive Behavior

The influence of the fraction  $f$  of freely sliding boundaries on the strain rate-v-stress response is illustrated in figure 6.4. As expected, the stress-v-strain rate curves transition from the limiting case of a homogeneous solid with sliding resistant grains to that of a polycrystal with freely sliding grains as  $f$  increases from 0 to 100 percent. The contribution to the total strain rate from each of the three possible mechanisms of plastic flow is shown in figure 6.5, for the same values of  $f$ : these results show the same transition. Increasing the fraction of freely sliding boundaries reduces the flow stress in both the dislocation creep regime and the grain boundary sliding regime: for example, the

flow stress at a strain rate of  $10^{-4} s^{-1}$  (GBS regime) increases from 6MPa to 14MPa as  $f$  varies from 100 percent to 0 percent; in contrast the flow stress at strain rate of  $0.01 s^{-1}$  increases from 33MPa to 42MPa (DC regime). In addition, the fraction of freely sliding grain boundaries has a strong influence on the stress exponent in the grain boundary sliding regime, where  $n$  decreases from approx 3.25 to 1.5 as  $f$  increases from 0 to 100 percent. The stress exponent in the dislocation creep regime is only slightly affected, decreasing from approx 4.3 to 3.4 as  $f$  increases from 0 to 100 percent.

### 6.3.2 The Effect of $f$ on Flow Stress

The influence of  $f$  on the flow stress is shown more clearly in figure 6.6, which shows the variation of  $\sigma$  as a function of  $f$ , for several values of the imposed strain rate  $\dot{\epsilon}$ . This figure shows a sudden drop in flow stress as  $f$  is increased from 67 percent to 77 percent, as well as a second, less obvious drop as  $f$  is increased from 39 percent to 46 percent. The drops in flow stress are associated with an increase in the contribution to the total strain rate from grain boundary sliding, as shown in figure 6.7. The increase in strain rate due to sliding is particularly pronounced between  $f=67$  percent and 77 percent at strain rates of order  $10^{-3}$  (near the transition in deformation mechanism). The changes in strain rate due to sliding and dislocation creep occur at the same fraction  $f$  because the simulations impose a constant total strain rate on the microstructure: if one increases, the other must decrease.

The sudden increase in grain boundary sliding is likely to be due to a percolation threshold: with  $f > 77$  percent, the freely sliding grain boundaries link up and provide a

mechanism for the crystal to deform primarily by shearing along grain boundaries; for  $f < 67$  percent there is no connected path of grain boundaries across the simulation cell and this mechanism of sliding cannot occur.

The origin of the discontinuity that occurs between  $f = 39$  percent and 46 percent is less clear. In general, the microstructures for  $f = 39$  percent were observed to contain at least one grain which is completely surrounded by sliding resistant grain boundaries, while the microstructures with  $f = 46$  percent do not contain such grains. It is possible that these highly constrained grains act as reinforcing particles.

### **6.3.3 The Effect of $f$ on the Transition in Deformation Mechanisms**

It is of particular interest to determine the critical strain rate at which the mechanism of plastic flow transitions from grain boundary sliding to dislocation creep, since the transition in deformation mechanism seems to correlate with the optimum strain rate for hot blow forming. Experimentally, the transition point is determined by the intersection of the two power-law fittings of stress and strain rate curve. To better quantify this transition, the critical strain rate is taken to be the point at which the contribution to the total strain rate from grain boundary sliding and dislocation creep are equal. Figure 6.8 shows the variation of this critical strain rate with the fraction  $f$  of freely sliding boundaries. The critical strain rate was found to vary from  $2 \times 10^{-5} s^{-1}$  to  $10^{-3} s^{-1}$  as  $f$  is increased from 20 to 100 percent. In addition, a large drop in critical strain rate was observed from  $4.4 \times 10^{-4} s^{-1}$  to  $1.0 \times 10^{-4} s^{-1}$  as  $f$  is reduced from 77 to 67 percent: this jump is again associated with a percolation threshold for grain boundary

sliding. This suggests that keeping  $f > 77$  percent is likely to substantially improve formability of AA5083.

#### **6.4.4 The Influence of the Spatial Distribution of the Free Sliding Grain Boundaries**

It is important to examine the sensitivity of the flow behavior on the detailed spatial distribution of sliding resistant grain boundaries. For example, figure 6.9 compares the predicted flow stress-v-strain rate for three different representations of a microstructure with  $f=50$ : (i) a random distribution of non-sliding grain boundaries; (ii) a microstructure in which the freely sliding boundaries were aligned at 45 degrees to the loading direction, indicated by the highlighted grain boundaries in figure 6.10; and (iii) a microstructure in which the sliding resistant boundaries were aligned at 45 degrees to the loading direction (for this case, the highlighted boundaries in figure 6.10 were assigned a high resistance to sliding). The flow stress is slightly reduced for microstructure (ii) in the grain boundary sliding regime, and slightly elevated for case (iii), but the effect is not significant.

#### **6.3.5 Discussion**

A sudden increase in the contribution from GBS to deformation and a corresponding reduction in flow stress occur as  $f$  increased from 67 percent to 77 percent, suggest the presence of a percolation threshold. At this threshold, multiple sliding



boundaries connect to permit rapid straining in the microstructure. In a two-dimensional model, the polycrystal can be loosely regarded as a lattice model, where each grain is a polyhedron with a bond that can be oriented perpendicular to the grain boundary. Specifically, the 2D polycrystal used in this study is very close to the 2D-hexagonal lattice model. The simulated threshold determined here is just above the "bond percolation" threshold of 65 percent for the 2D-hexagonal lattice. Recent simulations of Coble creep by Chen using a 2D model composed of rigid grains connected by grain boundaries that have either a high or low diffusivity obtained a percolation threshold that was slightly below the classical model (Chen & Schuh, 2006, 2007). It is expected that a 3D polycrystal will show a similar qualitative trend, but the critical  $f$  is unlikely to correspond to the simple connectivity threshold for a 3D lattice, since a connected path of fast sliding grain boundaries is not sufficient to allow unconstrained deformation in a 3D crystal structure. The threshold may be closer to the 'rigidity percolation threshold,' in which only bond-stretching forces are included. Rigidity percolation thresholds are greater than connectivity percolation models, for example: the rigid threshold for a triangular lattice is 0.642, much higher than 0.347 for an ordinary connectivity percolation. Further work is needed to explore the exact percolation threshold for the 3D polycrystal structure as well as the microstructural sensitivity of the percolation threshold. However, the 2D simulations suggest that the fraction of freely sliding boundaries should exceed 60 percent to give the best formability.

If it is assumed that the high angle boundaries in a polycrystal slide freely, then the fraction of freely sliding boundaries in most QPF aluminum alloys is likely to exceed 60 percent. Recent experiments by McNelley et al. show that although a typical cold-

rolled AA5083 sheet has a high fraction of low angle boundaries, after it has been annealed at 450°C the boundaries develop a random distribution, and over 90 percent of the boundaries in an annealed polycrystal are high angle boundaries (McNelly, Oh-Ishi, Zhilyaev, Swaminathan, Krajewski, et al., 2007). The QPF process is performed at 450°C, so low angle boundaries that are present in the initial blank are likely to disappear during forming, although it is not clear whether this can occur during the time-scales of a typical forming operation. It is impossible, however, to state with certainty that high angle boundaries in AA5083 can be considered to be freely sliding. Du et al. show that a threshold stress of only 3-5MPa can prevent grain boundary sliding under QPF conditions (Du, Bower, et al., 2008). MD simulations predict a very high threshold stress for grain boundary sliding even for high angle boundaries (exceeding 100MPa), suggesting that  $f=0$ , but these simulations probably greatly overestimate the threshold stress due to the short simulation times (Qi & Krajewski, 2007). Experimental data are not available for AA5083, and experimental measurements of grain boundary sliding rates are in general scarce and subject to considerable scatter. These are important questions for future research.

## 6.4 Conclusions

Finite element simulations were used to investigate the influence of heterogeneity in the sliding resistance of grain boundaries on the creep response of AA5083 during high temperature straining. Heterogeneity in sliding resistance was modeled by randomly

assigning each grain boundary in the polycrystal one of two possible values of sliding resistance: a fraction  $f$  were taken to slide freely; while the remaining fraction  $(1-f)$  were assumed to completely resist sliding. The computations predict the steady-state creep stress in the polycrystal as a function of applied strain rate, as well as the contributions to the total plastic strain rate arising from dislocation creep, grain boundary diffusion, and grain boundary sliding. The simulations showed that:

1. The critical strain rate at which the dominant deformation mechanism transitions from dislocation creep to grain boundary sliding varies from  $2.0 \times 10^{-5} s^{-1}$  to  $1.0 \times 10^{-3} s^{-1}$  as the fraction of freely sliding grain boundaries  $f$  is increased from 20 to 100 percent.
2. The stress exponent in the grain boundary sliding regime decreases from approximately 3.25 to 1.5 as  $f$  increases from 0 to 100 percent. The stress exponent in the dislocation creep regime is less sensitive to increasing  $f$ .
3. The flow stress in the grain boundary sliding regime is significantly reduced as  $f$  increases. For example, at a strain rate of  $1.0 \times 10^{-4} s^{-1}$ , the flow stress decreases from 14MPa to 6MPa as  $f$  varies from 0 to 100 percent. In contrast, the flow stress in the dislocation creep regime is relatively insensitive to  $f$ : at a strain rate of  $0.01 s^{-1}$ , the flow stress drops from 42MPa to 33 MPa as  $f$  varies from 0 to 100 percent.
4. A sudden increase in grain boundary sliding, and a corresponding reduction in flow stress is observed as  $f$  is adjusted from 67 to 77 percent, suggesting the

presence of a percolation threshold.

5. The flow stress and deformation mechanism are determined by the fraction of freely sliding grains, and are not sensitive to the detailed spatial distribution of sliding resistance in the polycrystal.

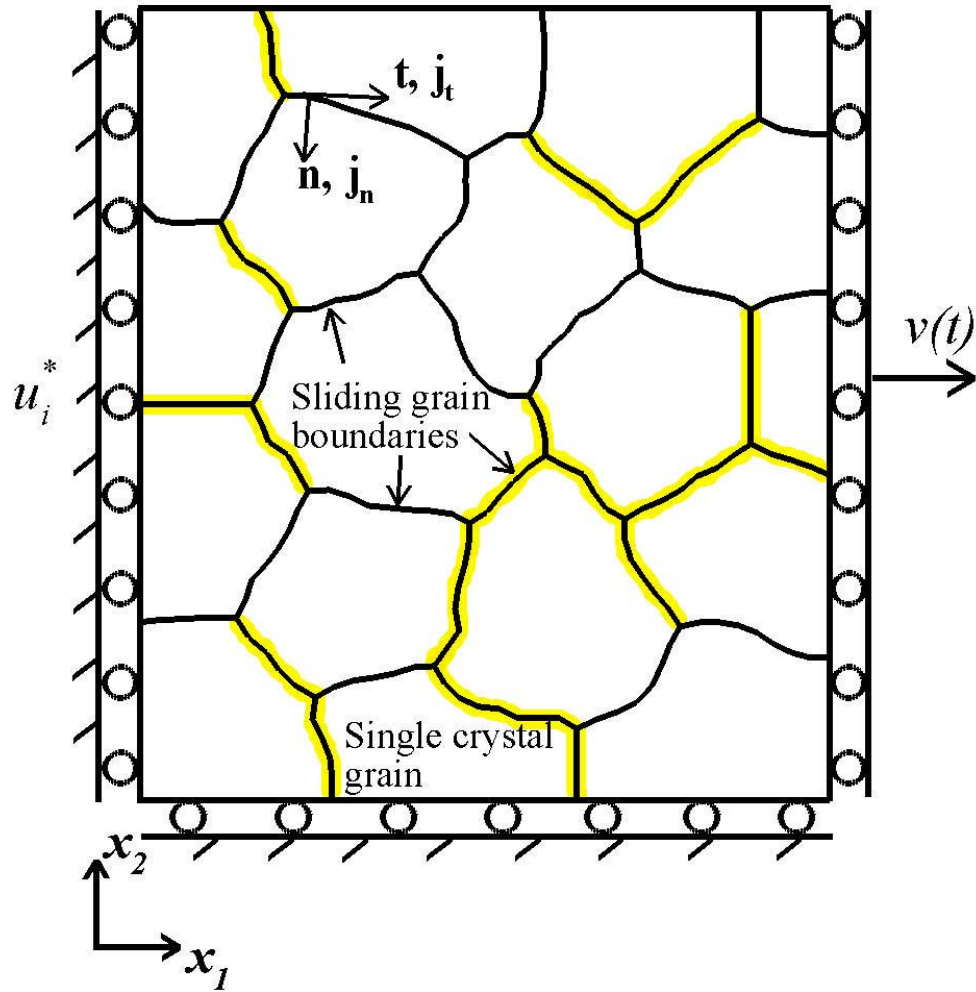


Figure 6.1: Schematic of the microstructure used in the finite element simulations for aluminum alloy 5083.

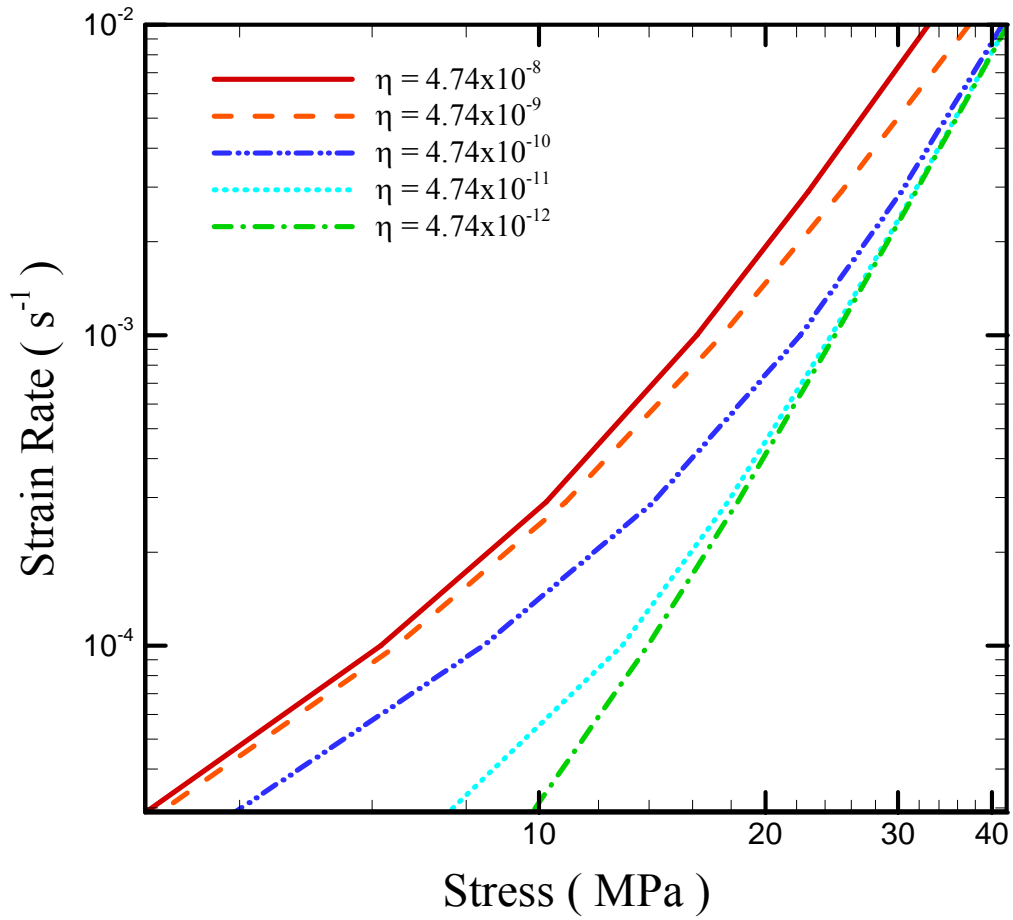


Figure 6.2: Strain rate as a function of stress for multiple values of constant grain boundary fluidity  $\eta$ .

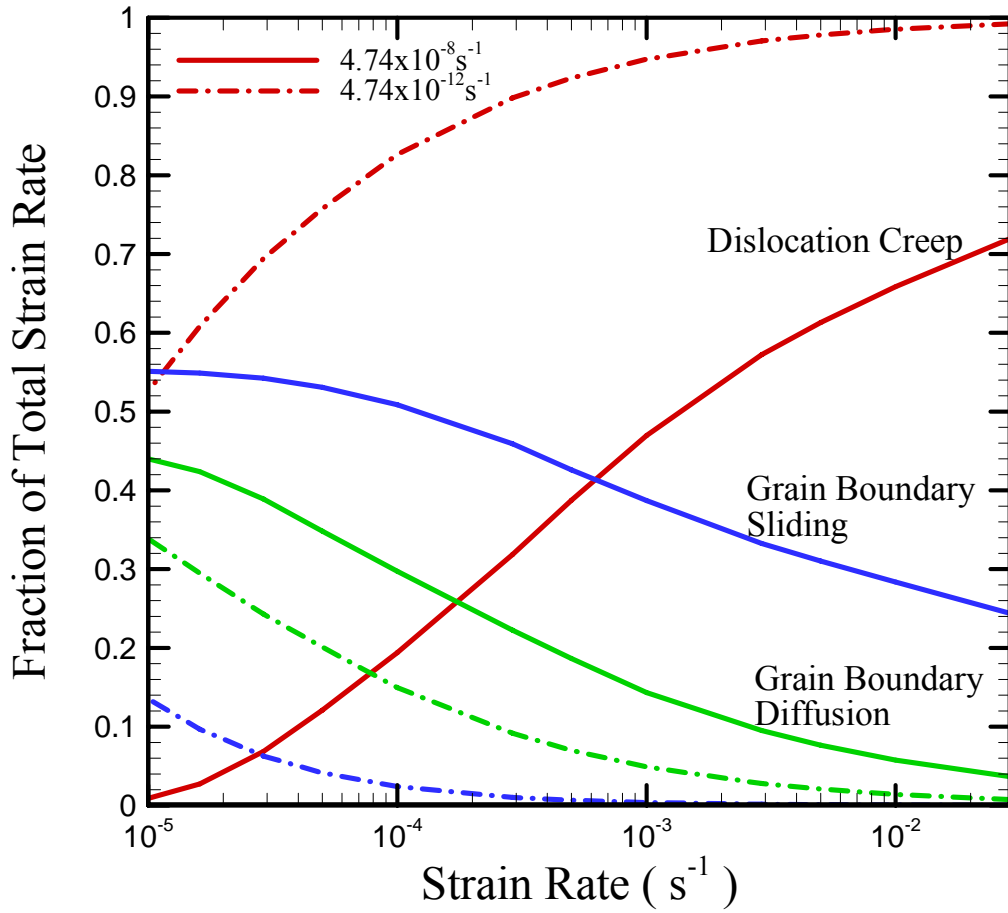


Figure 6.3: The predicted percentage contribution of total strain rate from dislocation creep, grain boundary diffusion and grain boundary sliding for simulations where  $\eta = 4.74 \times 10^{-8} \text{ m}^3 / \text{MN} \cdot \text{s}$  and  $\eta = 4.74 \times 10^{-12} \text{ m}^3 / \text{MN} \cdot \text{s}$ .

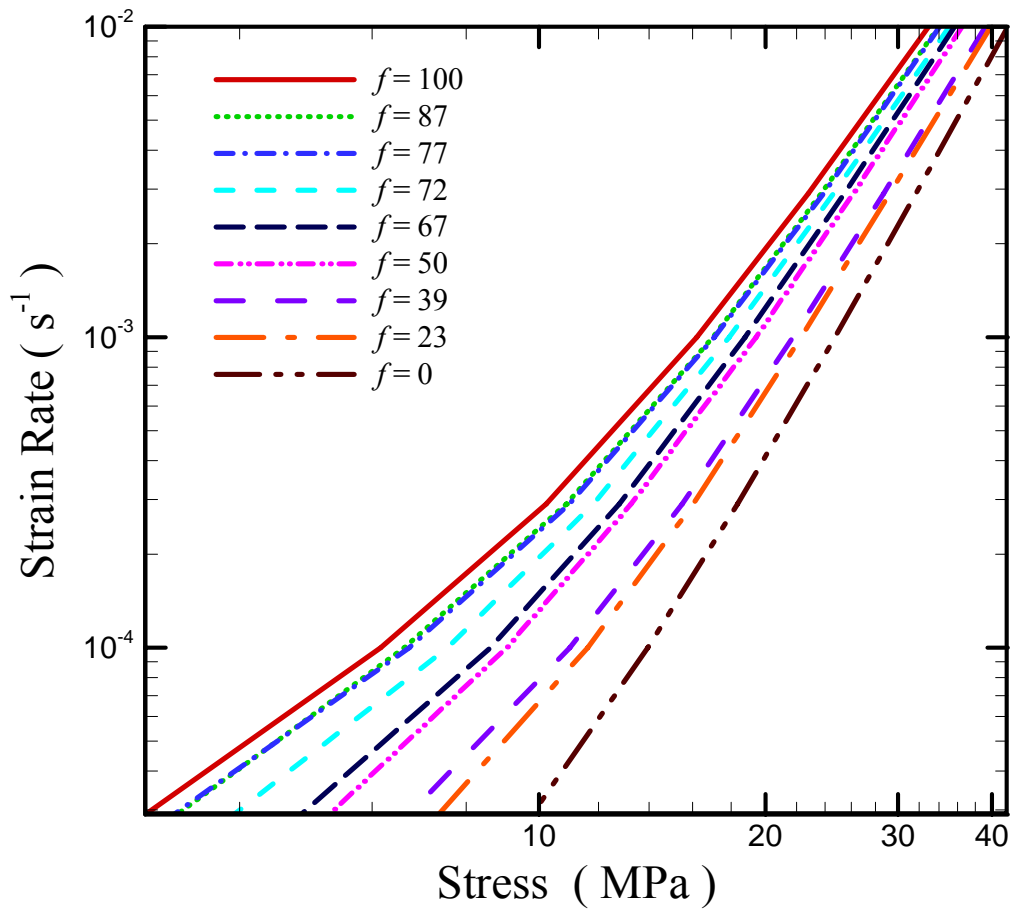
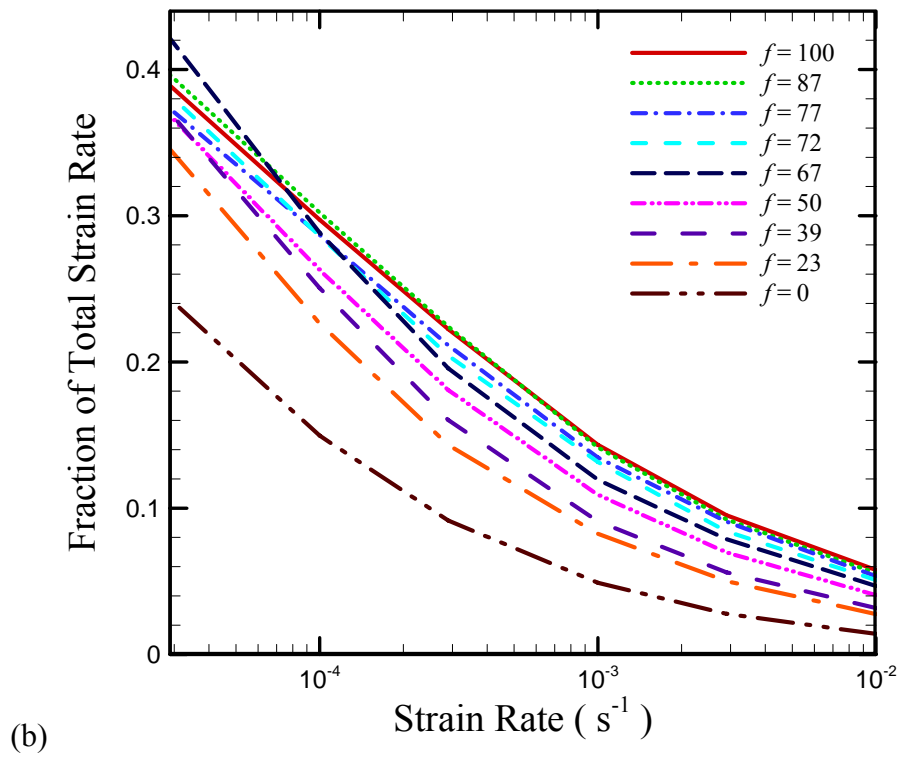
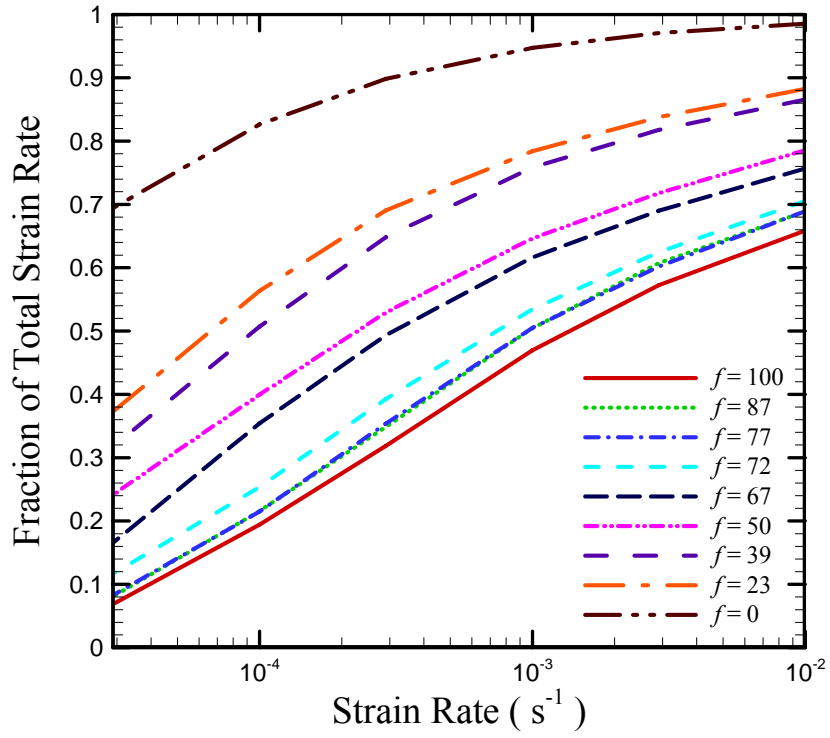
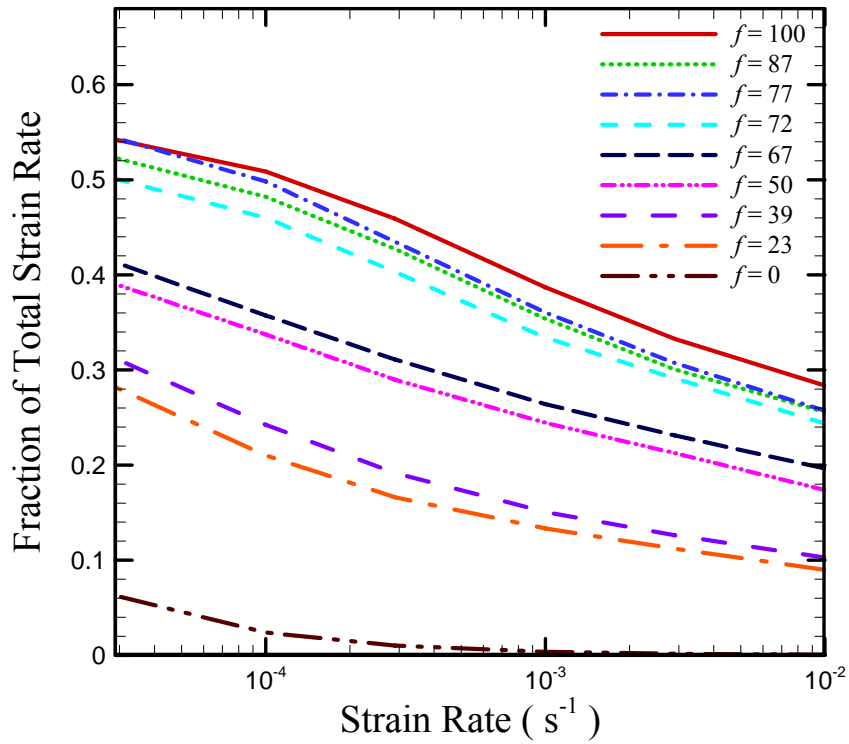


Figure 6.4: Plot of strain rate vs. stress for simulated results of varying percent of grain boundaries with allowable grain boundary sliding.







(c)

Figure 6.5: Plots for percent contribution to total strain rate for each deformation mechanism ((a) dislocation creep; (b) grain boundary diffusion; (c) grain boundary sliding) plotted for various values of *f*.

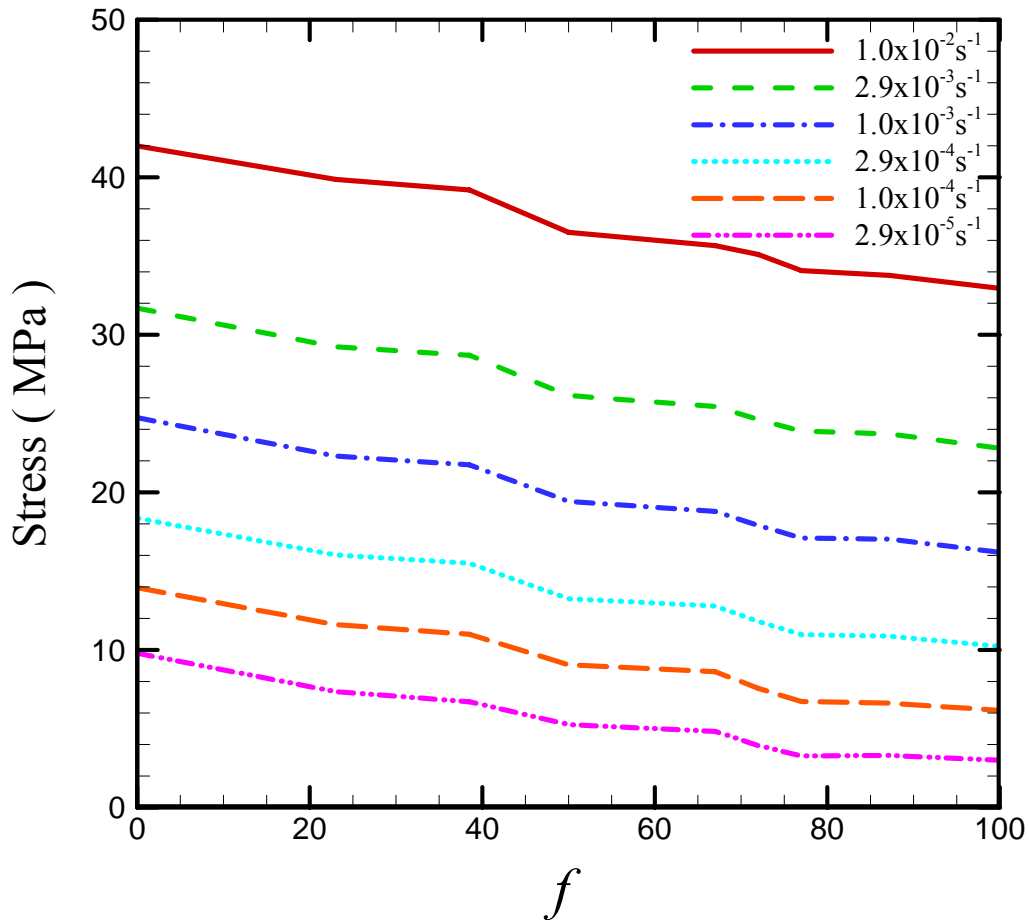


Figure 6.6: Plot of flow stress as a function of  $f$  for several values on constant strain rate.

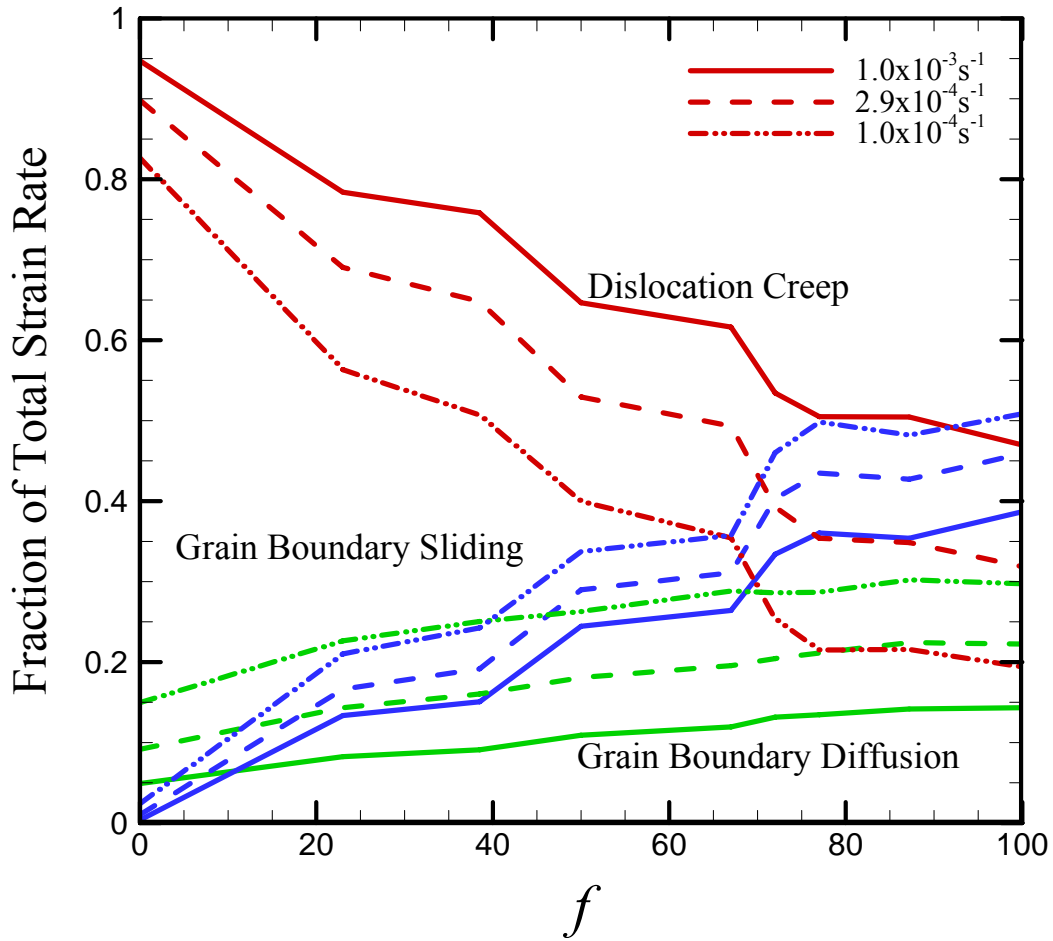


Figure 6.7: Plots of the percent contribution to total strain rate attributed to each mechanism of plastic flow as a function of  $f$ , plotted at several constant strain rates:  $\dot{\epsilon} = 1.0 \times 10^{-3} s^{-1}$ ,  $\dot{\epsilon} = 2.9 \times 10^{-4} s^{-1}$ , and  $\dot{\epsilon} = 1.0 \times 10^{-4} s^{-1}$ .

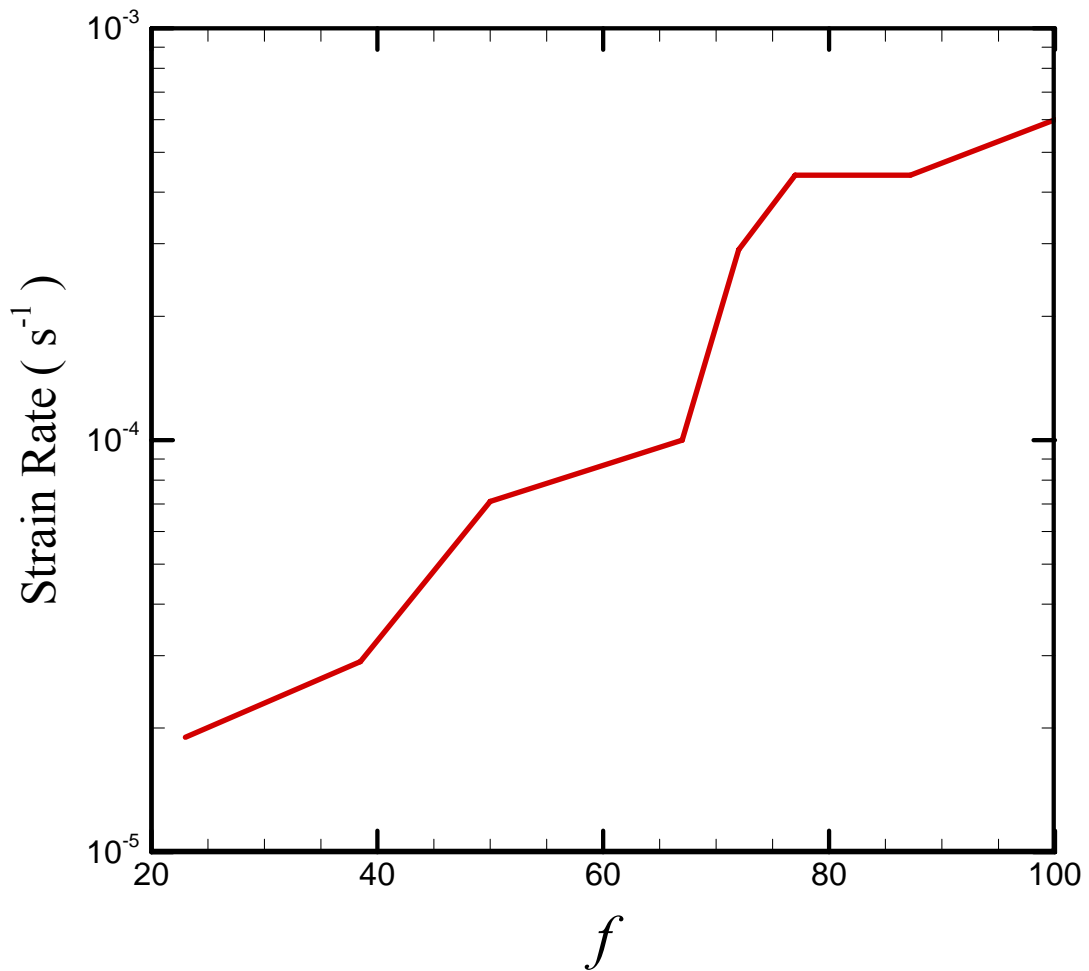


Figure 6.8: The strain rate where the transition in the dominant deformation mechanism between dislocation creep and grain boundary sliding plotted as a function of  $f$ .

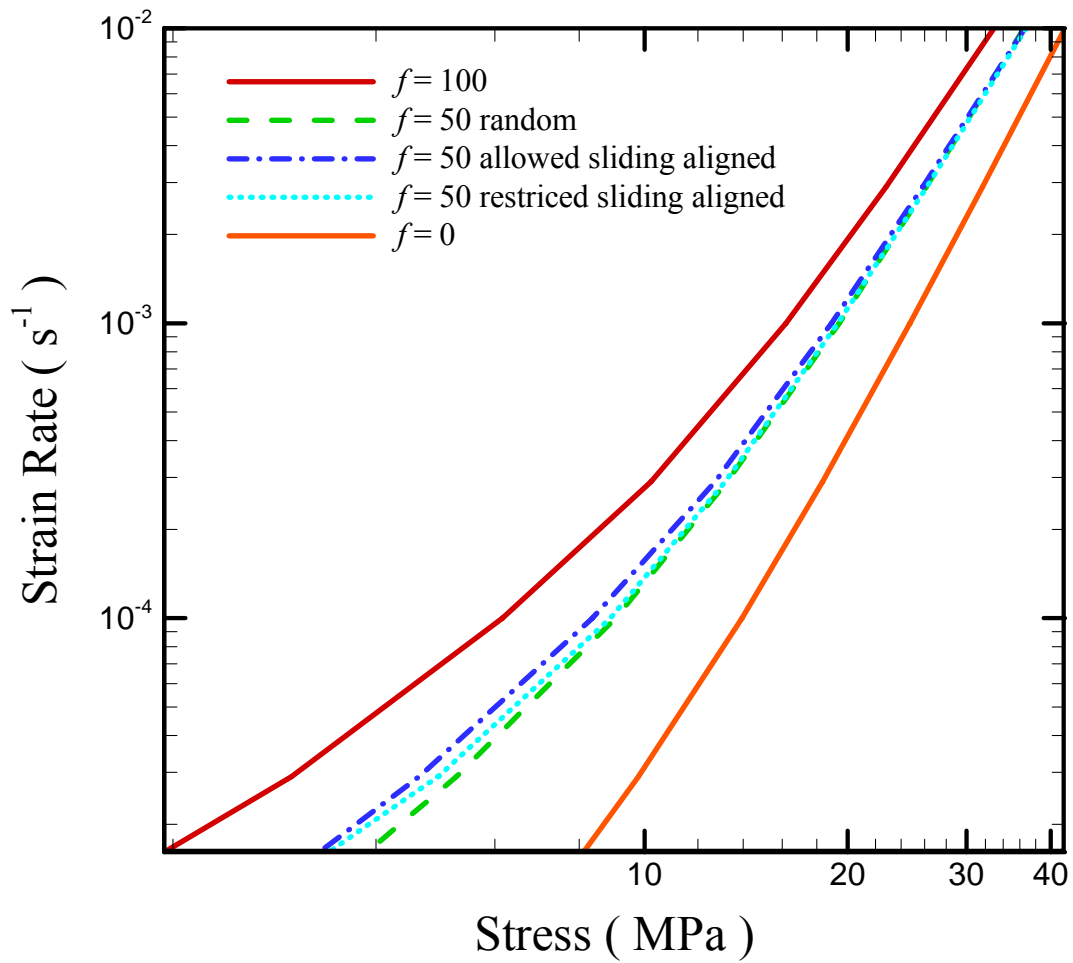


Figure 6.9: Strain rate plotted as a function of stress for  $f=54$  percent with different distributions of the grain boundaries that are allowed and restricted to slide.  $f=100$  percent and  $f=0$  percent are plotted for reference.

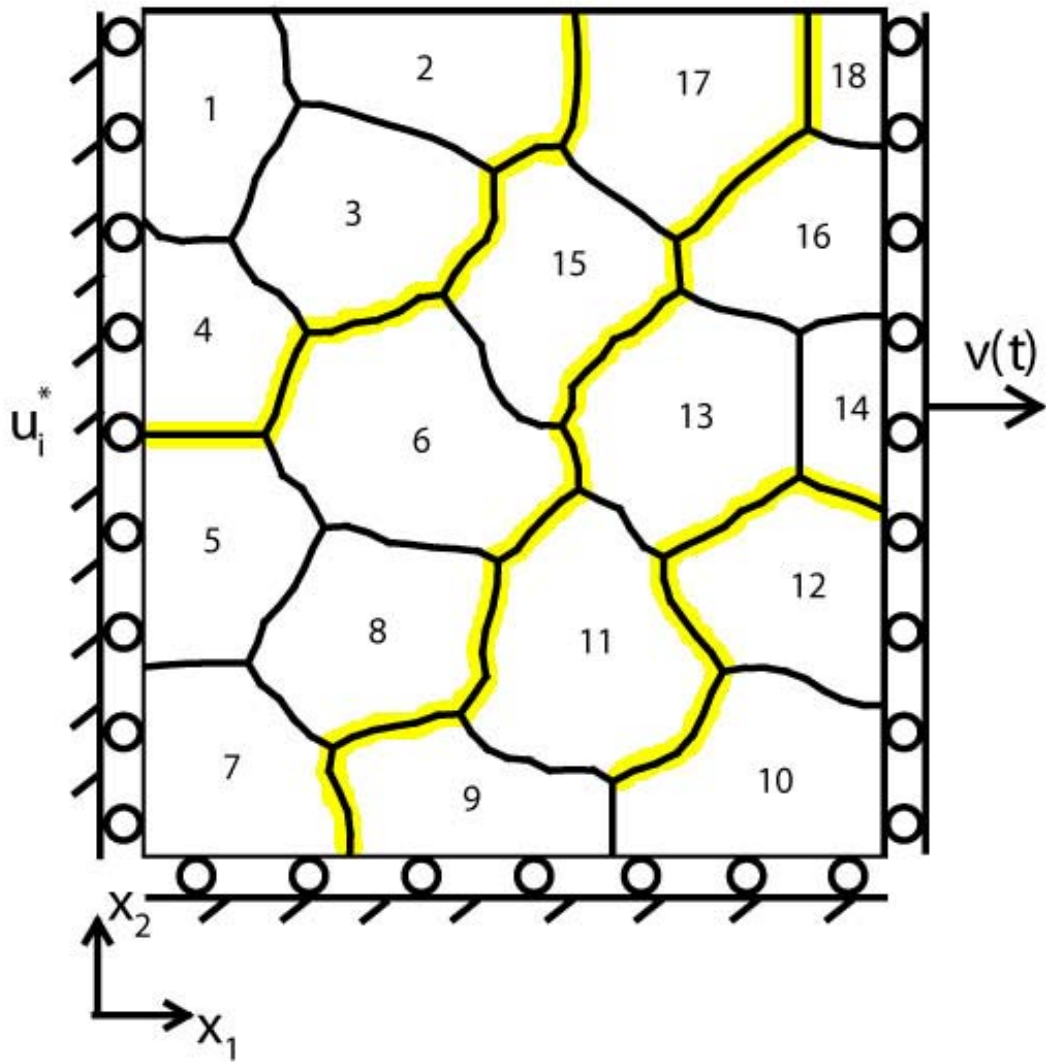


Figure 6.10: Distribution of the grain boundaries with allowed or restricted sliding aligned diagonally across the microstructure.

Table 6.1: Values for material parameters used in the finite element simulations for aluminum alloy 5083.

<b>Parameter</b>	<b>Value</b>
Grain size $L$	7 $\mu\text{m}$
Atomic volume $\Omega$	$1.66 \times 10^{-29} \text{ m}^3$
Young's modulus $E$	70 GN $\text{m}^{-2}$
Poisson's ratio $\nu$	0.3
Shear modulus $\mu$	26.9 GN $\text{m}^{-2}$
Characteristic strain rate $\dot{\gamma}_0$	5.20 $\text{s}^{-1}$
Initial yield stress $\tau_0$	65 MN $\text{m}^{-2}$
Solute drag creep stress exponent $n$	4.5
Grain boundary diffusion pre-exponential $\delta_{GB} D_{GBi}$	$1.02 \times 10^{-13} \text{ m}^3 \text{ s}^{-1}$
Grain boundary diffusion activation energy $Q_{GBi}$	$1.34 \times 10^{-19} \text{ J}$
Grain boundary sliding resistance coefficient $\eta$	$4.74 \times 10^{-8} \text{ m}^3 \text{ MN}^{-1} \text{ s}^{-1}$



## **CHAPTER 7: CONCLUSIONS AND FUTURE WORK**

This dissertation presents work to further understanding of deformation mechanisms in magnesium alloys at elevated temperature in an effort that will enable decreased forming temperature and decreased cycle time (by increasing the strain rate for forming) for constructing vehicle body panels from magnesium alloys. The work documents a combined experimental and computational approach that focuses on the behavior of the material at a microstructural level and its influence on the macroscopic properties necessary to improve formability. Although this work did not unearth a silver bullet to solve the problem of formability in magnesium alloys during sheet metal forming, it has achieved substantial headway in the quest to find an economically viable solution for using magnesium alloys to build lighter, more gas efficient automobiles.

### **7.1 Conclusions**

First the properties of 99.999 percent pure magnesium were considered from an experimental standpoint. Substantial grain growth was observed in pure magnesium as a function of temperature and strain rate. However, once the steady state grain size was

reached continued grain growth was not observed with increasing amounts of strain in the sample or time at elevated temperature. Ductility of the pure magnesium samples was independent of temperature and strain rate, but yield strength was a function of both variables. The strain rate sensitivity was found to be approximately 0.2 for deformation at strain rates from  $3.0 \times 10^{-2} s^{-1}$  to  $1.0 \times 10^{-4} s^{-1}$  and temperatures from 350°C to 450°C, suggesting that dislocation creep is dominant within this range.

In contrast to the pure magnesium material, in tests on magnesium alloy AZ31 ductility and yield strength were shown to be dependent on temperature and strain rate, and little grain growth was observed. Furthermore, the alloy material exhibited a dynamic response to strain rate over the same range. The strain rate sensitivity increased from 0.2 at high strain rates to between 0.3 and 0.5 at low strain rates, which suggests a change in the deformation mechanism from dislocation creep at high strain rates to grain boundary sliding. The extent that the strain rate sensitivity increased at low strain rates is a result of anisotropic effects in the extruded material.

The extrusion process imparted a strong texture in the sheet material that had a strong effect on the plastic response when loading was applied parallel or perpendicular to the extruded direction. If loading was performed parallel to the extruded direction, deformation exhibited the following characteristics: the strain rate sensitivity equaled 0.3 at low strain rates, necking occurred primarily in the thickness direction, and in comparison to the alternatively oriented sample, there was a greater yield stress and less ductility. If the tensile axis was oriented perpendicular to the extruded direction, the following characteristics were observed: the strain rate sensitivity equaled 0.5 at low strain rates, necking occurred primarily in the width direction, the yield stress was

smaller, and ductility increased. The microstructure of the material contains two possible origins for this anisotropic behavior: grain size and grain orientation. The extrusion process generates a strong basal texture in the extruded direction. Thus, for the sample oriented  $0^\circ$  to the extruded direction the grains are oriented with the basal plane along the tensile axis and the apparent grain size is approximately  $18\mu\text{m}$ , whereas for the sample oriented  $90^\circ$  to the ED the basal plane of the grains is oriented perpendicular to the tensile direction and the apparent grain size is  $9\mu\text{m}$ . Computational methods were used to attempt to discover the effect of the orientation of the samples and the microstructural differences associated with each orientation on the constitutive response during tensile deformation.

To understand the experimental observations a polycrystal continuum finite element model was developed that accounts for three deformation mechanisms within the microstructure; dislocation creep within the grains together with sliding and diffusion along the grain boundaries. The model was calibrated and then validated using experimental data of magnesium AZ31 that had been thermo-mechanically processed to various grain sizes. The model predicted the influence of grain size and strain rate on the flow stress with excellent agreement to the experimental data. Both variables were shown to have a significant impact on superplastic deformation in magnesium. The strain rate where the dominant deformation mechanism transitions from dislocation creep to grain boundary sliding, which is indicative of a transition from plastic to superplastic deformation, migrated to higher strain rates with an decrease in grain size.

The validated model was used to study the extruded magnesium AZ31 sheet material at  $350^\circ\text{C}$  and  $450^\circ\text{C}$ . The major microstructural differences that were observed

in the experimental procedure were accounted for by adjusting the simulation microstructure used as input to the model. The model predictions were in excellent agreement to the experimental results and allowed for the following insights. At QPF temperatures the transition point from dislocation creep to grain boundary sliding occurred at a strain rate of  $1.5 \times 10^{-4} s^{-1}$  when the tensile axis was oriented  $0^\circ$  to the extruded direction and increased to  $2.0 \times 10^{-3} s^{-1}$  when the tensile axis was rotated  $90^\circ$ . If the testing temperature was reduced to  $350^\circ\text{C}$ , the transition point decreased one order of magnitude independent of the orientation. When the tensile axis is oriented  $0^\circ$  to the extruded direction slip is most active on the prismatic plane followed by slip on the basal and pyramidal systems respectively. However, for the alternatively oriented sample, slip is most active on the basal system followed by slip on the pyramidal and prismatic system respectively. For the latter orientation, slip was more evenly distributed across each system.

By analyzing the results from the experimental work on extruded magnesium AZ31 sheet in combination with the computational study it was concluded that the increased ductility of the sample oriented with the tensile axis  $90^\circ$  to the extruded direction is due to increased grain boundary sliding during deformation at this orientation. The increase in grain boundary sliding is largely due to the decrease in the apparent grain size at this orientation. However, the effect of grain orientation is also influential. The orientation of the grains when the tensile axis is  $90^\circ$  to the ED allows alternate systems to activate in comparison to the sample oriented  $0^\circ$  to the ED and leads to more even distribution of slip across the various slip systems and thus a more even distribution of stress in the microstructure.

Although it was expected that grain size would have a significant impact on the deformation behavior of magnesium AZ31, orientation was also expected to have a substantial impact. There are substantial differences in the geometry and strength of the basal, prismatic, and pyramidal slip systems, which in addition to the texture of the extruded sheet led to preferential slip on the various systems. The orientation of the grains with respect to the tensile axis affected the flow stress and the distribution of the deformation mechanisms, but the effect on plastic flow was not as substantial as the change in grain size.

Aluminum alloys are used in similar lightweight applications to magnesium alloys. However, magnesium alloys allows for increased weight reduction compared to aluminum and thus processes such as QPF are being adapted for magnesium. Thus, it is instructive to consider the differences in the two materials. Although, it was determined that orientation with respect to the tensile axis did not have as large a role as expected in the plastic response of magnesium it was necessary to consider, whereas this was unnecessary for aluminum. The aluminum model accounted for plastic shearing on the twelve  $\{111\}\langle 110 \rangle$  slip systems, which have extensive symmetry and an equal critical resolved shear stress on each slip system. Besides the substantial difference between the atomic structure of aluminum and magnesium, the differences between the two metals manifested itself in other ways. The stress exponent for magnesium rose to higher values than aluminum at fast strain rates and fell to smaller values at slow strain rates. This suggests a greater change in the deformation mechanism over the range of strain rates tested. The transition from the grain boundary sliding regime to the dislocation creep regime was shown to occur at greater strain rates in magnesium compared to aluminum,

which shows promise for forming at greater strain rates for magnesium alloys. This difference is due to greater contributions from the grain boundary sliding mechanism, which is a result of the greater grain boundary fluidity and grain boundary diffusion parameters in magnesium. Unexpectedly a threshold stress for grain boundary sliding was not needed to model magnesium, whereas inclusion of a threshold stress allowed for a significant improvement in modeling the plastic response of aluminum. Overall, these changes show promise for increased use of magnesium alloys in the automobile industry due to the evidence for greater formability at elevated temperatures.

Due to the importance of grain boundary sliding in superplastic behavior, chapter 6 explained an investigation into the influence of heterogeneity in the resistance of grain boundaries to sliding on the constitutive behavior of aluminum alloy 5083 during elevated temperature deformation. This work utilized the finite element model described in chapter 3 adapted to aluminum. The study randomly assigned each grain boundary in the polycrystal one of two possible values of sliding resistance: a fraction  $f$  were allowed to slide freely, while the remaining fraction of boundaries ( $1-f$ ) were restricted from sliding freely. It was shown that deformation in the polycrystal was largely dependent on  $f$ , by documenting its effect on the transition point, the stress exponent at low strain rates, and the flow stress. These conclusions suggest that grain boundary engineering is possible to increase superplastic behavior in aluminum alloys. Although this work was completed for aluminum alloy 5083, it is assumed that qualitatively the same conclusions will apply to magnesium. The study assumes that some boundaries will slide freely and some will resist sliding based on the characteristics of the grain boundary. Although the grain boundary characteristics that enhance or restrict sliding in magnesium compared to

aluminum may differ, these two classes of boundaries will still exist.

## **7.2 Recommendations for Future Work**

During on the work performed to complete this dissertation, ideas have surfaced for future work that would build upon and enhance the work presented here. Some of these ideas are as follows.

The model predictions show excellent agreement with experiment, however, extension of the model could prove useful to further understanding of deformation of magnesium alloys at elevated temperature. As was noted only a small amount of strain is imposed on each system and thus the simulation microstructure is deformed only slightly. This was necessary for continuity of the grains being deformed in the finite element mesh. However, this only allows for limited grain refinement or rotation of the grains. Thus, texture evolution of the microstructure due to increasing strain is not accounted for. In light of the importance of texture in magnesium systems it would be beneficial to extend the model to handle large strains so that texture evolution can be understood. Presently the model is capable of computing the pole figures for the simulation microstructure, but in this work there is little change in the pole figures during the simulation because only a small amount of strain is imposed on the system. The pole figures could be used to monitor texture evolution over large strains induced in the polycrystal. Modeling texture evolution in magnesium would be especially interesting due to the unequal critical resolved shear stress on the various slip systems. As was shown by Yi et al. in their work with extruded magnesium AZ31 sheet, the texture of the

initial microstructure and the type of straining (in their case, uniaxial tension or compression) is shown to impact the texture evolution because grains rotate to accommodate strain based on their orientation with respect to the loading direction and the critical resolved shear stress on each slip system (Yi et al., 2006).

The importance of grain boundary sliding in deformation of magnesium naturally suggests that deeper investigation of this mechanism would be beneficial. As was shown in chapter 6 for aluminum adjusting the resistance of the grain boundaries to sliding can have a significant impact on the constitutive response of the material. However, this study assumed that the boundaries either slid freely or completely resisted sliding. An effective direction for future work would be to develop a more realistic model that accounts for the characteristics of the individual grain boundaries and does not limit boundary motion to sliding alone. Cahn and Taylor suggest that motion along the interface of adjacent grains is the result of coupled motion between grain boundary sliding and grain boundary migration based on the character of the boundary and the applied stress (Cahn & Taylor, 2004). In magnesium this has been observed experimentally in work on magnesium bicrystals by Kumar and Syed (Kumar & Syed, 2009), and in molecular dynamics simulations by Zhang (Zhang, 2009). Allowing for grain boundary migration to occur in the model coupled with grain boundary sliding, both of which are influenced by the grain boundary character would enable a more realistic analysis of grain boundary motion and its effect on deformation in magnesium. Furthermore, this could open up greater possibilities for grain boundary engineering that could lead to increased ductility of magnesium alloys.



## REFERENCES

- Agarwal, S., Briant, C. L., Krajewski, P. E., Bower, A. F., & Taleff, E. M. (2007). Experimental Validation of Two-dimensional Finite Element Method for Simulating Constitutive Response of Polycrystals During High Temperature Plastic Deformation. *Journal of Materials Engineering and Performance*, *16*(2), 170-178. doi:10.1007/s11665-007-9028-0
- Agarwal, S., Krajewski, P. E., & Briant, C. L. (2004). Texture development and dynamic recrystallization in AA5083 during superplastic forming at various strain rates. *Advances in Superplasticity and Superplastic Forming*, 95-107.
- Agnew, S. R., & Duygulu, Ö. (2005). Plastic anisotropy and the role of non-basal slip in magnesium alloy AZ31B. *International Journal of Plasticity*, *21*(6), 1161-1193. doi:10.1016/j.ijplas.2004.05.018
- Al-Samman, T., & Gottstein, G. (2008). Dynamic recrystallization during high temperature deformation of magnesium. *Materials Science and Engineering: A*, *490*(1-2), 411-420. doi:10.1016/j.msea.2008.02.004
- Ashby, M. F., Edward, G. H., Davenport, J., & Verrall, R. A. (1978). Application of Bound Theorems for Creeping Solids and Their Application to Large Strain Diffusional Flow. *Acta Metallurgica*, *26*(9), 1379-1388.
- Ashby, M. F., & Verrall, R. A. (1973). Diffusion-Accommodated Flow and Superplasticity. *Acta Metallurgica*, *21*(2), 149-163. doi:10.1016/0001-6160(73)90057-6
- Ball, A., & Hutchinson, M. M. (1969). Superplasticity in the aluminium-zinc eutectoid.

*Met. Sci. J*, 3, 1-6.

Bandivadekar, A., Bodek, K., Cheah, L., Evans, C., Groode, T., Heywood, J., Kasseris, E., et al. (2008). *On the road in 2035: reducing transportation's petroleum consumption and GHG emissions* (1st ed.). Cambridge Mass.: Massachusetts Institute of Technology.

Barnes, A. J. (1994). Superplastic forming of aluminum alloys. *Materials Science Forum*, 170-172, 701-714.

Barnes, A. J. (2007). Superplastic Forming 40 Years and Still Growing. *Journal of Materials Engineering and Performance*, 16(4), 440-454. doi:10.1007/s11665-007-9076-5

Barnett, M. R. (2003). A Taylor model based description of the proof stress of magnesium AZ31 during hot working. *Metallurgical and Materials Transactions A*, 34(9), 1799-1806. doi:10.1007/s11661-003-0146-5

Barnett, M. R., Ghaderi, A., Sabirov, I., & Hutchinson, B. (2009). Role of grain boundary sliding in the anisotropy of magnesium alloys. *Scripta Materialia*, 61(3), 277-280. doi:10.1016/j.scriptamat.2009.04.001

Beausir, B., Toth, L., & Neale, K. (2007). Role of strain-rate sensitivity in the crystal plasticity of hexagonal structures. *International Journal of Plasticity*, 23(2), 227-243. doi:10.1016/j.ijplas.2006.02.013

Bower, A. F., & Wininger, E. (2004). A two-dimensional finite element method for simulating the constitutive response and microstructure of polycrystals during high temperature plastic deformation. *Journal of the Mechanics and Physics of Solids*, 52(6), 1289-1317. doi:10.1016/j.jmps.2003.11.004

- Bradley, J. R. (2004). Bulge testing of superplastic AA5083 aluminum sheet. *Advances in Superplasticity and Superplastic Forming*, 109-118.
- Buchovecky, E. J., Du, N., & Bower, A. F. (2009). A model of Sn whisker growth by coupled plastic flow and grain boundary diffusion. *Applied Physics Letters*, 94(19), 191904. doi:10.1063/1.3136865
- Buckingham, D. A. (2006). *Aluminum Stocks in Use in Automobiles in the United States* (Fact Sheet No. 2005-3145). U.S. Geological Survey.
- Carter, J. T., Krajewski, P. E., & Verma, R. (2008). The hot blow forming of AZ31 Mg sheet: Formability assessment and application development. *JOM*, 60(11), 77-81. doi:10.1007/s11837-008-0153-5
- Chandra, N. (2002). Constitutive behavior of superplastic materials. *International Journal of Non-Linear Mechanics*, 37(3), 461-484. doi:10.1016/S0020-7462(01)00021-X
- Chen, Y., & Schuh, C. (2006). Diffusion on grain boundary networks: Percolation theory and effective medium approximations. *Acta Materialia*, 54(18), 4709-4720. doi:10.1016/j.actamat.2006.06.011
- Chen, Y., & Schuh, C. (2007). Coble creep in heterogeneous materials: The role of grain boundary engineering. *Physical Review B*, 76(6). doi:10.1103/PhysRevB.76.064111
- Cipoletti, D. E., Bower, A. F., & Krajewski, P. E. (2011). A microstructure-based model of the deformation mechanisms and flow stress during elevated-temperature straining of a magnesium alloy. *Scripta Materialia*, 64(10), 931-934. doi:10.1016/j.scriptamat.2010.12.033

- Cipoletti, D. E., Bower, A. F., Qi, Y., & Krajewski, P. E. (2009). The influence of heterogeneity in grain boundary sliding resistance on the constitutive behavior of AA5083 during high-temperature deformation. *Materials Science and Engineering: A*, 504(1-2), 175-182. doi:10.1016/j.msea.2008.10.037
- Coble, R. L. (1963). A Model for Boundary Diffusion Controlled Creep in Polycrystalline Materials. *Journal of Applied Physics*, 34(6), 1679-1682.
- Du, N. (2009, May). *Multiscale Modeling of Deformation and Failure Mechanisms of Al Alloys at Elevated Temperature*. Providence, RI: Brown University.
- Du, N., Bower, A. F., & Krajewski, P. E. (2010). Numerical simulations of void growth in aluminum alloy AA5083 during elevated temperature deformation. *Materials Science and Engineering: A*, 527(18-19), 4837-4846. doi:10.1016/j.msea.2010.04.010
- Du, N., Bower, A. F., Krajewski, P. E., & Taleff, E. M. (2008). The influence of a threshold stress for grain boundary sliding on constitutive response of polycrystalline Al during high temperature deformation. *Materials Science and Engineering: A*, 494(1-2), 86-91. doi:10.1016/j.msea.2007.10.089
- Ecob, N., & Ralph, B. (1983). The effect of grain size on deformation twinning in a textured zinc alloy. *Journal of Materials Science*, 18(8), 2419-2429. doi:10.1007/BF00541848
- Freund, L., & Suresh, S. (2003). *Thin film materials: stress, defect formation, and surface evolution*. Cambridge [England];New York: Cambridge University Press.
- Frost, H., & Ashby, M. F. (1982). *Deformation-mechanism maps: the plasticity and creep of metals and ceramics* (1st ed.). Oxford [Oxfordshire];New York: Pergamon

Press.

- Fukutomi, H., Yamamoto, T., Nonomura, K., & Takada, K. (1999). Examination of dislocation mechanism on grain boundary sliding in high angle grain boundaries by stress change test. *Interface Science*, 7(2), 141-146.
- Gehrmann, R., Frommert, M., & Gottstein, G. (2005). Texture effects on plastic deformation of magnesium. *Materials Science and Engineering A*, 395(1-2), 338-349. doi:10.1016/j.msea.2005.01.002
- Ghosh, A. K. (1994). New physical model for superplastic flow. *Materials Science Forum*, 170-172, 39-46.
- Gifkins, R. C. (1976). Grain-boundary sliding and its accommodation during creep and superplasticity. *Metallurgical Transactions A (Physical Metallurgy and Materials Science)*, 7(8), 1225-1232.
- Gittus, J. H. (1977). Theory of superplastic flow in two-phase materials: Roles of interphase-boundary dislocation, ledges, and diffusion. *Journal of Engineering Materials and Technology, Transactions of the ASME*, 99(3), 244-251.
- Hayden, H. W., Floreen, S., & Goodell, P. D. (1972). Deformation mechanisms of superplasticity. *Metallurgical and Materials Transactions*, 3(4), 833-842.
- Hutchinson, B., & Barnett, M. R. (2010). Effective values of critical resolved shear stress for slip in polycrystalline magnesium and other hcp metals. *Scripta Materialia*, 63(7), 737-740. doi:10.1016/j.scriptamat.2010.05.047
- Hutchinson, B., Barnett, M. R., Ghaderi, A., Cizek, P., & Sabirov, I. (2009). Deformation modes and anisotropy in magnesium alloy AZ31. *International Journal of Materials Research (formerly Zeitschrift fuer Metallkunde)*, 100(04), 556-563.

doi:10.3139/146.110070

Kaibyshev, O. A., Valiev, R. Z., & Emaletdinov, A. K. (1985). Deformation mechanisms and the theory of structural superplasticity of metals. *Physica Status Solidi (A) Applied Research*, 90(1), 197-206.

Kaifeng, Z., Deliang, Y., Guofeng, W., & Wenbo, H. (2006). Superplastic deformation behavior of hot-rolled AZ31 magnesium alloy sheet at elevated temperatures. *Journal of Wuhan University of Technology-Mater. Sci. Ed.*, 21(3), 1-6.

doi:10.1007/BF02840866

Kelley, E. W., & Hosford, W. F. (1968). *Transactions of the Metallurgical Society of AIME*, 242, 654-660.

Kim, W., Chung, S. W., Chung, C. S., & Kum, D. (2001). Superplasticity in thin magnesium alloy sheets and deformation mechanism maps for magnesium alloys at elevated temperatures. *Acta Materialia*, 49(16), 3337-3345.

doi:10.1016/S1359-6454(01)00008-8

Kokawa, H., Watanabe, T., & Karashima, S. (1981). Sliding behaviour and dislocation structures in aluminium grain boundaries. *Philosophical Magazine A*, 44(6), 1239-1254. doi:10.1080/01418618108235806

Krajewski, P. E. (2004). Research opportunities for automotive superplastic forming alloys. *Advances in Superplasticity and Superplastic Forming*, 173-184.

Krajewski, P. E., Ben-Artzy, A., & Mishra, R. K. (2010). Room temperature tensile anisotropy of extruded magnesium plates. *Magnesium Technology*, 467-472.

Krajewski, P. E., Hector Jr., L. G., Du, N., & Bower, A. F. (2010). Microstructure-based multiscale modeling of elevated temperature deformation in aluminum alloys.

*Acta Materialia*, 58(3), 1074-1086. doi:10.1016/j.actamat.2009.10.023

Krajewski, P. E., & Morales, A. T. (2004). Tribological Issues During Quick Plastic Forming. *Journal of Materials Engineering and Performance*, 13(6), 700-709.

doi:10.1361/10599490421330

Krajewski, P. E., & Schroth, J. G. (2007). Overview of Quick Plastic Forming Technology. *Materials Science Forum*, 551-552, 3-12.

Kulas, M. A., Green, W. P., Pettengill, E. C., Krajewski, P. E., & Taleff, E. M. (2004). Superplastic failure mechanisms and ductility of AA5083, 127-138.

Kulas, M. A., Green, W. P., Taleff, E. M., Krajewski, P. E., & McNelley, T. R. (2005). Deformation mechanisms in superplastic AA5083 materials. *Metallurgical and Materials Transactions A: Physical Metallurgy and Materials Science*, 36(5), 1249-1261.

Kulas, M. A., Green, W. P., Taleff, E. M., Krajewski, P. E., & McNelley, T. R. (2006). Failure mechanisms in superplastic AA5083 materials. *Metallurgical and Materials Transactions A: Physical Metallurgy and Materials Science*, 37(3), 645-655.

Langdon, T. G. (1970). Grain boundary sliding as a deformation mechanism during creep. *Philosophical Magazine*, 22(178), 689-700.

Langdon, T. G. (2006). Grain boundary sliding revisited: Developments in sliding over four decades. *Journal of Materials Science*, 41(3), 597-609. doi:10.1007/s10853-006-6476-0

Lapovok, R., Estrin, Y., Popov, M. V., Rundell, S., & Williams, T. (2008). Enhanced superplasticity of magnesium alloy AZ31 obtained through equal-channel angular

- pressing with back-pressure. *Journal of Materials Science*, 43(23-24), 7372-7378.  
doi:10.1007/s10853-008-2685-z
- Lebensohn, R., & Tome, C. (1993). A self-consistent anisotropic approach for the simulation of plastic deformation and texture development of polycrystals: Application to zirconium alloys. *Acta Metallurgica et Materialia*, 41(9), 2611-2624. doi:10.1016/0956-7151(93)90130-K
- Lee, H. P., Esling, C., & Bunge, H. J. (1988). Development of the Rolling Texture in Titanium. *Textures and Microstructures*, 7(4), 317-337. doi:10.1155/TSM.7.317
- Lifshitz, I. M. (1963). *Soviet Phys. JETP*, 17, 909-920.
- McNalley, T. R., Oh-Ishi, K., Zhilyaev, A. P., Swaminathan, S., Krajewski, P. E., & Taleff, E. M. (2007). Characteristics of the Transition from Grain-Boundary Sliding to Solute Drag Creep in Superplastic AA5083. *Metallurgical and Materials Transactions A*, 39(1), 50-64. doi:10.1007/s11661-007-9401-5
- Mukherjee, A. K. (1971). The rate controlling mechanism in superplasticity. *Materials Science and Engineering*, 8(2), 83-89.
- Nieh, T. (1997). *Superplasticity in metals and ceramics*. Cambridge [England];New York NY USA: Cambridge University Press.
- Obara, T., Yoshinga, H., & Morozumi, S. (1973).  $\{11\bar{2}2\}\langle\bar{1}\bar{1}23\rangle$  Slip system in magnesium. *Acta Metallurgica*, 21(7), 845-853. doi:10.1016/0001-6160(73)90141-7
- Pan, J., & Cocks, A. (1993). Computer simulation of superplastic deformation. *Computational Materials Science*, 1(2), 95-109. doi:10.1016/0927-0256(93)90001-4



- Panicker, R., Chokshi, A. H., Mishra, R. K., Verma, R., & Krajewski, P. E. (2009). Microstructural evolution and grain boundary sliding in a superplastic magnesium AZ31 alloy. *Acta Materialia*, 57(13), 3683-3693.  
doi:10.1016/j.actamat.2009.04.011
- Peirce, D., Asaro, R., & Needleman, A. (1983). Material rate dependence and localized deformation in crystalline solids. *Acta Metallurgica*, 31(12), 1951-1976.  
doi:10.1016/0001-6160(83)90014-7
- Peraire, J., Vahdati, M., Morgan, K., & Zienkiewicz, O. (1987). Adaptive remeshing for compressible flow computations. *Journal of Computational Physics*, 72(2), 449-466. doi:10.1016/0021-9991(87)90093-3
- Philippe, M. (1994). Texture formation in hexagonal materials. *Materials Science Forum*, 157-162, 1337-1350.
- Philippe, M., Beaujean, I., Bouzy, E., Diot, M., Wegria, J., & Esling, Claude. (1994). Effect of Texture and Microstructure on the Mechanical Properties of Zn Alloys. *Materials Science Forum*, 157-162, 1671-1674.  
doi:10.4028/www.scientific.net/MSF.157-162.1671
- Philippe, M., Bouzy, E., & Fundenberger, J.-J. (1998). Textures and Anisotropy of Titanium Alloys. *Materials Science Forum*, 273-275, 511-522.  
doi:10.4028/www.scientific.net/MSF.273-275.511
- Philippe, M., Esling, C., & Hocheid, B. (1988). Role of Twinning in Texture Development and in Plastic Deformation of Hexagonal Materials. *Textures and Microstructures*, 7(4), 265-301. doi:10.1155/TSM.7.265
- Philippe, M., Serghat, M., Vanhoutte, P., & Esling, C. (1995). Modelling of texture

evolution for materials of hexagonal symmetry—II. application to zirconium and titanium  $\alpha$  or near  $\alpha$  alloys. *Acta Metallurgica et Materialia*, 43(4), 1619-1630.

doi:10.1016/0956-7151(94)00329-G

Philippe, M., Wagner, F., Mellab, F., Esling, C., & Wegria, J. (1994). Modelling of texture evolution for materials of hexagonal symmetry—I. Application to zinc alloys.

*Acta Metallurgica et Materialia*, 42(1), 239-250. doi:10.1016/0956-

7151(94)90066-3

Prakash, A., Weygand, S. M., & Riedel, H. (2009). Modeling the evolution of texture and grain shape in Mg alloy AZ31 using the crystal plasticity finite element method.

*Computational Materials Science*, 45(3), 744-750.

doi:10.1016/j.commatsci.2008.06.015

Qi, Y., & Krajewski, P. E. (2007). Molecular dynamics simulations of grain boundary sliding: The effect of stress and boundary misorientation. *Acta Materialia*, 55(5),

1555-1563. doi:10.1016/j.actamat.2006.10.016

Rachinger, W. A. (1952). Relative Grain Translations in the Plastic Flow of Aluminum.

*Journal of the Institute of Metals*, 81, 33-41.

Raeisina, B., & Agnew, S. R. (2010). Using polycrystal plasticity modeling to determine

the effects of grain size and solid solution additions on individual deformation mechanisms in cast Mg alloys. *Scripta Materialia*, 63(7), 731-736.

doi:10.1016/j.scriptamat.2010.03.054

Raj, R., & Ashby, M. F. (1971). On Grain Boundary Sliding and Diffusional Creep. *Met*

*Trans*, 2(4), 1113-1127.

Reed-Hill, R. E., & Robertson, W. D. (1957a). Deformation of magnesium single crystals

- by nonbasal slip. *Transactions of the Metallurgical Society of AIME*, 220, 496-502.
- Reed-Hill, R. E., & Robertson, W. D. (1957b). The crystallographic characteristics of fracture in magnesium single crystals. *Acta Metallurgica*, 5(12), 728-737.  
doi:10.1016/0001-6160(57)90075-5
- Reed-Hill, R. E., & Robertson, W. D. (1958). Pyramidal slip in magnesium. *Transactions of the Metallurgical Society of AIME*, 221, 256-259.
- Schroth, J. G. (2004). General Motors' Quick Plastic Forming Process. *Advances in Superplasticity and Superplastic Forming*, 9-20.
- Sheng, Z., & Shivpuri, R. (2006). Modeling flow stress of magnesium alloys at elevated temperature. *Materials Science and Engineering: A*, 419(1-2), 202-208.  
doi:10.1016/j.msea.2005.12.020
- Somekawa, H., Hirai, K., Watanabe, H., Takigawa, Y., & Higashi, K. (2005). Dislocation creep behavior in Mg–Al–Zn alloys. *Materials Science and Engineering: A*, 407(1-2), 53-61. doi:10.1016/j.msea.2005.06.059
- Staroselsky, A., & Anand, L. (2003). A constitutive model for hcp materials deforming by slip and twinning application to magnesium alloy AZ31B. *International Journal of Plasticity*, 19(10), 1843-1864. doi:10.1016/S0749-6419(03)00039-1
- Takuda, H., Morishita, T., Kinoshita, T., & Shirakawa, N. (2005). Modelling of formula for flow stress of a magnesium alloy AZ31 sheet at elevated temperatures. *Journal of Materials Processing Technology*, 164-165, 1258-1262.  
doi:10.1016/j.jmatprotec.2005.02.034
- Taub, A. I., Krajewski, P. E., Luo, A. A., & Owens, J. N. (2007). The evolution of

- technology for materials processing over the last 50 years: The automotive example. *JOM*, 59(2), 48-57. doi:10.1007/s11837-007-0022-7
- U.S Environmental Protection Agency. (2011, February 9). Regulations & Standards. Transportation and Climate. Retrieved May 3, 2011, from <http://www.epa.gov/otaq/climate/regulations.htm#finalR>
- U.S. Energy and Information Administration. (2009). *Annual Energy Review 2009*. Washington, DC: U.S. Department of Energy. Retrieved from <http://www.eia.doe.gov/totalenergy/data/annual/>
- Vagarali, S. S., & Langdon, T. G. (1981). Deformation mechanisms in h.c.p. metals at elevated temperatures—I. Creep behavior of magnesium. *Acta Metallurgica*, 29(12), 1969-1982. doi:10.1016/0001-6160(81)90034-1
- del Valle, J. A., Carreno, F., & Ruano, O. A. (2007). On the threshold stress for superplasticity in Mg–Al–Zn alloys. *Scripta Materialia*, 57(9), 829-832. doi:10.1016/j.scriptamat.2007.07.002
- del Valle, J. A., Pérez-Prado, M. T., & Ruano, O. A. (2005). Deformation mechanisms responsible for the high ductility in a Mg AZ31 alloy analyzed by electron backscattered diffraction. *Metallurgical and Materials Transactions A*, 36(6), 1427-1438. doi:10.1007/s11661-005-0235-8
- del Valle, J. A., & Ruano, O. A. (2006). Influence of the grain size on the strain rate sensitivity in an Mg–Al–Zn alloy at moderate temperatures. *Scripta Materialia*, 55(9), 775-778. doi:10.1016/j.scriptamat.2006.07.013
- Verma, R. (2010, August). personal communication, General Motors Company.
- Verma, R., Carter, J. T., & Krajewski, P. E. (2009). High-temperature deformation

- behavior of three rolled sheets of magnesium alloy AZ31. *Magnesium Technology*, 399-403.
- Verma, R., Hector, L. G., Krajewski, P. E., & Taleff, E. M. (2009). The finite element simulation of high-temperature magnesium AZ31 sheet forming. *JOM*, 61(8), 29-37. doi:10.1007/s11837-009-0118-3
- Vespa, G., Mackenzie, L., Verma, R., Zarandi, F., Essadiqi, E., & Yue, S. (2008). The influence of the as-hot rolled microstructure on the elevated temperature mechanical properties of magnesium AZ31 sheet. *Materials Science and Engineering: A*, 487(1-2), 243-250. doi:10.1016/j.msea.2007.10.064
- Wang, H., & Yang, Wei. (2004). Constitutive modeling for nanocrystalline metals based on cooperative grain boundary mechanisms. *Journal of the Mechanics and Physics of Solids*, 52(5), 1151-1173. doi:10.1016/j.jmps.2003.08.005
- Ward Flynn, P. W., Mote, J., & Dorn, J. E. (1961). *Transactions of the Metallurgical Society of AIME*, 221, 1148-1154.
- Weinberg, F. (1958). *Transactions of the Metallurgical Society of AIME*, 212, 808-817.
- Wu, X., & Liu, Y. (2002). Superplasticity of coarse-grained magnesium alloy. *Scripta Materialia*, 46(4), 269-274. doi:10.1016/S1359-6462(01)01234-9
- Xiong, F., & Davies, C. H. J. (2003). Anisotropy of tensile properties of extruded magnesium alloy AZ31. *Materials Science Forum*, 426-432(4), 3605-3610.
- Yang, W., & Wang, Hongtao. (2004). Mechanics modeling for deformation of nano-grained metals. *Journal of the Mechanics and Physics of Solids*, 52(4), 875-889. doi:10.1016/j.jmps.2003.07.003
- Yi, S., Davies, C., Brokmeier, H., Bolmaro, R., Kainer, K., & Homeyer, J. (2006).

- Deformation and texture evolution in AZ31 magnesium alloy during uniaxial loading. *Acta Materialia*, 54(2), 549-562. doi:10.1016/j.actamat.2005.09.024
- Yi, S., Zaefferer, S., & Brokmeier, H. (2006). Mechanical behaviour and microstructural evolution of magnesium alloy AZ31 in tension at different temperatures. *Materials Science and Engineering: A*, 424(1-2), 275-281. doi:10.1016/j.msea.2006.03.022
- Yoo, M., Agnew, S., Morris, J., & Ho, K. (2001). Non-basal slip systems in HCP metals and alloys: source mechanisms. *Materials Science and Engineering A*, 319-321, 87-92. doi:10.1016/S0921-5093(01)01027-9
- Yoshinaga, H., & Horiuchi, R. (1963). Deformation Mechanisms in Magnesium Single Crystals Compressed in the Direction Parallel to Hexagonal Axis. *Japan Institute of Metals*, 4(1), 1-8.
- Zhang, K., Yin, D., Wang, G., & Han, W. (2006). Superplastic deformation behavior of hot-rolled AZ31 magnesium alloy sheet at elevated temperatures. *Journal Wuhan University of Technology, Materials Science Edition*, 21(3), 1-6.